UNIVERSITÀ DEGLI STUDI DI PADOVA

SCUOLA DI SCIENZE
Dipartimento di Geoscienze
Direttore Prof. Nicola Surian

TESI DI LAUREA MAGISTRALE IN GEOLOGIA
AMBIENTALE E DINAMICA DELLA TERRA

Estimate of seismic surface energy from microstructural studies of pseudotachylyte-bearing faults

Relatore: Prof. Giulio Di Toro
Correlatore: Prof. Giorgio Pennacchioni

Laureanda: Silvia Aldrighetti
Matricola: 2044594

ANNO ACCADEMICO 2022-2023

A mio nonno

Contents

Abstract

Earthquakes are the result of the propagation of a rupture and associated slip along a fault (Reid, 1910; Scholz, 2019). The total energy involved in a seismic event is quantitatively unknown but, neglecting the work against gravity, is qualitatively partitioned into radiated energy (E_R, seismic waves, that can be measured) and dissipated energy in the fault zone (E_{FZ}, mostly fracture and frictional heat, transparent to seismological investigations) (Cocco et al., 2023). The fracture energy G, or energy dissipated in rupture propagation, is one of the main energy sinks of an earthquake (Scholz, 2019). G can be estimated with some confidence through the inversion of seismic waves (i.e., seismological fracture energy G'), though its physical meaning remains unclear (Cocco et al., 2023). Instead, geological estimates of the energy associated with the formation of new fracture area (or fracture surface energy U_S) and frictional heat Q during seismic faulting might be possible. In fact, in the case of natural and experimental pseudotachylytes (solidified friction melts produced during seismic slip) and associated damage in their wall rocks, U_S is proportional to the surface of the fragments/microfractures while Q to the volume of melt produced (Pittarello et al., 2008; Johnson et al., 2021).

High resolution FESEM and image analysis were carried out to measure the microfracture pattern in the wall rocks of an E-W striking pseudotachylyte-bearing fault cutting tonalites in the continental crust (Gole Larghe Fault Zone, Adamello batholith, Italy). FESEM-Cathodoluminescence investigations evidence a pervasive damage in both wall rocks, with asymmetric distribution of both fracture density and crack orientation. The southern wall rocks are affected by a microfracture pattern with high density and preferential sub-vertical strike; the northern wall rocks have lower microfracture density and preferential sub-horizontal strike. Instead, in pseudotachylytes produced with rotary machines, where the effects of the propagation of the seismic rupture are negligible, the asymmetric distribution of the fracture density is absent and only a subtle difference in the microfracture strike is detected. These features, together with the results of numerical models simulating the propagation of seismic ruptures along the natural faults, support the hypothesis that the asymmetric damage measured in the natural wall rocks is coseismic.

Rock fragmentation is intense in the proximity (< 1 mm) of the natural pseudotachylyte fault and injection veins, but decays rapidly moving away from the fault. Because of this, the contribution of the microfracture damage in the wall rocks to U_S is

negligible with respect to the one of the densely fractured/fragmented micro-domains at the contact with the pseudotachylyte. For this reason, the micro-domains were considered as representative of the most intense damage associated with the propagation of seismic ruptures, and thus investigated through FESEM-CL, FESEM-EBSD and mid-angle FESEM-BSE techniques. This microstructural approach, with resolution of ∼ 90 nm, allowed to retrieve the Clast Size Distribution of the fragments in the micro-domains and to estimate U_S (Pittarello et al., 2008). However, the analysis yielded different U_S values depending on (1) the resolution limits of the techniques and thus the grainsize interval analysed and, (2) the CSDs, that in some cases could be described by more than one power-law distribution. Resulting estimates of U_S are: 0.015–0.023 MJ m^{-2} for FESEM-CL, 0.008 – 0.062 MJ m^{-2} for FESEM-EBSD and 0.43 – 1.35 MJ m^{-2} for mid-angle FESEM-BSE. The values of U_S, obtained with these new techniques, are consistent with previous estimates (Johnson et al., 2021; Pittarello et al., 2008). Still, even considering the highest U_S values, these are negligible with respect to the energy dissipated as frictional heat on the selected fault during the same seismic event (32 MJ m^{-2}).

In conclusion, frictional heat (32 MJ m^{-2}) is the biggest energy sink during rupture propagation in this selected fault segment cutting continental crustal rocks. Moreover, the seismological fracture energy G' estimated from numerical models of seismic ruptures propagating in faults in the same area ranges between 8 and 67 MJ m^{-2}. Consequently, U_S (1.35 MJ m^{-2}) or the energy directly associated with coseismic rock fragmentation, is likely a minimal contribution to G' and most of the so called the seismological fracture energy is probably heat.

Riassunto

I terremoti sono il risultato dalla propagazione di una rottura e dello scivolamento associato lungo una superficie di faglia (Reid, 1910; Scholz, 2019). L'energia totale coinvolta in un evento sismico è sconosciuta, ma, trascurando il lavoro contro la gravità, può essere divisa qualitativamente in energia irradiata (E_R, cioè le onde sismiche, che possono essere misurate) ed energia dissipata nella zona di faglia (E_{FZ}, per la maggior parte frattura e calore, non rilevabili da indagini sismiche) (Cocco et al., 2023). L'energia di frattura G, o l'energia spesa nella propagazione della rottura, è uno dei maggiori processi di dissipazione di energia durante un terremoto (Scholz, 2019). G può essere stimata con sufficiente sicurezza grazie all'inversione delle onde sismiche (energia sismica di frattura, G'), anche se il suo significato fisico rimane ambiguo (Cocco et al., 2023). Invece, stime geologiche dell'energia associata alla formazione di nuova area di superficie (o energia di superficie di frattura U_S) e del calore Q durante un evento sismico possono essere effettuate. Infatti, nel caso di pseudotachiliti naturali e sperimentali (fusi frizionali prodotti durante un terremoto) e l'associato danneggiamento nella roccia incassante, U_S è proporzionale alla superficie dei frammenti/microfratture, mentre Q al volume di fuso prodotto (Pittarello et al., 2008; Johnson et al., 2021).

Indagini ad alta risoluzione con tecniche FESEM e analisi d'immagine sono state svolte per misurare le microfratture nella roccia attorno a una faglia a pseudotachiliti che attraversa in direzione E-W delle tonaliti nella crosta continentale (Zona di Faglia delle Gole Larghe, batolite dell'Adamello, Italia). Analisi FESEM-CL evidenziano un danneggiamento pervasivo in entrambi i lati della faglia, ma con una distribuzione asimmetrica sia della densità che dell'orientazione delle microfratture. Il lato sud è interessato da microfratture con densità molto elevata, e un'orientazione preferenziale perpendicolare alla vena principale di pseudotachilite; il lato nord mostra invece una minore densità di frattura, e un'orientazione preferenziale sub-parallela alla pseudotachilite. Invece, nella pseudotachilite prodotta con il macchinario rotary, dove gli effetti della propagazione della rottura sismica sono trascurabili, la distribuzione asimmetrica della densità di frattura è assente, e la direzione delle microfratture presenta solo una sottile differenza. Queste caratteristiche, insieme ai risultati di modelli numerici di terremoti successi lungo faglie naturali, supportano l'ipotesi che il danneggiamento asimmetrico misurato nella roccia incassante naturale sia cosismico.

La comminuzione della roccia è estremamente elevata in prossimità della vena di faglia (< 1 mm) e delle estremità delle vene di iniezione, ma diminuisce rapidamente spostandosi verso la roccia incassante. Per questo, il contributo delle microfratture nella roccia incassante a U_S è limitato rispetto a quello dei micro-domini densamente frammentati al contatto tra la pseudotachilite e la tonalite. Perciò, i micro-domini sono stati considerati come rappresentativi del danneggiamento maggiore associato alla propagazione della rottura sismica, e quindi analizzati con tecniche FESEM-CL, FESEM-EBSD e mid-angle FESEM-BSE. Questo approccio microstrutturale, con una risoluzione di ~ 90 nm, ha permesso di ricavare le curve granulometriche (Clast Size Distribution curves) dei frammenti nei micro-domini e di stimare U_S (Pittarello et al., 2008). Tuttavia, l'analisi ha restituito diversi valori di U_S, a causa di (1) diversi limiti di risoluzione delle tecniche utilizzate e quindi del differente intervallo di dimensione dei frammenti analizzato, (2) le CSD, che in alcuni casi seguono una o più leggi di potenza. Gli intervalli di U_S risultanti sono: 0.015 – 0.023 MJ m^{-2} dai dati FESEM-CL, 0.008 – 0.062 MJ m^{-2} dai dati FESEM-EBSD, 0.43 – 1.35 MJ m^{-2} dai dati FESEM-BSE. I valori di U_S, ottenuti con queste nuove tecniche, concordano con stime precedenti presenti in letteratura (Johnson et al., 2021; Pittarello et al., 2008). Comunque, anche considerando l'intervallo più elevato di U_S, questo è trascurabile rispetto all'energia dissipata in calore dalla faglia selezionata durante lo stesso evento sismico (32 MJ m^{-2}).

In conclusione, il calore frizionale (32 MJ m^{-2}) è il maggiore dissipatore di energia durante la propagazione della rottura lungo la faglia selezionata, che attraversa la crosta continentale. Oltretutto, l'energia sismica di frattura G' calcolata da modelli numerici di rotture sismiche lungo faglie nella stessa area ha valori tra 8 e 67 MJ m^{-2}. Di conseguenza, U_S (1.35 MJ m^{-2}) o l'energia direttamente associata con la frammentazione cosismica della roccia, è probabilmente una minima parte di G' e la maggior parte dell'energia sismica di frattura è costituita da calore.

1. Introduction

1.1 Motivations

The total energy balance of an earthquake is still an unknown in seismology. The partitioning of the energy in seismic waves and associated dissipation processes, together with the determination of seismic source parameters (i.e., rupture directivity and speed, focal mechanism, dynamic coseismic fault strength, hypocentral depth, moment magnitude, etc.) is fundamental to better understand the mechanics of earthquakes (Scholz, 2019). Many of these parameters can be studied through seismological observations, but others (e.g., dynamic coseismic fault strength) are instead transparent to indirect investigations. The determination of the energy partitioning during rupture propagation is of high importance for the understanding of earthquake mechanics, because the latter is influenced by the processes happening during rupture propagation, both on the fault plane and in the damage zone (Pittarello et al., 2008). For instance, seismic fracture energy G' can be retrieved by the inversion of seismic waves and is one of the main measurable energy sinks during an earthquake (Ida, 1972; Abercrombie & Rice, 2005; Tinti et al., 2005). However, though G' is assumed to be the energy dissipated during rupture propagation (Ida, 1972), its physical meaning remains obscure.

Pseudotachylytes and the associated damage in the wall rocks have proven to be great proxies for the estimate of different seismic source parameters (Di Toro et al., 2005b; Pittarello et al., 2008; Lazari et al., 2023), among which fracture surface energy U_S. U_S is calculated from the total surface area of the grain fragments formed during a seismic event, with the latter attested by the presence of pseudotachylytes (Pittarello et al., 2008). The quality of the results obtained with this method is related to the quality of the fault outcrops and the possibility to determine other useful parameters from them (i.e. fault offset, pseudotachylyte thickness, total length of the fault etc.), but also to the quality of the analytical methods employed to investigate the damage associated to the pseudotachylytes (FESEM techniques). However, though both related somehow to the propagation of seismic ruptures, the relation between U_S and G' remains rather unclear.

The objective of the present thesis is thus to quantitatively analyse the damage surrounding a pseudotachylyte-bearing fault of the Gole Larghe Fault Zone (GLFZ, Adamello batholith, western Italian Alps) and to assess its coseismic nature. Then, following

the method of Pittarello et al. (2008), to estimate the total surface energy of the fractured grains formed during the seismic event. The characteristics of the fault outcrops of the GLFZ and the analytical methodologies adopted to analyse the microfractures and fragments will allow the estimate of seismic surface energy with a certain confidence. The results are then compared to fracture energy G' values from the literature (Johnson et al., 2021; Cocco et al., 2023), including seismic ruptures of actual earthquakes and, by numerical modelling, of the GLFZ ancient earthquakes (Di Toro et al., 2005a). The goal is to understand the relation of U_S with G, and with other energy sinks such as frictional heat Q.

1.2 State of the art

Introductory concepts such as how an earthquake works, its energy partitioning and how pseudotachylytes form are presented below. The significance of fracture energy G' and the different methods to estimate this quantity are briefly described.

1.2.1 Earthquakes basic concepts

Earthquakes are the result of the propagation of a shear rupture and of slip along a fault (Reid, 1910; Scholz, 2019). Potential elastic strain energy is slowly accumulated at a steady rate in the fault zone during the interseismic phase due to plate movements. When the shear stress reaches the value of the static friction μ_s on the fault ($\mu_S = \tau_p / \sigma_n$), instability is obtained on the fault surface, and seismic slip is triggered (μ_s evolves to dynamic friction μ_d during the earthquake); the accumulated stresses are suddenly released during the coseismic phase, generating an earthquake (Cocco et al., 2023). During the coseismic phase, when the rupture propagating at about 3 km s^{-1} reaches a fault patch, the shear stress evolves abruptly from τ_0 to the peak value τ_p, and then decreases to the residual value τ_{min} (dynamic weakening stage) due to energy dissipation processes (Fig. 1.1). The elastic strain energy loaded in the fault zone and in the wall rocks is dissipated during the seismic phase, fuelling the rupture propagation. When the elastic strain energy is dissipated, the slip arrests and the coseismic phase ends. This is then followed by the postseismic phase, where stresses are redistributed and aseismic slip may occur. Then, the stress loading around the fault zone starts again (a new interseismic phase begins), generating the so-called earthquake cycle (Cocco et al., 2023).
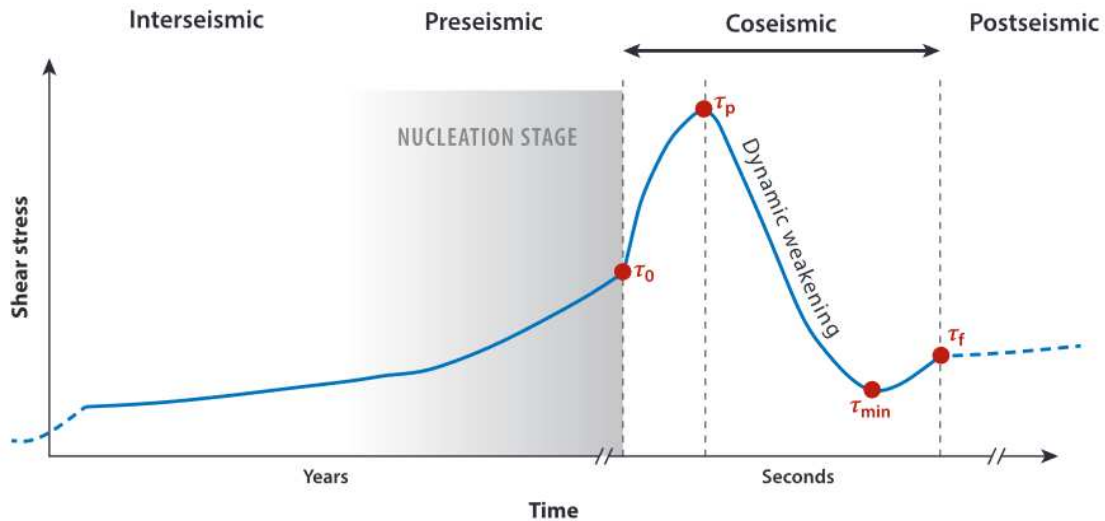
Fig. 1.1 Theoretical evolution of the stresses in time during one seismic cycle for a point on a fault. Shear stress builds up in the preseismic phase until a value τ_0, then is released and dissipated in the coseismic phase reaching a minimum value τ_{min}. The fault zone and its wall rocks loads again in the postseismic phase, starting a new seismic cycle. From Cocco et al. (2023).

Earthquakes take place in fault zones. These are constituted by one or more principal slip zones (PSZs) where the slip is localized, surrounded by the fault core (FC), a zone of highly damaged rock that accommodates most of the deformation. The fault core is embedded in the damage zone (DZ), constituted by fractured rock (Cocco et al., 2023). The fault core can reach up to some metres in thickness, while the damage zone can reach hundreds of metres (Fondriest et al., 2020a) (Fig. 1.2). Fault zones are characterized by highly deformed rocks, such as gouges, cataclasites and pseudotachylytes in the PSZ, and breccias in the FC. These are produced by the high stress perturbation associated to the passage of the seismic rupture (see Chapter 5.1) (Fig. 1.2). The rupture zone can be divided in three domains, depending on the stresses and on the slip accumulated. The first is the frontal zone, where the most of the fracturing processes occur and no slip is present; then follows an intermediate region, where the fragments are further comminuted and slip starts to accumulate, and lastly a tail region, where the slip is higher but slip velocities are significantly lower with respect to the areas in front (Fig. 1.3). The stress is extremely high at the tip and decreases rapidly moving towards the tail. The dissipation of energy takes place along all the rupture, mainly as fracture and frictional heat. Shear heating increases from the tip to the intermediate zone, until temperatures, for some earthquakes, are high enough to allow melt generation (i.e., formation of pseudotachylytes) (McKenzie and Brune, 1972; Sibson, 1975; Swanson, 1992; Di Toro et al., 2009; Ben-Zion & Dresen, 2022, preprint).
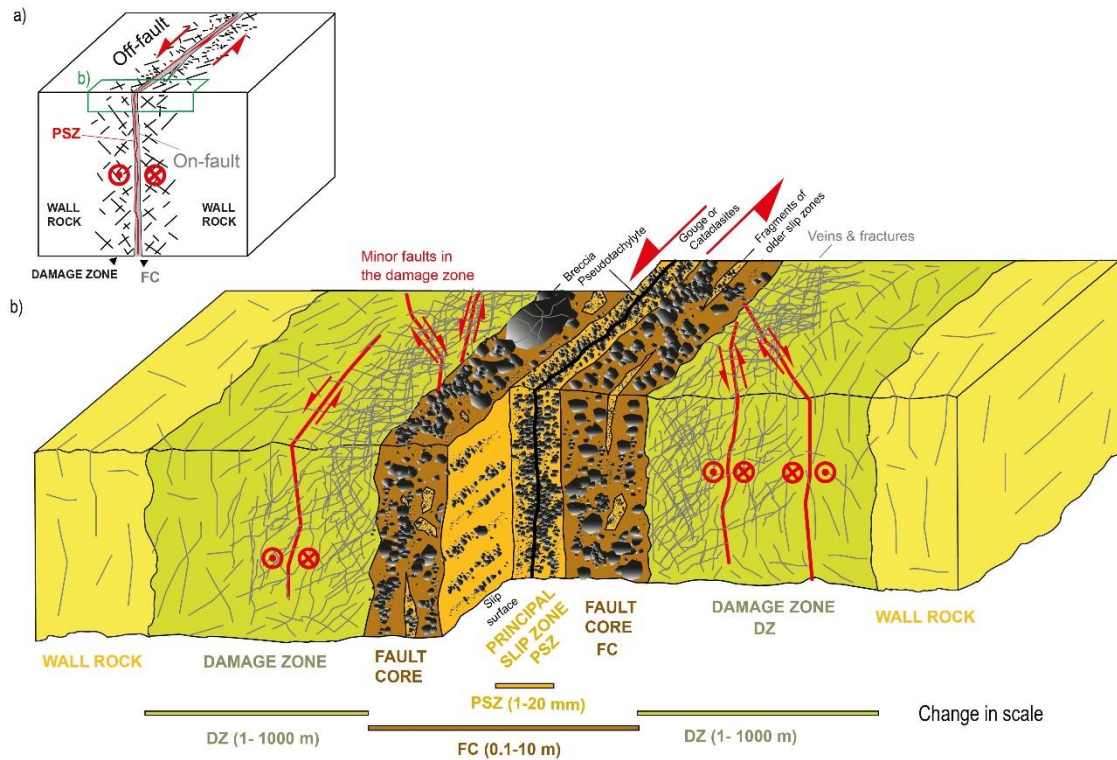
Fig. 1.2 Simplified structure of a fault zone. a) Large-scale model of a fault zone. b) Detail of the fault zone, composed by a damage zone (DZ), a fault core (FC) and a principal slip zone (PSZ). The PSZ is characterized by stress localization, slip and high comminution of the rocks (gouges, cataclasites); also pseudotachylytes are located in the PSZ (black layer). The fault core is constituted by breccias and cataclasites while the damage zone by highly fractured rock. Modified from Cocco et al. (2023).

1.2.2 Natural pseudotachylytes

Tectonic pseudotachylytes are solidified frictional melts produced during seismic slip (Sibson, 1975). For this reason, they are widely recognized as evidences of ancient earthquakes in the rock record (Cowan, 1999; Rowe and Griffith, 2015). Pseudotachylytes are formed by comminution and melting of silicate rocks at fault slip rates between 1-10 m s^{-1}. They are mostly associated to brittle deformation regimes, but there are also cases of pseudotachylytes related to ductile deformation; pseudotachylytes are mostly produced down to mid-crustal levels ($\sim$ 20 km depth), though deep-seated pseudotachylytes are not uncommon (Di Toro et al., 2009; Scambelluri et al., 2017). The present thesis is focused on pseudotachylytes produced in the upper part of the crust in the so-called brittle regime (8 – 11 km of depth). Pseudotachylytes are composed by a dark glassy matrix with embedded survival clasts of the host rock and microlites. Their composition is usually more mafic than the one of the host rocks (Chapter 2.3). Because of the high temperature achieved during frictional sliding, the viscosity of the frictional melt might be rather low and they thus may

act as lubricants during seismic slip (i.e. low values of shear resistance) (Di Toro et al., 2006). Generally, pseudotachylytes are found in the field both as fault and injection veins, with mean thicknesses ranging from some millimetres to some centimetres. However, evidences of extremely thick tectonic pseudotachylytes have also been found (Techmer et al., 1992; Menegon et al., 2021).

Pseudotachylytes are generated by frictional sliding on a fault surface. During rupture propagation, the rock is extremely fractured and comminuted; frictional melting probably occurs on the fault after << 1 mm of slip (Spray, 1995; Violay et al., 2014; Fondriest et al., 2020b). The melt is then formed and mostly extruded from the slip zone into the injection veins. Once the energy released during the earthquake is dissipated, the slip rate goes to zero and the frictional melt cools down and may weld the fault (Di Toro & Pennacchioni, 2005; Mitchell et al., 2016). The melt then cools in a time period lasting some seconds to minutes (depending on its initial temperature) and can be preserved in the rock record as a cohesive fault rock (Fig. 1.3) (Di Toro et al., 2009). The temperature of the frictional melts during their formation has been determined between 750-1450°C through different methods, such as (1) SiO_2 glass composition, (2) microlites analysis, (3) survivor clast composition, (4) textural zoning of pseudotachylyte veins, etc. and has also been measured in experiments simulating seismic slip conditions. In most cases, is assumed that frictional melting of the wall rocks happens in non-equilibrium conditions, so the melt is superheated (i.e., the melt temperature is higher than the equilibrium melting temperature of that mineral association) (Di Toro & Pennacchioni, 2004). The role of fluids in the frictional melting process is still not well understood. Fluids could be present and facilitate frictional melting, lowering the melting temperature of the rocks. Traces of fluid inclusions, vesicles etc. have in fact been found in pseudotachylytes (Gomila et al., 2021). The fluid phase could be present due to the breakdown of water-bearing minerals, or as free water in the pores. In the latter case, however, a free aqueous fluid phase could hinder frictional melt production, because its vaporization would require heat, subtracting it from the heat needed for rock melting. Also, the expansion of the vapour could decrease the normal stress applied on the fault. For these reasons, pseudotachylytes have been assumed to form in quite dry conditions (Sibson & Toy, 2006), but still evidences of frictional melting in fluid-rich conditions have been found (Gomila et al., 2021).
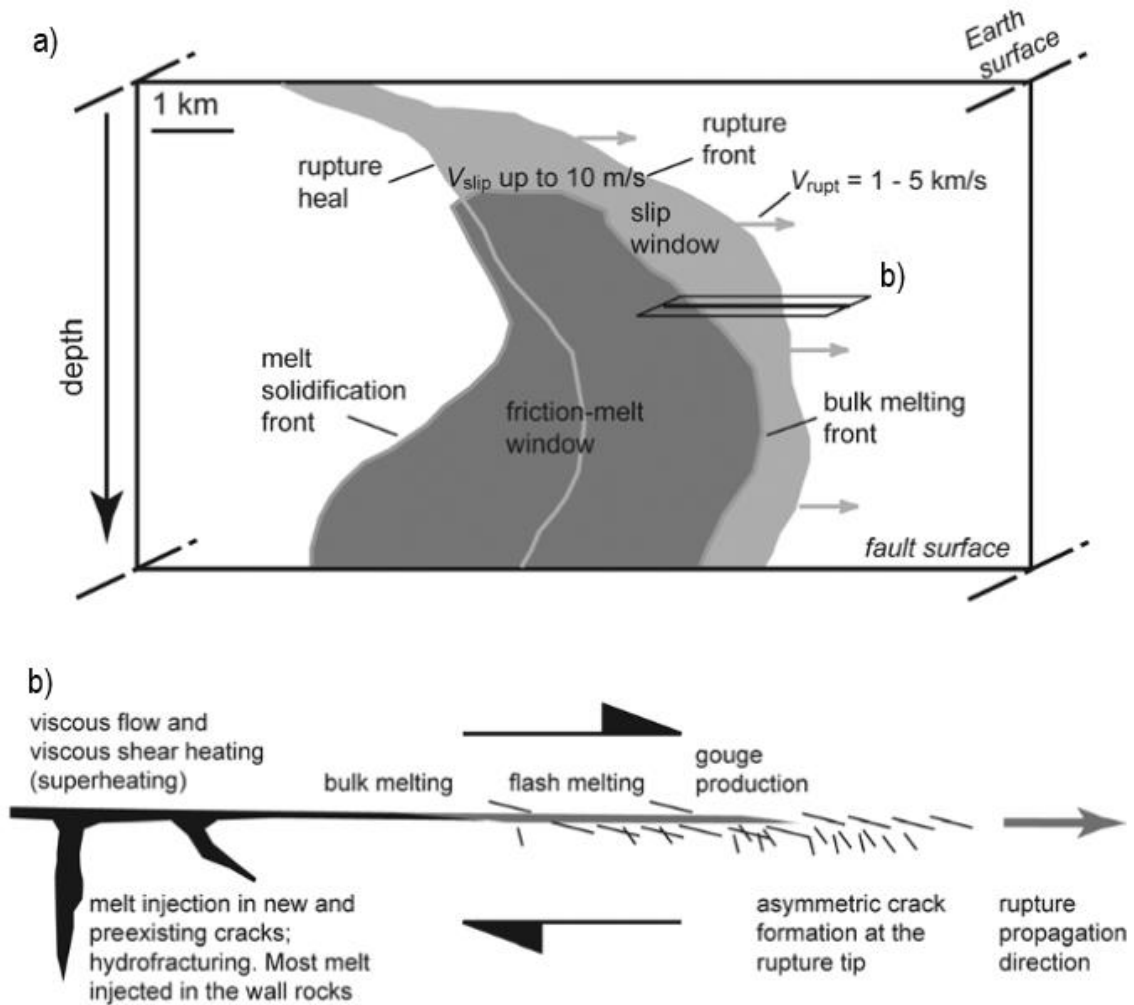
Fig. 1.3 Model of pseudotachylyte production. **a)** Model of rupture propagation, associated to a Mode II crack. The rupture propagates to the left at 1-5 km s^{-1}, and the slip follows at velocities up to 10 m s^{-1}. The melt is produced on the fault during slip, and solidifies after seconds-minutes. **b)** Close-up view of the fault section. The rupture and associated damage is followed by frictional melting and injection of the pseudotachylytes in the wall rocks. Modified from Swanson (1992).

1.2.3 Earthquake energy partitioning

The elastic strain energy stored during the inteseismic period is released suddenly during a seismic event in a timeframe of some seconds to minutes. Neglecting the work against gravity, the energy is converted into radiated energy E_R (i.e. seismic waves, a small portion of the total) and dissipation processes E_{FZ} (mainly fracture and frictional processes in the fault zone) (Cocco et al., 2023):

$$\Delta W = E_R + E_{FZ} \quad (J) \quad \text{Eq. 1.1}$$

Considering the dissipated energy for a single point on the fault it is possible to calculate the energy density W_{FZ} (i.e. work per unit area). This is composed by friction and fracture

6

processes on the fault surface and in the surrounding damage zone, respectively W_{on} and W_{off}, together with the dissipation processes at the rupture front W_G (Cocco et al., 2023):

$$W_{FZ} = W_G + W_{off} + W_{on} \quad \left(\frac{J}{m^2}\right) \quad \text{Eq. 1.2}$$

According to Pittarello et al. (2008), the energy adsorbed by a single point of the fault surface (in this case W_{on}) can also be defined as the mechanical work E_F, computed as:

$$E_F = Q + U_S \quad \left(\frac{J}{m^2}\right) \quad \text{Eq. 1.3}$$

where Q is the frictional heat and U_S the fracture surface energy (see Chapter 5.3).

The energy density dissipated in the propagation of the rupture front W_G in literature is also called the fracture energy G' (Scholz, 2019). The definition and physical significate of G' is still controversial, also due to the different results achieved in estimating it from different perspectives (geological, experimental and seismological methods). Seismic estimates of G' come from point source and extended source models, while laboratory approaches comprise shear fracture of whole samples, stick-slip, and high velocity frictional experiments (Cocco et al., 2023). Instead, fracture energy G is considered a material property, thus a constant, in fracture mechanics (Linear Elastic Fracture Mechanics) (see Scholz, 2019). For frictional models of earthquakes, it depends on the constitutive law that governs the model itself. In the latter case, G' likely includes the surface energy of the cracks generated during rupture propagation per unit fault area and non-elastic deformations at the tip of the rupture (Cocco et al., 2023). Following the most used models of earthquakes, the shear stress evolves following a slip-weakening law (Ida, 1972); with this assumption, G' becomes a slip-dependent quantity, described by the following equation (Palmer & Rice, 1973; Cocco et al., 2023):

$$G' = \int_0^{D_c} [\tau(\delta) - \tau_r]d\delta \quad \left(\frac{J}{m^2}\right) \quad \text{Eq. 1.4}$$

where δ is the slip, τ_r is the residual stress, and D_c the slip-weakening distance. For the slip-weakening model, the decrease of shear stress from the peak value τ_p to the residual value τ_r is linear over the slip-weakening distance, so Eq. 1.6 can be written as (Cocco et al., 2023):

$$G' = \frac{1}{2}\left(\tau_p - \tau_r\right) D_c = \frac{1}{2}\Delta\tau_b D_c \quad \left(\frac{J}{m^2}\right) \quad \text{Eq. 1.5}$$

with $\Delta\tau_b$ the breakdown stress drop. The fracture energy G' can thus be described also as the energy needed for the advancement of the rupture at a certain velocity (Cocco et al., 2023). In slip-weakening models, G' is the area in the shear stress vs. coseismic slip graph comprised between the shear stress evolution curve and the residual shear stress τ_r (Fig. 1.4). As the theoretical formulations (Eq. 1.4 and 1.5), seismological and experimental estimates of fracture energy G' evidence its power-law dependence with slip distance δ (Fig. 1.5) (Nielsen et al., 2016; Passelègue et al., 2016):

$$G' \propto \delta^a \quad \text{Eq. 1.6}$$

where a is a value often near to 1. Also, if the earthquake rupture is modelled as a propagating Mode II fracture (Fig 1.3a) G' increases with loading and confining stresses on the fault surface (Wong, 1982). These two statements contrast with how LEFM describes fracture energy G, so the difficulty in determining exactly what G' signifies is evident.
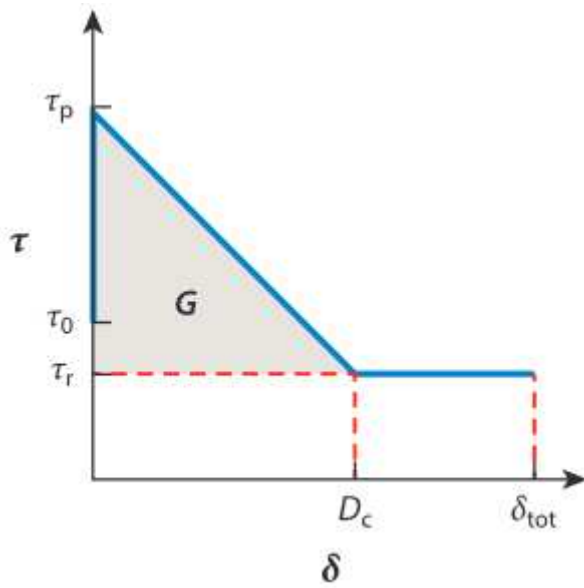

Fig. 1.4 Diagram of the shear stress evolution for a point on a fault, following the slip-weakening law. Fracture energy G can be approximated as the grey area under the blue curve and above the residual stress τ_r (Eq. 1.7). The white area below τ_r is often assumed as the frictional heat dissipated during the seismic event. Modified from Cocco et al. (2023).

Geological estimates of the damage produced both off and on fault during rupture propagation (W_{off} and W_{on}, respectively) are normally based on the calculation of the newly generated surface area of the fragmented domain per unit fault area produced by the rupture propagation (Chester et al., 2005; Pittarello et al., 2008). Geological analysis can also allow the calculation of the frictional heat if pseudotachylytes are present (Pittarello et al., 2008). In both cases, many assumptions have to be made (constant value of some parameters during the earthquake such as normal stress, or the absence of processes such recrystallization that could modify the grainsize distributions, etc.) (Cocco et al., 2023). In the present thesis, the

geological approach was adopted to estimate U_S, its relation with the dissipated frictional heat Q and its significate with respect to the seismological fracture energy G'.
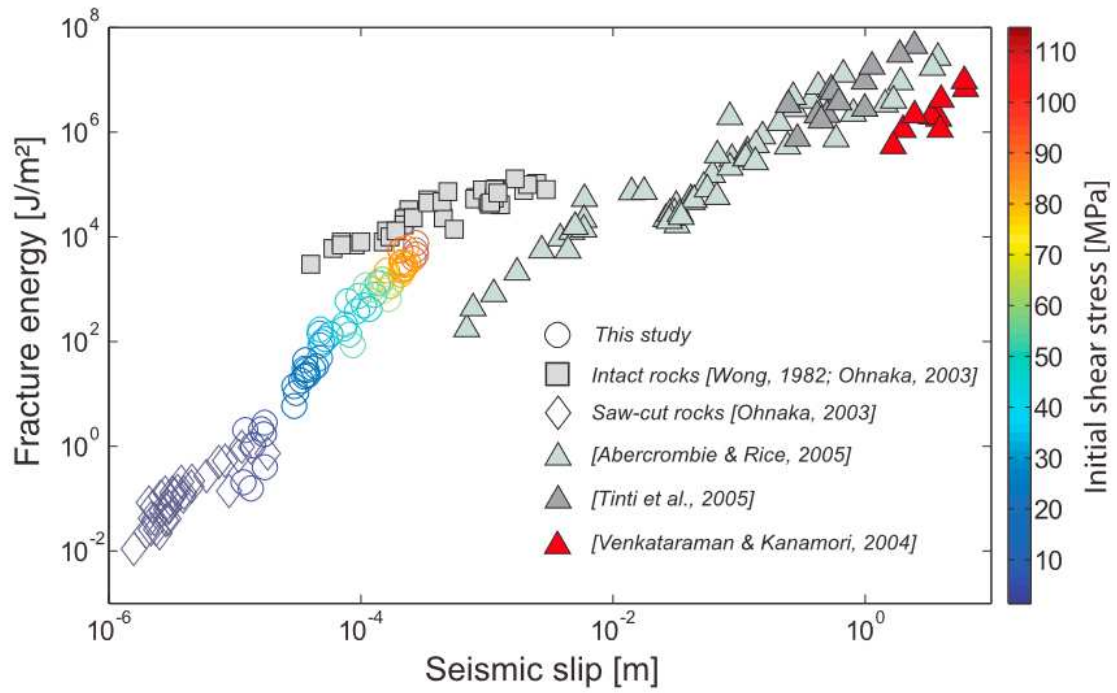

Fig. 1.5 Fracture energy dependence with seismic slip from experimental and seismological analysis. Seismological (e.g., Tinti et al., 2005; Abercrombie and Rice, 2005) and experimental estimates of G' are comparable over several orders of magnitude of seismic slip. From Passelègue et al. (2016).

2. Geological setting

The samples studied in the present thesis were collected from a pseudotachylyte-bearing fault of the Gole Larghe Fault Zone, in the Adamello batholith, northern Italy. A brief description of the geological background of the area is presented in this Chapter, as well as a description of the faulting conditions and characteristics of the pseudotachylytes found there.

2.1 Adamello batholith

The Adamello batholith is the biggest (~670 km^2) Tertiary post-collisional magmatic intrusion of the Alpine chain. It intruded in the Permian basement and Permian to Mesozoic unmetamorphosed units of the Southern Alps between 42 – 30 Ma (Del Moro et al., 1983; Callegari & Brack, 2002). The intrusion is located at the junction between the Tonale Line to the north and the Giudicarie Line to the east (Fig. 2.1). The first is a dextral strike-slip fault, a segment of the Periadriatic Line, while the latter a sinistral transpressive fault (Schaltegger et al., 2019).

The Adamello intrusion is composed of four main units divided by sharp boundaries: Re di Castello, Adamello, Avio and Presanella, in turn formed by smaller intrusions (Fig. 2.1). The batholith is the result of different degrees of crustal assimilation and crystal fractionation processes that from similar parental mantle magmas generated the different units (Callegari & Brack, 2002; Schaltegger et al., 2019). The four units have slightly different composition but are generally composed of acid igneous rocks ranging from granodiorites to tonalites, with minor leucotonalites and diorites (Callegari & Brack, 2002). Age determination of the different bodies made with ^{39}Ar/^{40}Ar dating methods reports the following results (Schaltegger et al., 2019):

I.   Re di Castello: 42 – 38 Ma, fine grained granodioritic to tonalitic rocks;
II. Adamello: 36 – 34 Ma, coarse grained hornblende- and biotite-tonalites to leucotonalites;
III. Avio: 34 – 32 Ma, medium grained biotite-tonalites;
IV. Presanella: 33 – 29 Ma, coarse grain hornblende- and biotite-tonalites.

The magmatic suite also comprehends minor bodies of gabbroic rocks found mainly at the borders of the batholith and is cut by aplitic and pegmatitic dykes. A more detailed

classification of the units can be found in Schaltegger et al., 2019, based on U/Pb and $^{40}Ar/^{39}Ar$ dating.
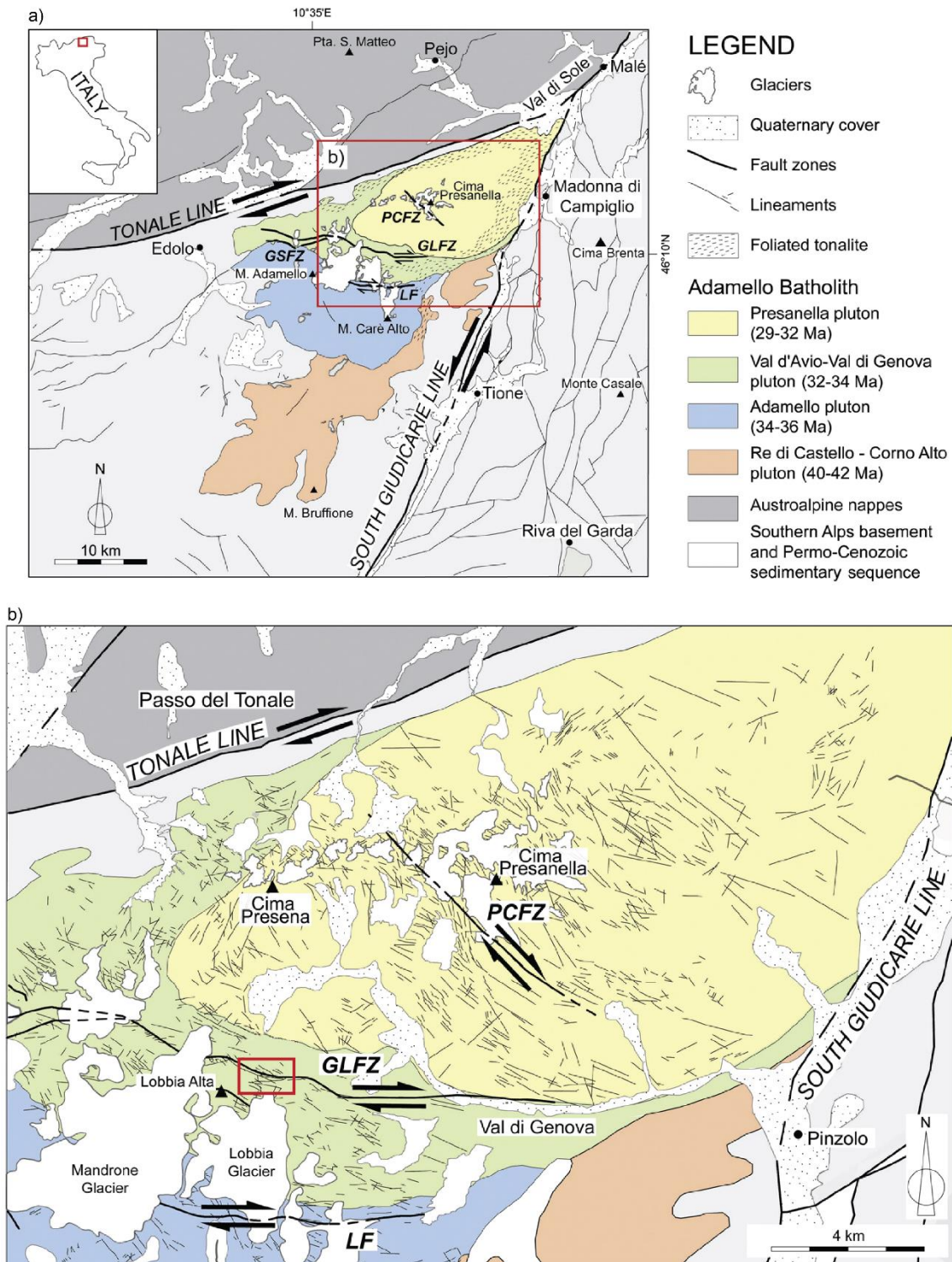

Fig. 2.1 Schematic illustration of the geological setting of the Adamello massif. **a)** Simplified map of the four main units; GLFZ = Gole Larghe Fault Zone, GSFZ = Gole Strette Fault Zone, LF = Lares Fault, PCFZ = Passo Cercen Fault Zone. **b)** Schematic structural map of the GLFZ and surroundings. The red square represents the location of the pseudotachylyte-bearing fault selected for this thesis, pictured in Fig. 4.1. Modified from Smith et al. (2013).

The ages are consistent with the ones determined by K/Ar and Rb/Sr dating in Del Moro et al. (1983). Both these studies show an evident age-decreasing trend from the Re di Castello unit in the south to the Presanella unit in the north (Callegari & Brack, 2002).

Evidence of contact metamorphism is widespread along the borders of the intrusion, with an aureole that extends generally for 1 – 2 km in the different lithologies surrounding the Adamello. Tonalites and granodiorites near the limits of the intrusive body show igneous and tectonic foliations (especially the Presanella unit) as a result of the emplacement during the activity of the Periadriatic Line, locally expressed on the Tonale and Giudicarie faults. The Tonale fault was active also afterwards (Stipp et al., 2002; Pennacchioni et al., 2006; Mittempergher et al., 2022). The conditions of emplacement of the Adamello intrusion are suggested by metamorphic mineral assemblages in the rocks constituting the metamorphic aureole. Assemblages of quartz + andalusite + muscovite + K-feldspar (+ water) and evidences of andalusite to sillimanite metamorphic reaction mark ambient pressures between $0.25 - 0.30$ GPa, and temperatures around 250°C. This corresponds to shallow crustal depths of 8 – 11 km (Stipp et al., 2002; Pennacchioni et al., 2006; Mittempergher et al., 2022). The cooling rate of the intrusion from emplacement temperatures of ~ 300°C was quite fast, estimated in ~ 100°C/Ma (Del Moro et al., 1983; Pennacchioni et al., 2006; Schaltegger et al., 2019).

2.2 Gole Larghe Fault Zone

The Gole Larghe Fault Zone is a ~ 20 km dextral transpressive fault trending E-W in the Avio body, with a mean dip of 50° to N190°, an estimated offset of 1 km and thickness of ~ 550 m. It is a strand of the Tonale Line system, and is likely connected also to the Giudicarie Line to the E (Pennacchioni et al., 2006). The solid state deformation of the Avio body occurred between its emplacement (36 – 34 Ma) and exhumation (29 – 20 Ma), and in particular faulting around 30 Ma, at conditions similar to the ones of its emplacement (Di Toro & Pennacchioni, 2004; Di Toro et al., 2005a; Pennacchioni et al., 2006; Mittempergher et al., 2022). The GLFZ is composed of thousands of major and minor subparallel faults, with thickness between 0.01 – 1 m and spacing that ranges from 1 m to 5 m. The associated fault rocks are cataclasites to ultracataclasites and pseudotachylytes. There are no evidences of successive extensive reactivation of the fault zone and of tilting during exhumation (Di Toro & Pennacchioni, 2004, 2005; Pennacchioni et al., 2006). Four main deformation stages

can be inferred from field relationships, occurred during the cooling history and coeval exhumation of the pluton (Fig. 2.2):

I. Magmatic joints (> 600°C): late magmatic features, organized in two main orthogonal systems with conjugate sets. A first one trending ESE-WNW, and a second one, NNE-SSW. These are divided in major and minor joints, that crosscut magmatic features such as aplitic and pegmatitic dykes. Often they are decorated by unaltered biotite and hornblende lineations, that indicate high temperatures of formation (Pennacchioni et al., 2006);

II. Shear zones (550 – 450°C): ductile reactivation of the magmatic joints, forming coeval N-S and E-W striking shear zones, respectively of sinistral and dextral sense of shear. The major shear zones are surrounded by mylonitic fabric in the tonalites, while the smaller ones often are thin without widespread ductile deformation of the host rock (Pennacchioni et al., 2006);

III. First brittle reactivation phase (300 – 250°C): dextral transpressive reactivation of the E-W joint family and shear zones, with formation of epidote- and chlorite-bearing cataclasites to ultracataclasites, also thanks to fluid circulation (the latter resulted also in the precipitation of K-bearing veins). These features show dextral slip and have a mean orientation of 50° to N195°. Cataclasite-bearing faults are frequently found in association with pseudotachylytes, evidence of the seismogenic nature of the faults (Pennacchioni et al., 2006). The cataclastic deformation took place at sub-greenschist facies conditions (Di Toro & Pennacchioni, 2004, 2005);

IV. Late brittle reactivation phase (< 200°C): reactivation of the N-S mylonitic shear zones and of the E-W cataclastic faults and cooling joints as a network of zeolite-bearing faults. These have different kinematics, from sinistral strike-slip (the N-S family) to both normal and reverse (E-W family). The intersection between these leading fault fractures often forms metre-thick damage zones filled by zeolite minerals and minor Fe-oxides. These features are generally evidenced by the whitish to reddish colour of the zeolites and their preferential erosion (Dempsey et al., 2014).

For more detailed structural data, please refer to Pennacchioni et al. (2006).
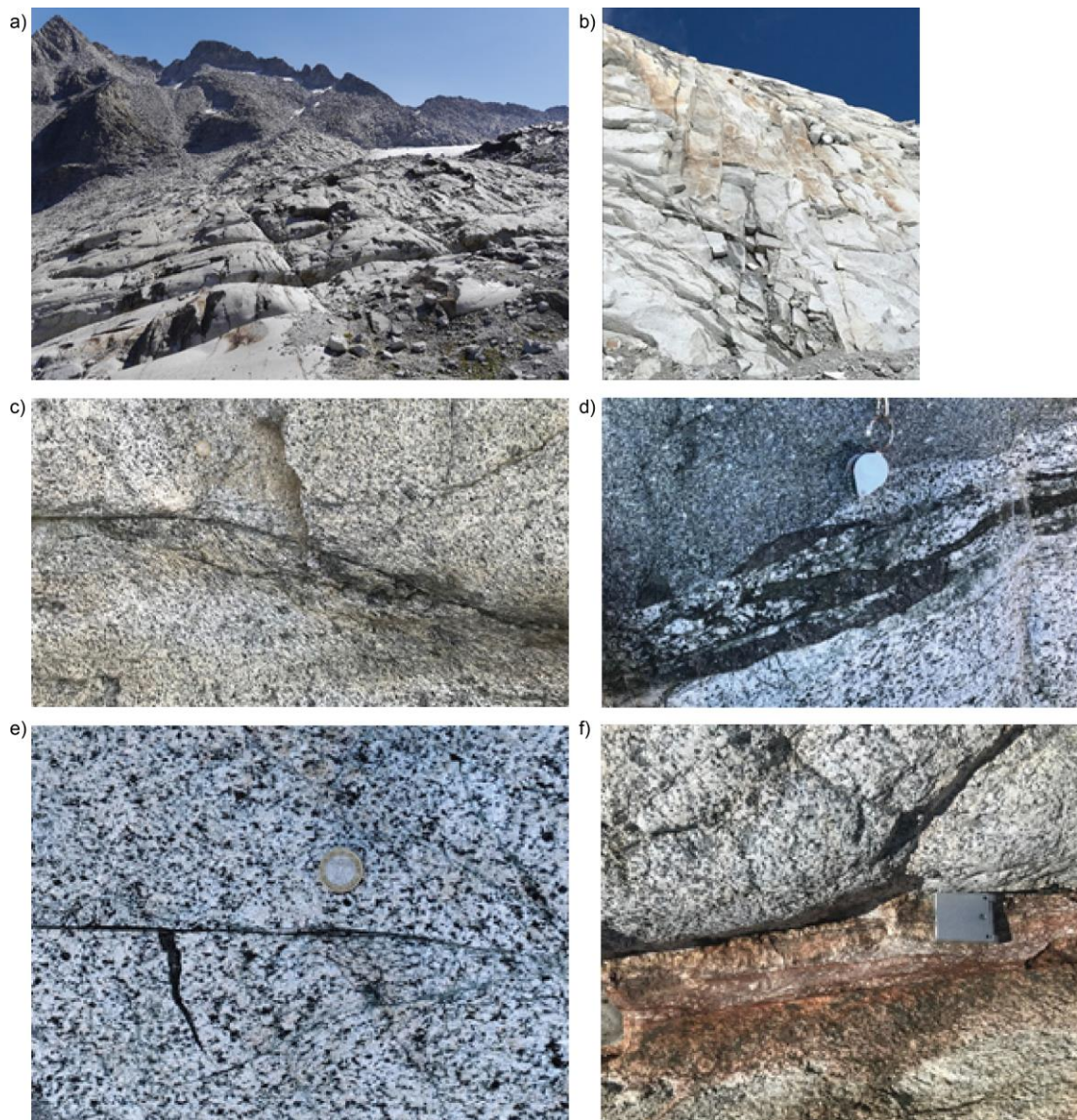
Fig. 2.2 Field photos of the Gole Larghe Fault Zone and its main deformation structures. **a)** Polished outcrops of the GLFZ at the base of the Lobbia Glacier. It is possible to see already some major faults cutting in E-W direction the tonalites. North to the left. **b)** Magmatic joints. **c)** Ductile shear zone with sinistral shear sense. **d)** Cataclasite and psueodtachylyte-bearing fault between tonalite and a mafic body. **e)** Pseudotachylyte-bearing fault and injection vein. **f)** Zeolite-bearing fault, with the characteristic reddish colour.

2.3 Pseudotachylytes of the GLFZ

Tectonic pseudotachylytes are solidified friction melts produced during seismic slip (Sibson, 1975). In the Gole Larghe Fault Zone these are found both as fault and injection veins. They have thickness ranging from millimetres to some centimetres, except when they

14

infill local extensional features such as pull apart or extensional domains (also called dilational jogs), where they can reach up to 20 cm in thickness (Di Toro & Pennacchioni, 2004; Di Toro et al., 2005b). Pseudotachylyte-bearing faults can either show or not a cataclastic precursor. The fault veins are normally located at the cataclasite-tonalite boundary, with sharp contacts in both cases. The geometry of the fault veins and the associated injection vein network is concordant with the sense of shear evidenced by cataclasites and by the separation of structural markers (mylonites, dykes and magmatic enclaves) (Di Toro & Pennacchioni, 2004). Veins thinner than few millimetres are quite homogeneous and blackish in colour, while thicker pseudotachylytes are zoned with a dark green to blackish inner layer bounded by rims black in colour, interpreted as chilled margins (Di Toro & Pennacchioni, 2004). Some pseudotachylytes are altered under sub-greenschist conditions due to metamorphic fluids circulation and acquire a dark green to whitish purple colour (Di Toro & Pennacchioni, 2004; Fondriest et al., 2020b). All pseudotachylytes overprint or cut magmatic joints, dykes and mylonites. Instead, the pseudotachylytes cut and are cut by sub-greenschists facies cataclasites and are cut systematically by zeolite-bearing veins and faults. In some faults, pseudotachylytes are well-preserved, fresh-looking and overprint the cataclasites, meaning they were the last event coseismic slip phase recorded (Di Toro and Pennacchioni 2004, 2005, Pennacchioni et al., 2006). Instead, the sub-greenschist facies cataclasites accommodated deformation by both cataclasis and pressure-solution (mainly in quartz) and precipitation (mainly of chlorite) and may record both interseismic and seismic phases (Di Toro and Pennacchioni, 2005).

The bulk chemical composition of the pseudotachylytes reflects the melting of tonalite-forming minerals depending on their melting temperatures. Analysis show that the matrix of the pseudotachylytes is more mafic than the host rock. It is enriched in MgO, FeO and K_2O with respect to the surrounding rocks and cataclasites, due to the preferential melting of biotite, chlorite and K-feldspar. They are instead relatively depleted in SiO_2 because quartz grains are preferentially conserved as clasts in the melt, thanks to their higher melting temperature, not reached by the frictional melts (1730°C vs 1250-1450°C). These evidences support a disequilibrium melting process happening during pseudotachylyte formation (O'Hara, 1992; Di Toro et al., 2009; Mittempergher et al., 2022).

The majority of injection veins in the individual faults of GLFZ (average strike E-W) is found in the southern wall rocks. This asymmetric distribution is interpreted as the result of the stress perturbation associated with the propagation at few km s^{-1} of the seismic rupture

(Mode II-III cracks) (Chapter 5.1). In fact, ruptures propagating along the GLFZ from W towards E, given the dextral transpressive sense of shear, would result in a large (up to GPa) transient tensional stress field in the southern wall rocks and in a compressional one in the northern wall rocks. Given the much lower strength of rocks under tension (~10 MPa vs ~200 MPa for a granite), injection veins opened more easily on the southern wall rocks. This interpretation is supported also by numerical models, other than systematic field observation both at the outcrop scale and microscale (Fig. 2.3) (Di Toro et al., 2005a).
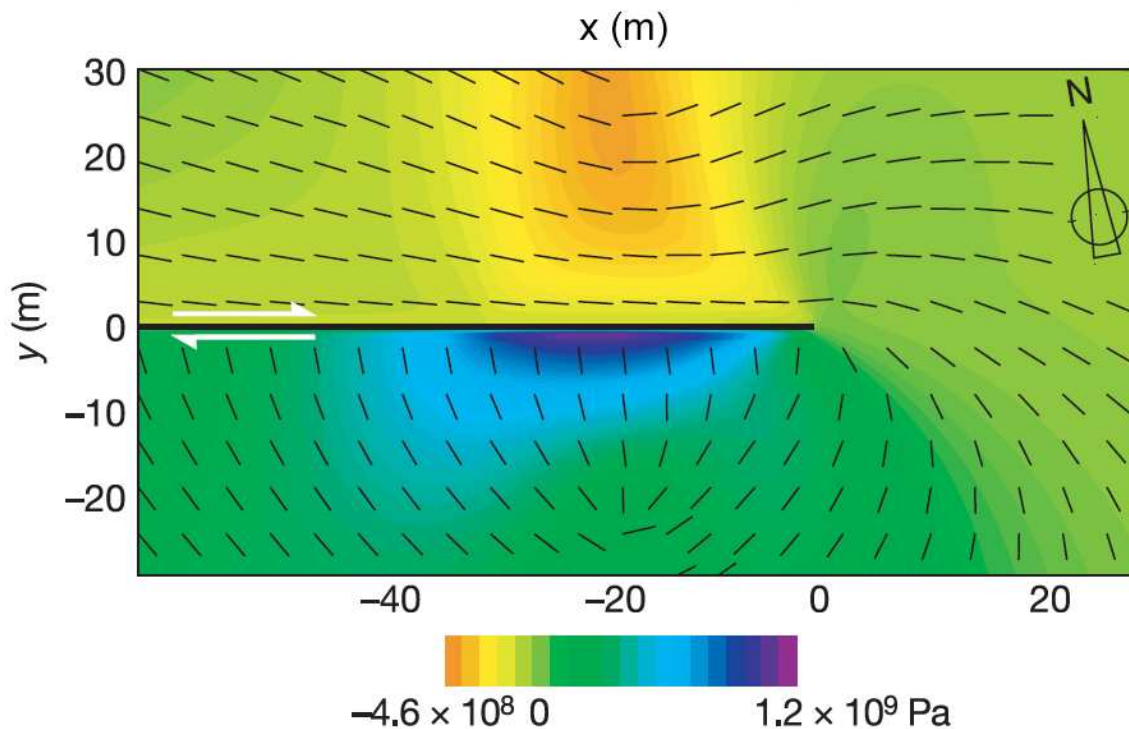
Fig. 2.3 Stress field simulation around a dextral strike slip fault. The fracture tip is represented by the black line; rupture velocity $v = 0.9v_s$. Colorbar for stress magnitude; note the maximum tension planes oriented orthogonally to the fault surface in the S wall, coincident with the strike of the majority of the injection veins found in the field. Modified from Di Toro et al., 2005a.

The age of faulting and therefore of pseudotachylyte production can be constrained by [39]Ar-[40]Ar dating of bulk pseudotachylyte samples; these record an age of 30 Ma for the seismic event (Pennacchioni et al., 2006). More recent dating of pseudotachylyte samples confirm the previous estimates, recording ages between 29 – 32 Ma. However, samples of ~ 25 Ma have been found, meaning that the seismogenic activity of the faults probably lasted at least 3 Ma longer than previously assessed (Mittempergher et al., 2022). Microstructural evidences such as plasticity of quartz around the pseudotachylyte veins, as well as the mineral assemblage found in cataclasites (K-felspar + epidote + chlorite) help to constrain the depth

of the faults during the seismic event (8 – 11 km, very similar to the depth of emplacement of the pluton) (Di Toro & Pennacchioni, 2004, 2005; Pennacchioni et al., 2006; Mittempergher et al., 2022). The exhumation of the igneous body happened around 22 Ma, therefore after the earthquakes responsible for the formation of the pseudotachylytes.

3. Methods

Five samples were selected for the microstructural analysis: one experimental sample and four natural samples of a fault segment in the GLFZ. This allowed me to compare microfractures produced under different loading conditions and environment, and to understand the role of rupture propagation in the generation of microfracture patterns. In this Chapter the methods used for microfracture data collection and elaboration are described, as well as the imposed experimental conditions to produce the artificial pseudotachylyte.

The pseudotachylyte-bearing fault samples were first retrieved from the GLFZ outcrop and thin sectioned. Preliminary investigations with optical microscopy were carried out, and successively in-depth microstructural investigations by means of FESEM imaging, to collect microimages of the microfractures and of the grains. These microimages were elaborated through image analysis software to determine the microfracture pattern and the size and distribution of the grains. Dedicated MATLAB® scripts and toolboxes were then used to obtain quantitative information. Results are presented in Chapter 4.

3.1 Field sampling procedure

The natural samples analysed in the present thesis were collected from a single pseudotachylyte-bearing fault of the Gole Larghe Fault Zone (Fig. 4.1). The criteria of selection of this particular fault, also discussed in Griffith et al. (2010), are described in Chapter 4.1. Three slabs of rock, WF22-01, WF22-02, WF22-03, respectively of 40 x 12 cm, 40 x 10 cm, 30 x 14 cm were extracted from the fault with drills and rock extractors in the field survey of 8th October 2022. (Fig. 4.2). Shape and position of the rock slabs were chosen to recover the fault slip zone and at least 10 cm of wall rocks on both fault sides, to analyse the microfracture pattern distribution and its variation from the slip zone towards the less deformed wall rocks. In particular, sample WF22-01 was extracted 10 cm to the east of the cylindrical core sample L05-08, collected and discussed by Griffith et al. (2010) (Fig. 4.2).

3.2 Experimental procedure

The experimental pseudotachylyte of sample HVR376 was produced with the high-velocity rotary shear machine HV-1 (Shimamoto and Tsutsumi, 1994) installed in Kyoto, Japan (Di Toro et al., 2006). Two cylinders of 22 mm of diameter and 23 mm in length of

the wall rock tonalite from the GLFZ were put in contact under a normal stress σ_n of 15 MPa and sheared at room humidity conditions at an equivalent slip rate of 1.28 m/s for a slip distance of few metres (Di Toro et al., 2006) . In particular, the specimen HVR376 is composed by two juxtaposed cylinders ("pre-cut" samples), where the contact surface simulates the fault. The sample is cased with a 1 mm-thick aluminium ring to confine the rock cylinder and prevent sample destruction by thermal fracturing. The arrow indicates the stationary side (N) while the opposite one is the rotational side (S). (Fig. 3.1). Rotation of the left halve of the sample imposes slip displacement along the experimental fault surface, that can be unlimited thanks to the rotary configuration. During sliding, melt is produced by frictional heating along the rubbing rock surfaces, forming fault and injection vein-type pseudotachylytes similar to those found in nature.
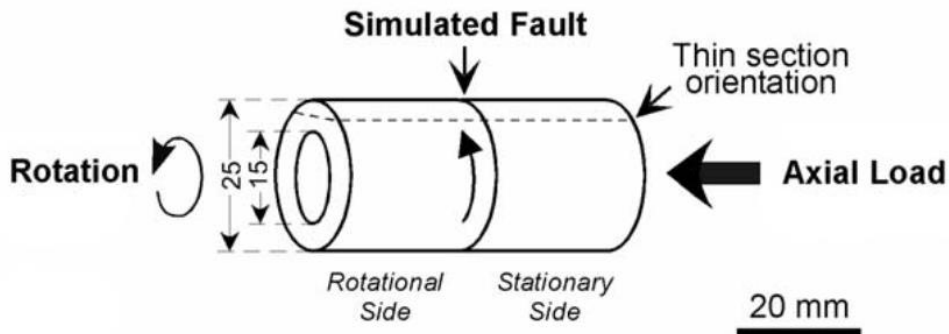
Fig. 3.1 Sketch of the experimental sample asset for high-velocity shear experiments. In the thin section of sample HVR376 the stationary side is on top (N). Modified from Hirose and Shimamoto (2005).

3.3 Samples and thin section preparation

Slab WF22-02 and WF22-03 broke in pieces during field sampling and were reassembled with instant glue. Instead, rock slab WF22-01 did not report any evident damage and was selected to produce polished samples and thin sections. The rock slab was then consolidated with epoxy, resized and cut in half with a diamond saw. The cut was parallel to the outcrop surface and perpendicular to the fault surface. The two resulting halves were polished and the thinner one used to produce 30 µm thin sections (WF22-01a, WF22-01b, WF22-01c) for microstructural analysis (Fig. 4.3). The position of the thin sections was chosen to investigate the fault slip zone and ~ 3 cm of wall rocks on both sides of the fault (Fig. 3.2).

Fig. 3.2 Sample WF22-01 with location of the three thin sections: from N to S WF22-01a, WF22-01b, WF22-01c. WF22-01a and c are from the wall rock, while WF22-01b contains the ~ 2 mm thick pseudotachylyte-fault vein. To the right of the thin sections is located an injection vein intruding the southern wall rock.

A thin section from the drill core L05-08 was available at the Department of Geosciences from previous studies (Griffith et al., 2010; Lazari et al., 2023), as well as a thin section of the experimental sample HVR376 (Di Toro et al., 2006) (see Appendix A). The first is 30 µm-thick and the other ~50 µm-thick.

Optical microscope photographs were taken with a Canon EOS 550D camera at different magnifications. After investigation at the optical microscope, all thin sections (WF22-01a, WF22-01b, WF22-01c, L05-08, HVR376) were polished with Syton® and successively coated with a 10 nm carbon layer for analysis at the FESEM.

3.4 Field Emission Scanning Electron Microscope (FESEM)

After preliminary investigations of the thin sections carried out with an optical petrographic microscope, all the microstructural investigations were performed with a TESCAN SOLARIS dual beam Focused Ion Beam – Field Emission – Scanning Electron Microscope (FIB-FESEM) available at the Department of Geosciences. Microstructural characterization of the samples was systematically performed in Back Scatter Electrons

(BSE) and Cathodoluminescence (CL) modes, but complementary investigations at different working conditions were also performed:

I. FESEM-CL for in-depth characterization of all the samples, and performed at 15 mm working distance, 10 keV accelerating voltage, 3 nA beam current;

II. FESEM-SE (Secondary Electrons) for collecting reference images, which were acquired at 15 mm of working distance, 10 keV accelerating voltage, 3 nA beam current;

III. FESEM-EBSD (Electron Back Scattered Diffraction) for acquiring two EBSD maps at 16 mm working distance, 20 keV accelerating voltage, 5 nA beam current and a step size of 0.5 μm;

IV. FESEM-BSE for collecting BSE images which were acquired at 5 mm of working distance, 20 keV accelerating voltage, 5 nA beam current. Moreover, high resolution mid-angle BSE images were instead acquired at 4 mm working distance, 5 keV and 300 pA beam current.

Standard observations of the thin sections through optical and electron-BSE techniques are not suited to evidence the pervasiveness, down to the nanoscale, of the microfracture pattern in the wall rocks surrounding the pseudotachylyte fault and injection veins. This is because the microfractures are healed/sealed by a second generation of the hosting mineral, likely due to mineral precipitation from postseismic fluid circulation (Bestmann & Pennacchioni, 2015; Bestmann et al., 2016). Hence, the two mineral generations (in this case, magmatic and co- to postseismic) are not distinguishable through the techniques mentioned above, except in few cases where the microfractures are decorated by trails of small fluid inclusions (as those studied by Griffith et al., 2010). As evidenced by other studies conducted along the GLFZ on pseudotachylyte-bearing faults and associated damage zones, FESEM Cathodoluminescence detects the various generations of microfractures (Bestmann et al., 2012, 2016). In fact, the microfractures cutting magmatic minerals (quartz, plagioclase and K-feldspar) of the Avio tonalites have a darker shade of grey when observed through FESEM-CL. In the case of quartz, this is due to the different Ti content (and possible lattice defects) in the quartz sealing the microfractures with respect to the magmatic quartz. The healed microfracture have Ti contents of $10 - 13$ ppm while the neighbour quartz grains of $35 - 55$ ppm (Bestmann et al., 2016). Instead, in the case of feldspars, the origin of the different FESEM-CL signal associated with the microfractures is a matter of debate. Whatever the case, given the high magnification with respect to the optical

microscopes, FESEM-CL is then the state-of-the-art technique to investigate these microfractures, and it has been adopted as the core methodology in this thesis.

The microfractures isolate fragments of host minerals with dimensions ranging between ~ 90 nm to 0.8 mm in diameter and thus over several orders of magnitude. The fragments down to ~ 500 μm can be investigated trough FESEM-CL, but the finest fragments, down to < 90 nm, cannot be detected with FESEM-CL, due to its resolution limits. To overcome this problem, images of the smaller fragments were acquired through EBSD and high resolution mid-angle BSE microimaging of selected regions of sample L05-08. The EBSD microimaging allowed me to discriminate fragments depending on their crystallographic orientation. However, even if the FESEM-EBSD has a higher resolution than the FESEM-CL, it cannot detect fragments below ~ 1 μm. To overcome this fragment size limit, high resolution mid-angle BSE images have been acquired, which allowed me to identify fragments down to ~ 90 nm in diameter.

3.5 Image analysis

Images acquired with the FESEM are used for the quantitative description of:

- *microfracture pattern:* orientation, fracture density, gradient towards the host rock etc., associated with the pseudotachylyte-bearing fault. These data are required to discuss seismic rupture, and
- *fragments isolated by the microfractures:* Clast Size Distribution (CSD) curves, surface area of the fragments, etc. These data are instead required to estimate the fracture surface energy U_S.

The methods to process the images to obtain the microfracture pattern data and to detect the fragment/grain boundaries are described below.

3.5.1 Microfractures

Ten FESEM-CL images of natural samples L05-08 and WF22-01 a, b, c, were selected to characterize the microfractures. The images at increasing distance from the fault surface (from 0 to 22 mm, see Table 3.1 and Appendix A). Automatic processing of the images was not possible due to the extreme complexity of the microfracture patterns. Machine learning and artificial intelligence techniques were also not considered because of the limited number

of FESEM-CL images and the limited time available for training the algorithm. The microfractures were thus drawn one by one by hand on the FESEM-CL images with AutoCAD®, a commercial computer-aided design software, on a representative area of 1.64 mm² (the area of a single image), which included quartz, plagioclase and K-feldspar grains.

Table 3.1. FESEM-CL images selected for image analysis with position with respect to the geographic north and distance with respect to the pseudotachylyte fault vein-wall rock contact.

IMAGE CODE	SAMPLE	SIDE (with respect to the fault vein)	DISTANCE (from the fault vein)
1	HVR376	N	0 mm
2	HVR376	S	0 mm
2	L05-08	N	5 mm
3	L05-08	S	0 mm
5	L05-08	N	0 mm
13	L05-08	S	7 mm
2	WF22-01a	N	20 mm
1	WF22-01b	N	0 mm
3	WF22-01b	S	0 mm
2	WF22-01c	S	22 mm

The lines depicting the microfracture pattern were first manually drawn on the image and then divided in segments of constant length (10 µm) with the open source Lisp command MeasureBreak (Fig. 3.3). In CAD software, the Lisp (list processing) language is employed to automate the drawing procedures and to expand and customize the functionality of the software. In this case the Lisp was used to automate the subdivision process of the lines (i.e. the microfractures). This line segmentation allowed me to give comparable importance to the longer and shorter microfractures: for instance, one rectilinear microfracture described by a single 50 µm long segment had the same statistical weight of five short rectilinear microfractures of 10 µm in length each. This approach yielded a robust estimate of the fracture orientation frequency. All the microfractures smaller than 10 µm were ignored because poorly visible in the images. In the areas near to the fault and injection veins the pattern is very complex and the minerals are highly fractured, so a specific trend cannot be individuated; these were thus ignored in the computation of the microfractures characteristics, while they were considered for the fragments size distributions (Fig. 3.3 vs. 3.4).
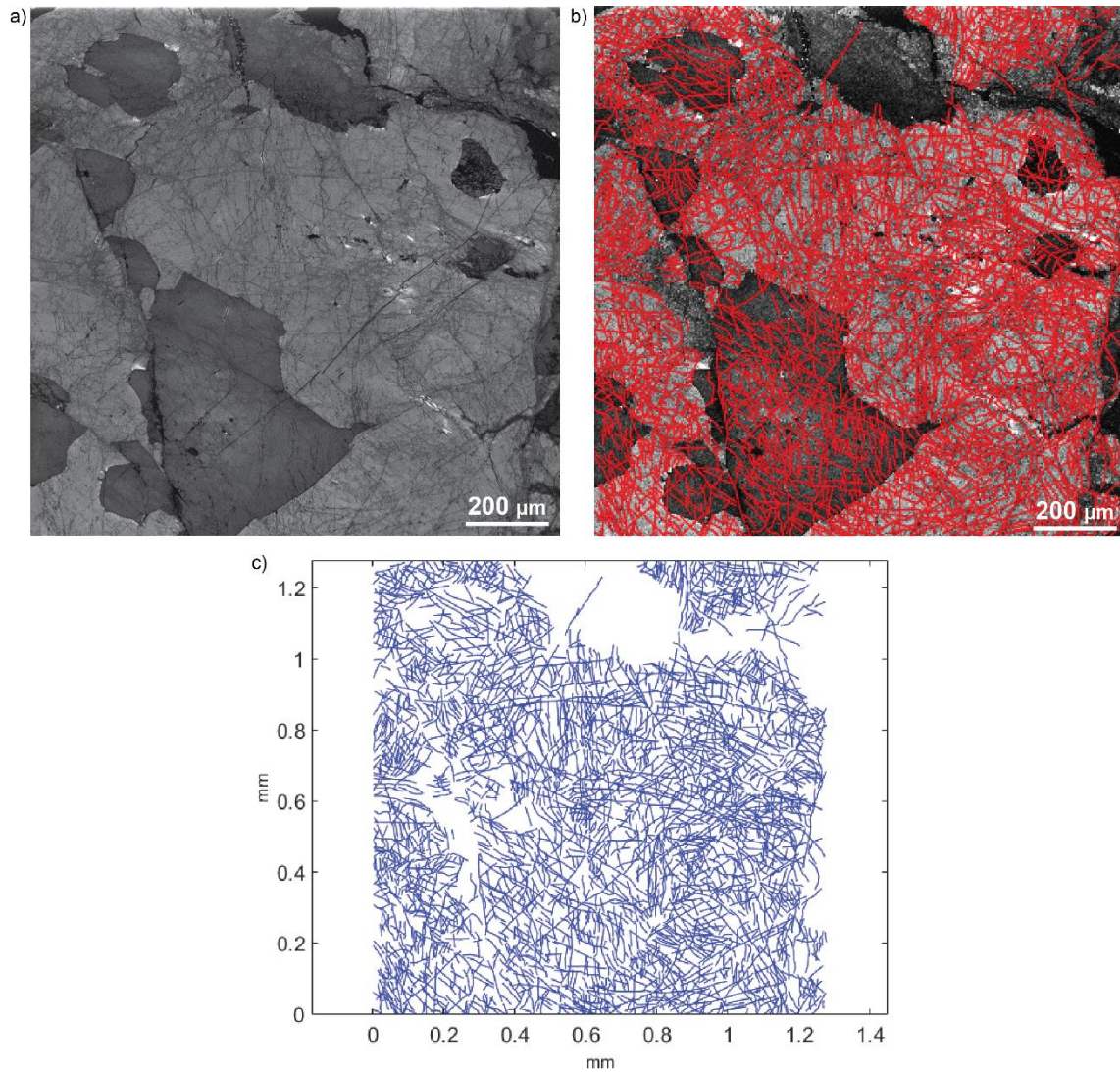
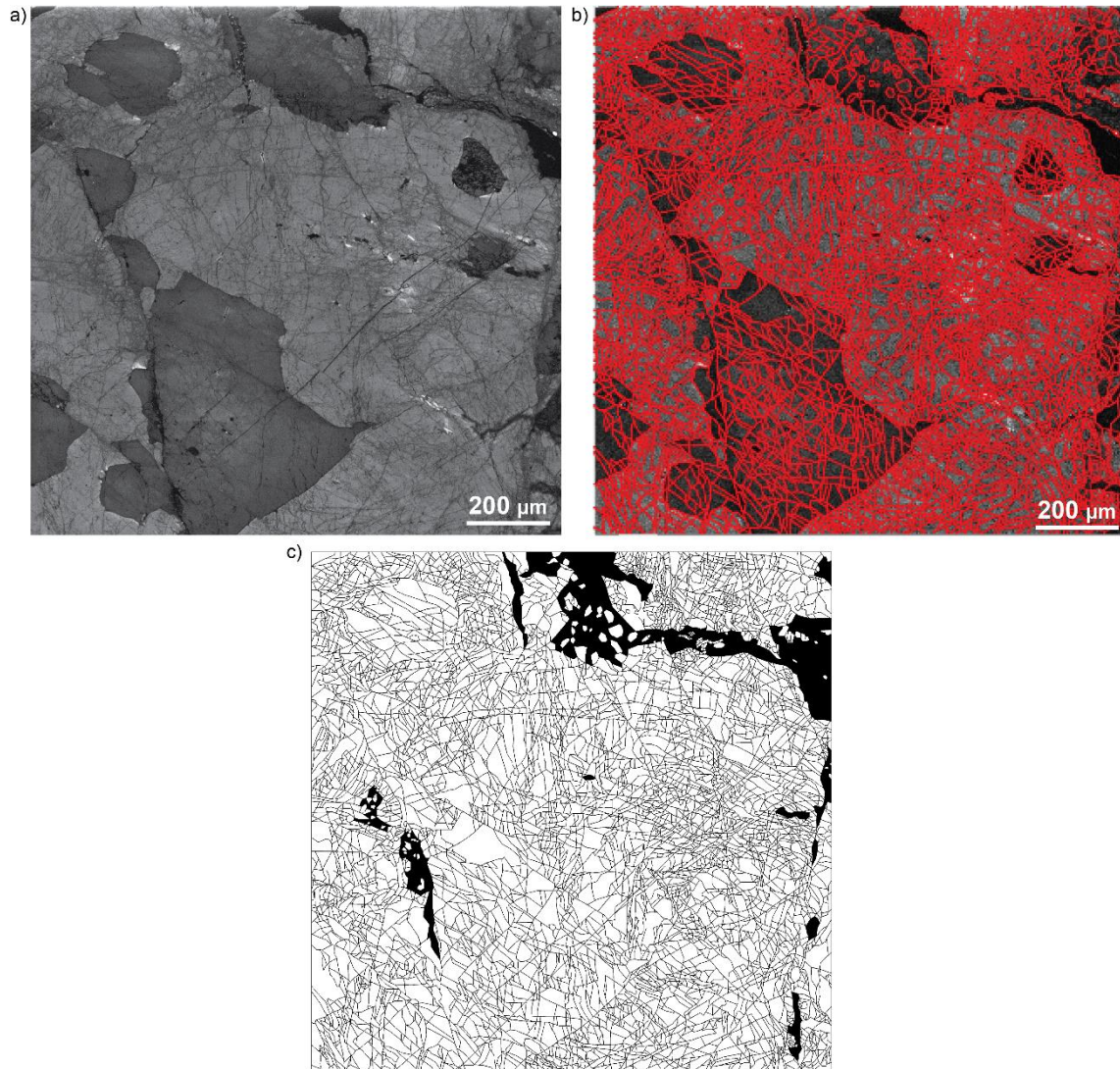**Fig. 3.3** Main steps of CL image elaboration. **a)** Original CL image of the southern side of natural sample L05-08. **b)** Fracture pattern drawn with AutoCAD®. **c)** Resulting pattern elaborated through the MATLAB® script.

3.5.2 Grain boundaries

In the case of natural sample L05-08, the images used to determine the fragment (or clast) size distribution included 1) one FE-SEM-CL image (maximum resolution of ~ 1 μm), plus 2) one EBSD map (max resolution ~ 1 μm) and 3) one high-resolution mid-angle BSE image (max resolution ~ 90 nm), of the same area (see Appendix A). The images were collected at the tip of the major injection vein found in the thin section, because there the damage and fragmentation of the pseudotachylyte host rock is the most intense (Fig. 4.11h). In fact, this area is considered as representative of the maximum intensity of fracture damage, which should correspond to the physical situation which precedes, during seismic faulting,

24

the frictional melting of the grains (Spray, 1995; Hirose & Shimamoto, 2005; Di Toro et al., 2009). The analysis of the selected images allowed me to investigate the grainsize spanning from ~ 0.8 mm to 90 nm, and to build a Clast Size Distribution over 5 orders of magnitude. The images underwent a different elaboration technique and the processing of the EBSD map is described in Chapter 3.6.2.

The boundaries of grains/fragments were first tried to be extracted from the FESEM-CL images with Fiji. Due to the complexity of the CL microimages and the consequent heavy loss of information after the elaboration, I chose to extract the grain boundaries manually, employing one of the microimages elaborated also for the microfractures, instead of the one chosen at the beginning representing the surroundings of the pseudotachylyte injection vein. The new microimage and the pictured damage was considered equal to the one chosen at the beginning, because it also comes from the pseudotachylyte-wall rock boundary of the same thin section (L05-08). The elaboration was done with AutoCAD®, as for the microfractures. The resulting .dwg file was converted to a .tiff image with CorelDRAW® (Fig. 3.4). The mid-angle FESEM-BSE image did not have enough contrast for automatic thresholding through Fiji, so also in this case the grain boundaries were manually drawn one by one with Adobe Illustrator® (Fig. 3.5). For both microimages, the area and perimeter data were successively extracted with Fiji and saved in a .xlsx file for their elaboration. Fiji (Schroeder et al., 2021) is a software package including ImageJ software and various plugins. ImageJ is based on Java language, and can display, edit, analyse and process 8-bit grayscale images. The elaboration of the SEM-EBSD map is described in Chapter 3.6.2.

To produce the Clast Size Distribution diagrams, the fragments areas were organized in an Excel spreadsheet by decreasing value (in μm^2). From these values the diameters of the circles having equal area to every particle were calculated (according to the formula $d = 2\left(\sqrt{A/\pi}\right)$). The Clast Size Distribution curves were generated plotting the diameter of the fragments versus their cumulative number of clasts with a certain diameter in a log-log diagram.

Fig. 3.4 Main steps of CL image elaboration for the grainsize analysis. **a)** Original CL image of the southern side of natural sample L05-08. **b)** Grain perimeters elaborated from the microfracture pattern of Fig. 3.3b. **c)** Resulting grain boundaries elaborated with CorelDRAW® script. The black areas were not considered because the fragments were not well discernible in the FESEM-CL image because too small. The subvertical black line at the top of the image is an injection vein.
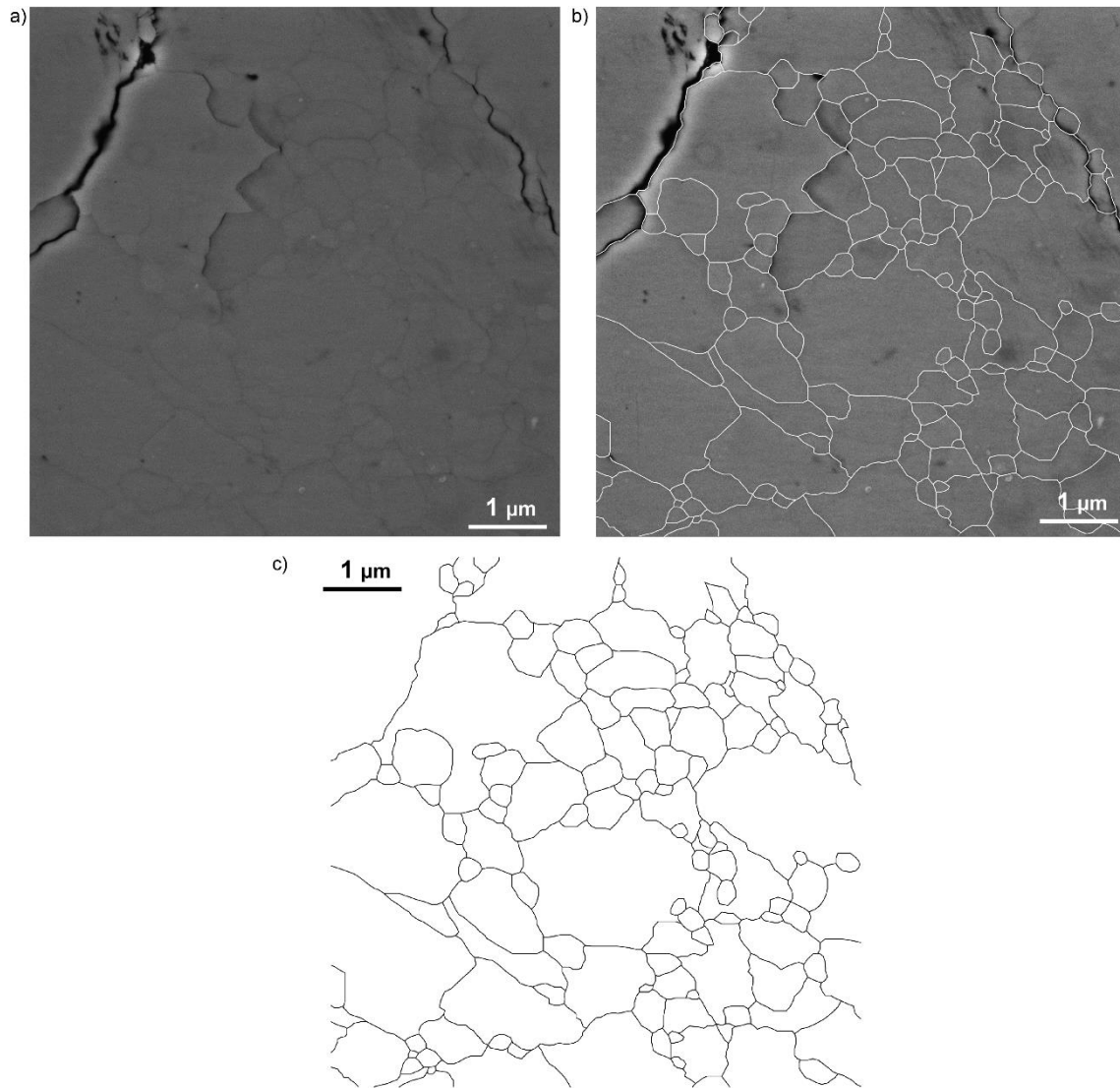
Fig. 3.5 Main steps of FESEM-BSE image elaboration to obtain the grain boundaries for the CSD curves. **a)** Original FESEM-BSE image of the tip of the pseudotachylyte injection vein of natural sample L05-08. **b)** Grain/fragment boundaries drawn with Adobe Illustrator®. **c)** Resulting grain/fragments boundaries for the ImageJ elaboration.

3.6 MATLAB® script

The orientation and density of the segments describing the microfractures were obtained with a specific MATLAB® script, while the perimeter and area of each fragment/clast was retrieved from the EBSD map with the MTEX MATLAB® toolbox. The two methods are described below.

3.6.1 Microfractures

Quantitative analyses of the microfracture patterns of the samples were performed with a MATLAB® script written by Ashley Griffith to generate rose diagrams and histograms of microfracture trends with respect to a given geographical orientation (e.g., north, Griffith et al., 2010). In Griffith et al. (2010) analysed microfractures were those cutting quartz grains and visible at the optical microscope because of the presence of fluid inclusion trails. Thus, the original MATLAB® script was slightly modified to satisfy the objectives of this thesis (see Appendix B). The workflow to obtain the graphic outputs was (Fig. 3.6):

I.   The microfracture pattern of the image was digitalized through AutoCAD®, as described in Chapter 3.5.1. This step allowed me to obtain the microfracture network in a .dxf file;

II.   The .dxf file was converted into a .xyz file with the software Dxf2xyz 2.0. The output file contained an identification number and the x, y coordinates of their starting and ending points of each segment;

III. The .xyz file was fed to the MATLAB® script, that generated the orientation rose diagram, the frequency histogram and an image of the microfractures.

The y axis of the frequency histograms refers to the number of standard 10 µm segments contained in the elaborated SEM-CL microimages. Both the rose diagrams and the histograms are built with reference to the direction of the fault vein, always considered horizontal. The scales of the rose diagrams are not equal to one another to allow a better reading of the ones with less microfractures, while the scales of the histograms are normalized to the microimage with the highest number of segments (>3500).
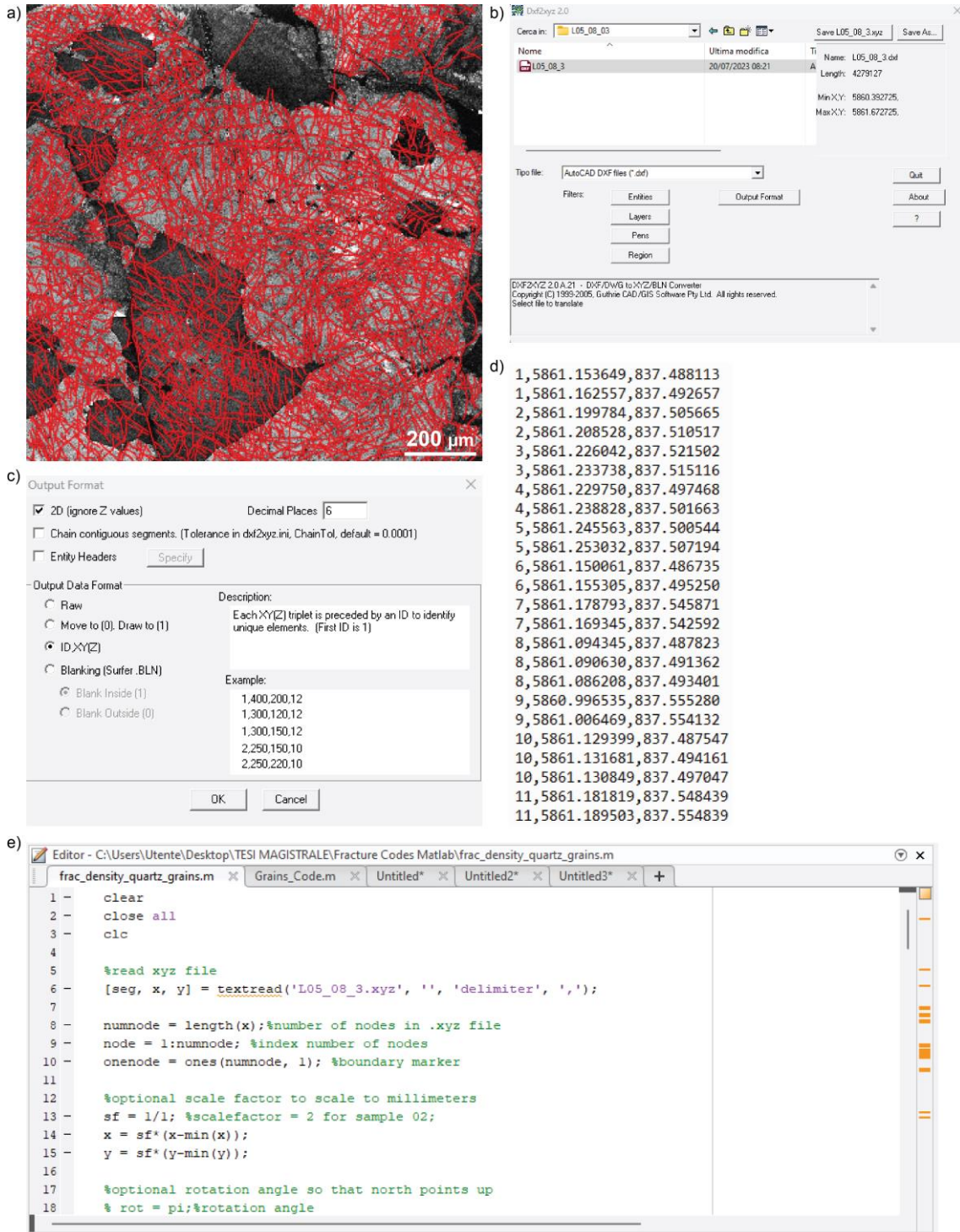
Fig. 3.6 Main steps of the processing of the microfracture pattern. **a)** AutoCAD® dxf. file with the microfractures drawn by hand. **b)** Software Dxf2xyz 2.0 for the conversion of the file. **c)** Settings of the .xyx output file to obtain the coordinates of all the segments. **d)** Example of a .xyz file containing the identification number and x,y coordinates of the starting and ending points of all the segments. **e)** MATLAB® script by Griffith et al. (2010); line 6 reads the .xyz file. Results of the analysis and MATLAB® outputs are reported in Chapter 4.

3.6.2 MTEX

The EBSD map was elaborated fist through AZtecCrystal software by Oxford Instruments, to remove the noise, while the data processing was done with the MATLAB® toolbox MTEX (Bachmann et al., 2011), an open source toolbox for the elaboration of EBSD and crystal pole figures data. The grains were calculated for all the minerals of the EBSD map. Biotite was then removed from the map because not relevant. After a preliminary detection of the grains from the raw EBSD map, a more in-depth cleaning of the data was performed, removing grains defined by less than 4 pixels and setting all the non-indexed pixels as non-measured values. The empty pixels in the grains were then filled by interpolation. The standard degree threshold (10°) for the distinction of two neighbour grains was considered appropriate, even if the deformation mechanism is mostly brittle *in-situ* fracturing, without major rotation of the crystals. This because setting the value too low would mean considering subgrains as single grains. I calculated the grains employing also lower values (respectively 8° and 6°), but the difference with the initial result was not relevant, so the 10° value was maintained. Another issue that had to be considered was crystal twinning. For quartz, the most common twinning law is the Dauphiné law, that consists in a rotation around the axis [0 0 0 1] of 60°. To avoid the contribution of twinning to the grain perimeters calculation, the symmetry system of quartz had to be switched to hexagonal, and the grains recalculated. The twinning laws of K-feldspar and plagioclase are much more complex, so it is difficult to avoid considering twins as different crystals as for quartz. A preliminary analysis of the EBSD map showed the presence of a low number of twins for both plagioclase and K-feldspar, so it was decided to ignore the contribution of twinning in feldspars. After all this steps, the EBSD map still presents some noise, especially in K-feldspar grains. Some of the pixels have been indexed as plagioclase instead of K-feldspar, due to the difficult distinction between the two minerals, and these pixels cannot be removed without altering too heavily the data (Fig. 3.7). However, this was not considered problematic for the calculation of the grainsize.
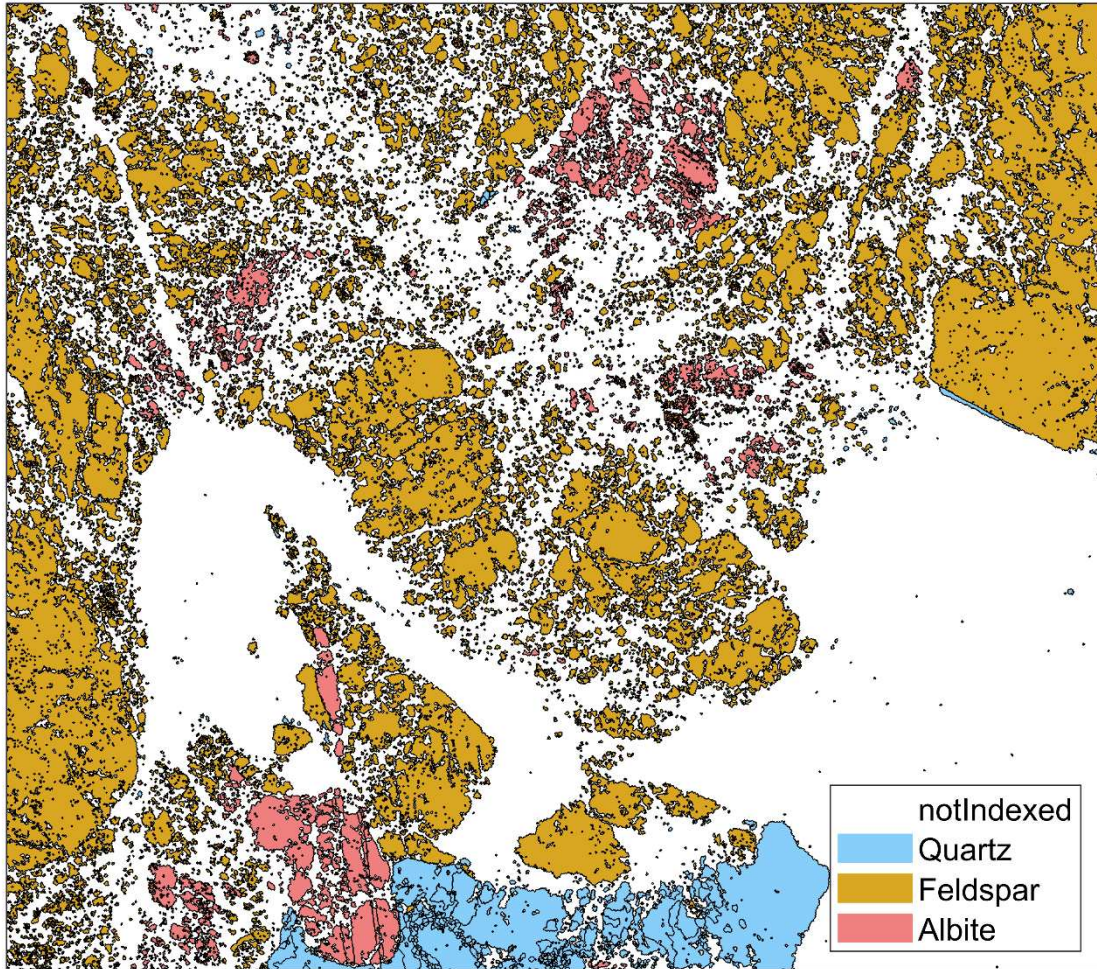
Fig. 3.7 EBSD map after the data cleaning, with the three mineral phases of interest and evidenced grain boundaries. The small dots in K-feldspar are wrongly indexed pixels.

4. Results

In this Chapter the results of the microstructural analysis are presented, both for natural and experimental samples. The main results include the description of the selected fault and of the microstructures in the pseudotachylytes and wall rocks. The quantitative analysis of the microfracture patterns (i.e., fracture density and orientation) and of the fragments (Clast Size Distributions) with increasing distance from the pseudotachylyte fault vein are also presented.

4.1 The selected pseudotachylyte-bearing fault

The selected fault segment (Fig. 4.1) was studied by Griffith et al. (2010), Lazari et al. (2023) and in my Bachelor's degree thesis. The fault is located in the upper Genova Valley (N46 10' 348", E10 34' 864"), at the base of the Lobbia glacier (Fig. 2.1). The area has been exposed only recently due to glacial retreat and the action of the ice allowed the formation of very well-polished outcrops on relatively flat surfaces. The fault cuts the hornblende-free (i.e., biotite is the main mafic mineral) tonalites of the Avio pluton (Di Toro & Pennacchioni, 2004). The selected fault has a right-lateral sense of shear and, like most E-W striking features of the GLFZ, dips 60° towards N205 (Di Toro & Pennacchioni, 2005). In particular, this fault segment was selected because the intersection of the fault surface with the outcrop surface is sub-parallel to the fault slip vector. In fact, the fault presents large-wavelength (~ 1 m) bends that result, given the right sense of shear, in local contractional, neutral and extensional jogs or domains (Griffith et al., 2010; Lazari et al., 2023) (Fig. 4.2). Samples L05-08, WF22-01a, b and c come from a neutral domain of the fault. The fault is exposed for ~ 5 m in length, because is truncated at both ends by other faults. In fact, though the GLFZ is ~ 20 km long, given its anastomosing structure the length of individual fault strands recognizable in the field is in the range of few to hundreds of metres (Di Toro & Pennacchioni, 2005; Griffith et al., 2010). Structural markers (dykes, enclaves etc.) offset by the fault are missing (Griffith et al., 2010). To estimate the fault slip displacement, two methods have been employed (Di Toro et al., 2005b; Di Toro & Pennacchioni, 2005; Griffith et al., 2010): (1) a statistical approach based on the faults in this field area, where for a number of fault segments the displacement was measured in the field and plotted against the pseudotachylyte fault thickness (calculated as the ratio between the pseudotachylyte vein area and the total length of the fault), and (2) the length of the dilational jog found at around 3.3

m from the left on the fault in the latter (30 cm, Fig 4.2). The estimated slip accommodated by the fault ranges between 30-100 cm (see also Chapter 5.1).
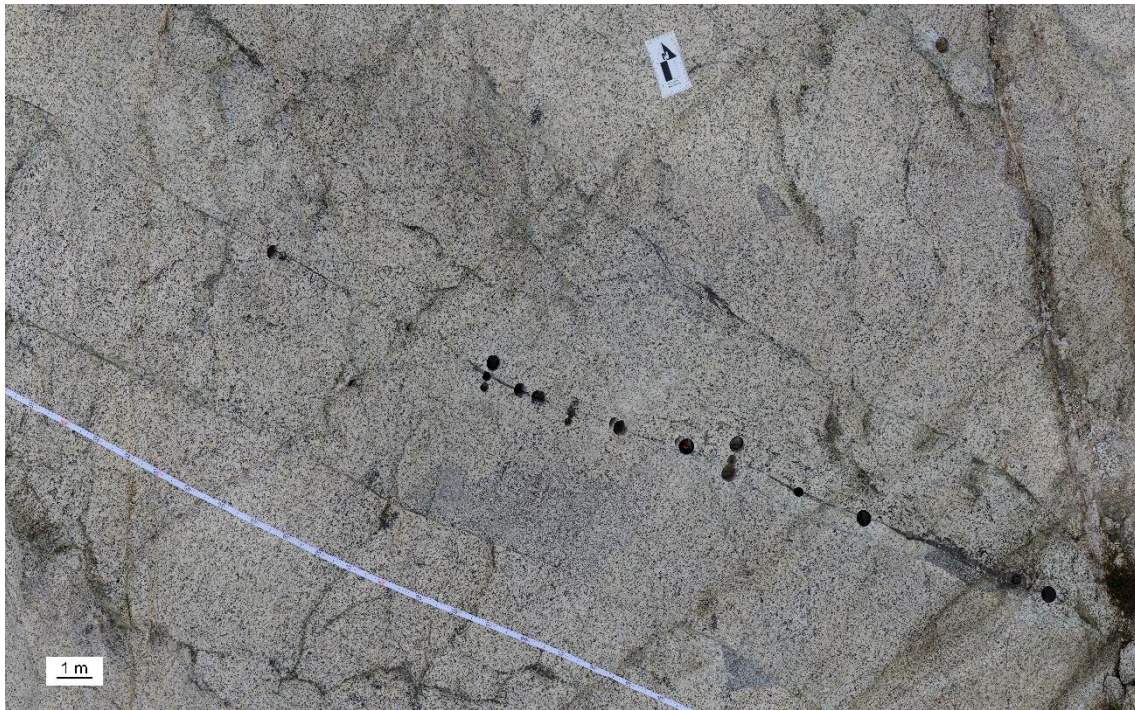
Fig. 4.1 The selected fault. UAV or drone image collected during the field survey of my Bachelor's degree in September 2020. The dark colour of the pseudotachylyte-bearing faults, mostly striking from top left to bottom right, is well discernible from the whitish host tonalites. Fault location is reported in Fig. 2.1. Arrow points to the north.
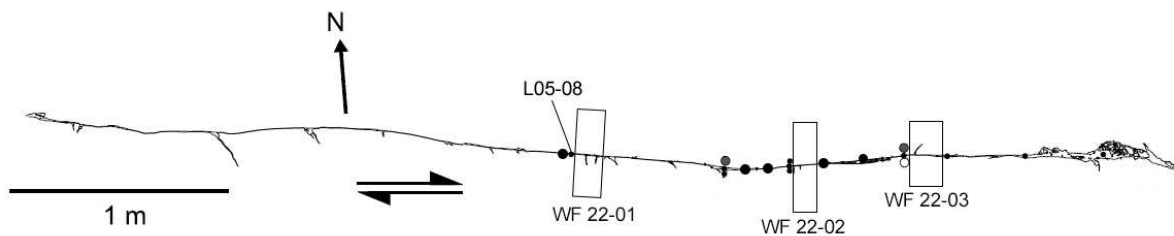
Fig. 4.2 Drawing of the selected fault segment obtained from photomosaics with location of the samples. The black dots represent the locations of drill samples collected by Griffith et al. (2010). Instead, the rectangles are the rock slabs collected for this thesis. L05-08 is the sample collected by Griffith et al. (2010) and discussed also in the present thesis. Modified from Griffith et al. (2010).

In the selected fault, pseudotachylyte is present both as fault and injection veins, and decorates all the fault surface, including a 50 mm-thick extensional melt reservoir located at the eastern end of the fault exposure (Fig. 4.1). Under the optical microscope, the inner structure of the pseudotachylyte is quite homogeneous and there are no evidences of multiple events of pseudotachylyte formation. This, together with the pristine aspect of the host rock

and the absence of greenschist facies cataclastic precursor, support the assumption that the fault records a single seismic slip event (Pittarello et al., 2008; Griffith et al., 2010). Pseudotachylyte injection veins intrude the wall rocks at high angles with respect to the fault vein and are found preferentially in the southern wall rock (Fig 4.2, 4.7a). This asymmetric distribution of the pseudotachylyte injection veins is in accordance with the stress field perturbation associated with rupture propagation from the west to the east in right-lateral strike slip faults (see discussion in Di Toro et al., 2005). In fact, only very few veins intrude the northern side (Fig. 4.2, sample WF22-03). The average pseudotachylyte thickness (area of the pseudotachylyte, including the injection veins, divided by the length of the exposed fault) is 7 mm, with thicknesses of $\sim 100 - 200$ µm in contractional domains, and of 2 mm in extensional domains. The outcrop of the fault selected for sampling does not show any other major fractures or damage, and there are no evident relationships with the other faults in the surrounding. Thus, the microfracture pattern analysed in this study can be considered as related only to the selected fault.

The present fault segment has been chosen because (1) of its simple meso-scale structure, (2) the absence of any precursor deformation event, (3) the possibility to estimate the (probably cosesimic) offset (~ 30 cm) and (4) the outcrop surface is orthogonal to the fault dip and sub-parallel to the fault slip vector (Griffith et al., 2010). Furthermore, samples from the fault were already available at the Department of Geosciences; in particular, sample L05-08 was also object of my Bachelor's degree thesis.

A high resolution photograph of the polished sample WF22-01, the scans of all the thin sections (both natural and experimental) with the location of the SEM-CL microimages and the SEM-CL microimags employed for the microfracture pattern quantitative analysis are reported below (Fig. 4.3, 4.4 and 4.5).

Fig. 4.3 High resolution photograph of the polished sample WF22-01. Red arrows indicate the fracture sets visible also in optical microscope micrographs of thin sections WF22-01a, b, c, to the right of a mesoscopic injection vein. (Fig. 4.9a, 4.10a).
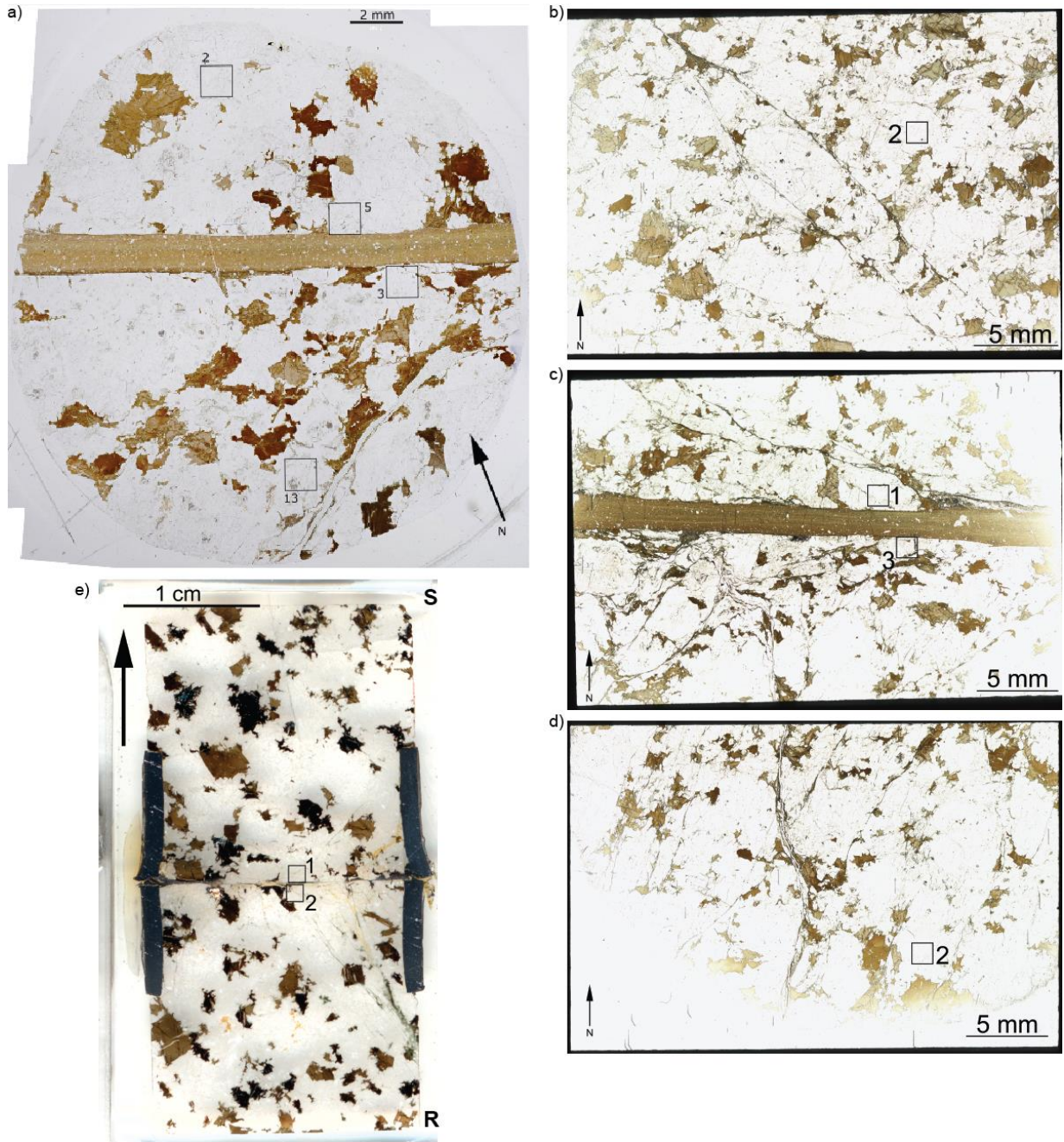
Fig. 4.4 Scans of the natural and experimental thin sections of this thesis, with the location of the FESEM-CL microimages employed in the microfracture pattern characterization (see Fig. 4.5 for the microimages). A4 scans are available in Appendix A. **a)** Sample L05-08. **b)** Sample WF22-01a. **c)** Sample WF22-01b. **d)** Sample WF22-01c. **e)** Sample HVR376; R = rotary, S = stationary. The numbers in the thin sections refer to the names of the FESEM-CL microimages (see Table 3.1).
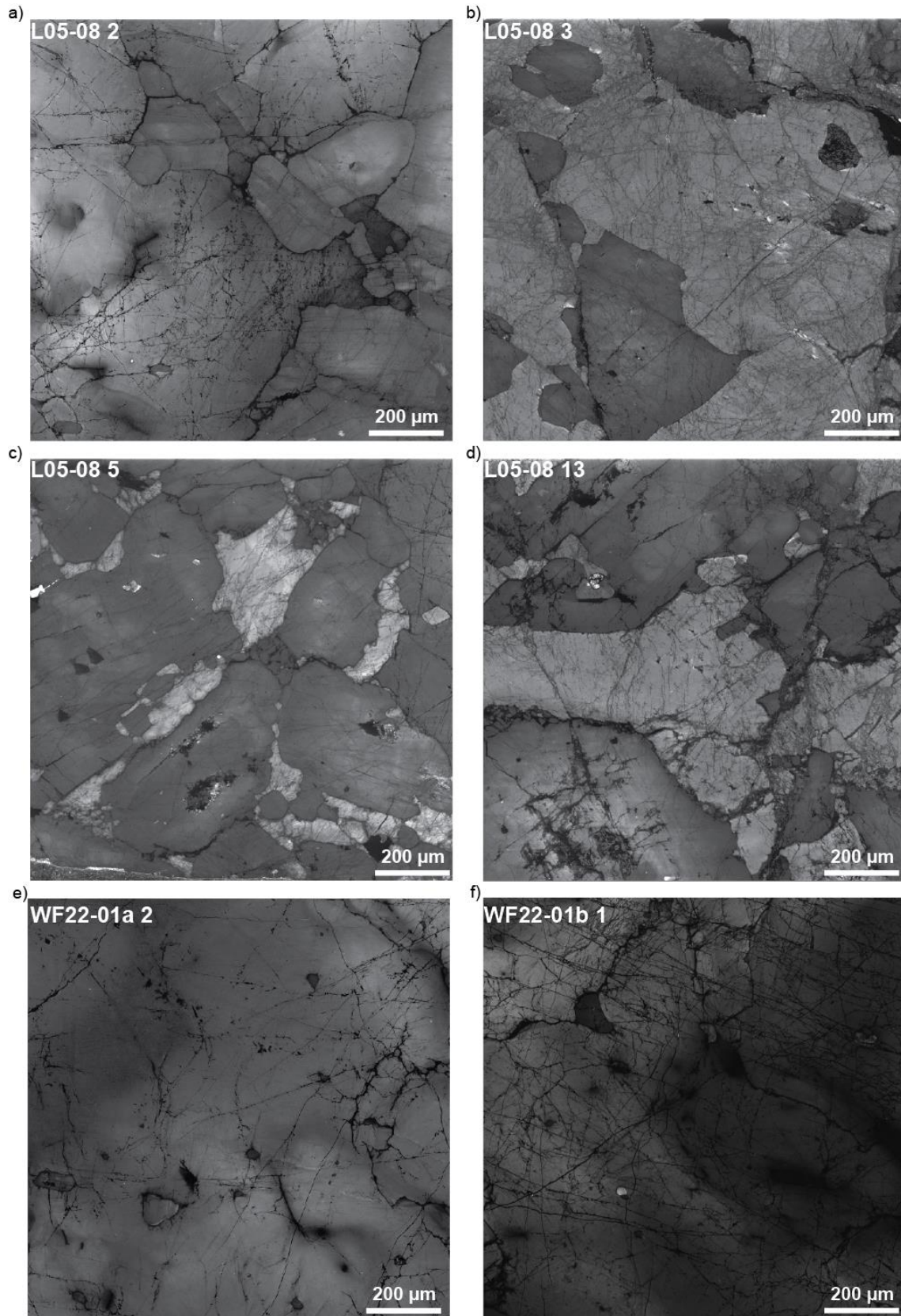
Fig. 4.5 Caption in the next page.
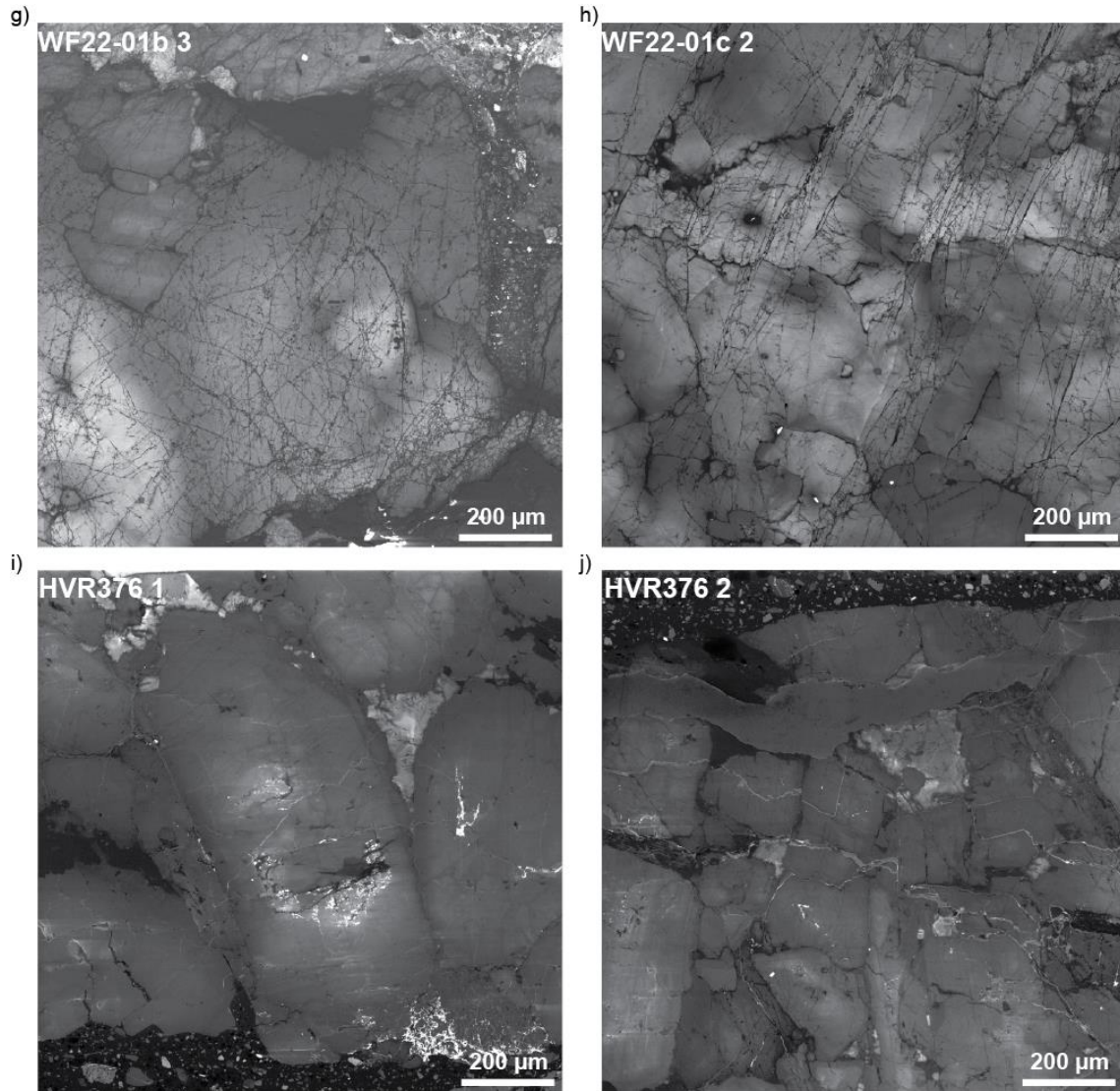
Fig. 4.5 FESEM-CL microimages of the northern and southern wall rocks of natural and experimental samples for the microfracture pattern characterization. For the location of the microimages in the thin sections refer to Fig. 4.4. **a)** HVR376 1. **b)** HVR376 2. **c)** L05-08 2. **d)** L05-08 3. **e)** L05-08 5. **f)** L05-08 13. **g)** WF22-01a 2. **h)** WF22-01b 1. **i)** WF22-01b 3. **j)** WF22-01c 2.

4.2 Microstructures in natural pseudotachylytes

The analysed natural samples are L05-08, WF22-01a, WF22-01b, WF22-01c. The magmatic mineral assemblage of the Avio tonalites is composed by plagioclase (48 % modal composition) quartz (29 %), biotite (17 %) and K-feldspar (6 %) with an average grainsize of 2 mm. Accessory minerals include zircon and rutile. Post-magmatic alteration minerals are epidote and chlorite (Di Toro & Pennacchioni, 2004, 2005). Analysis of the thin sections with optical microscope shows that the tonalite is not altered nor deformed except by brittle fracturing, and has a magmatic texture. At the contact (< 10 mm) with the pseudotachylyte

fault vein, quartz grains have undulated and sometimes patchy extinction at crossed Nicols, and are often made by subgrains (Fig. 4.11). Instead, feldspars have more homogeneous extinction at crossed Nicols. Plagioclase shows zoning and evidences of alteration where it exhibits a dusty appearance, likely saussurite (Fig. 4.6e). Deformation twinning is occasionally present. Biotite, locally altered to chlorite, is deformed more plastically than the other minerals and is kinked, sometimes very strongly (Fig. 4.6 a, b). Quartz grains have linear trails of fluid inclusions, evidence of healed microfractures (Fig. 4.6 d, 4.9b, 4.10b).

In FESEM-CL images, the minerals appear with different shades of grey, which, in general, are not correlated with mineralogy, so they should not be compared from one image to another to recognize the mineral phase. This is because the greyscale depends on compositional changes (ppm) and also because in the case of some microimages the brightness and contrast was changed because they were very dark when acquired. However, healed and sealed microfractures and compositional changes, zoning etc. are evidenced. In FESEM-CL images, quartz grains often display darker rims and shadows, likely due to changes in Ti content (probably in the range of 30 to 100 ppm, Bestmann et al., 2016), while feldspars can have different grey shades due to compositional zoning (Fig. 4.9c). Biotite is very dark due to its composition (i.e. it contains elements, like Fe, with a higher atomic number with respect to the other minerals).

Both thin sections L05-08 and WF22-01b contain a ~ 1.5 mm-thick pseudotachylyte fault vein (Fig. 4.7a). About ~ 0.2 – 12 mm long (micro-) injection veins intrude the southern wall rock (Fig. 4.7a), consistently with the distribution of larger injection veins at the outcrop scale (Fig. 4.2). No pseudotachylyte (micro-) injection veins intruding the northern wall rocks are present in any of the studied natural samples. Under the optical microscope, the fault vein has dark chilled margins on both sides and presents flow structures in the inner portion (Fig. 4.7a, b, c). Flow structures are visible also in the bigger injection veins. In the fault vein, the colour of the pseudotachylyte is not homogeneous and varies from a dark brown near the borders to light brown in the middle (Fig. 4.7a, c). This change in colour is likely due to the different composition (i.e. abundance of Fe) of the original frictional melt resulting from the preferential melting of biotite along the wall rocks (Di Toro & Pennacchioni, 2004; Lazari et al., 2023). The pseudotachylyte is composed by a glassy-like matrix, containing under the FESEM, microlites formed during the cooling of the melt (Fig. 4.7f). The matrix wraps clasts of quartz and feldspars with rounded borders (Fig. 4.7c, d). As previously stated, there are no evidences of multiple melt generation events in the pseudota chylyte. Both fault and inje-
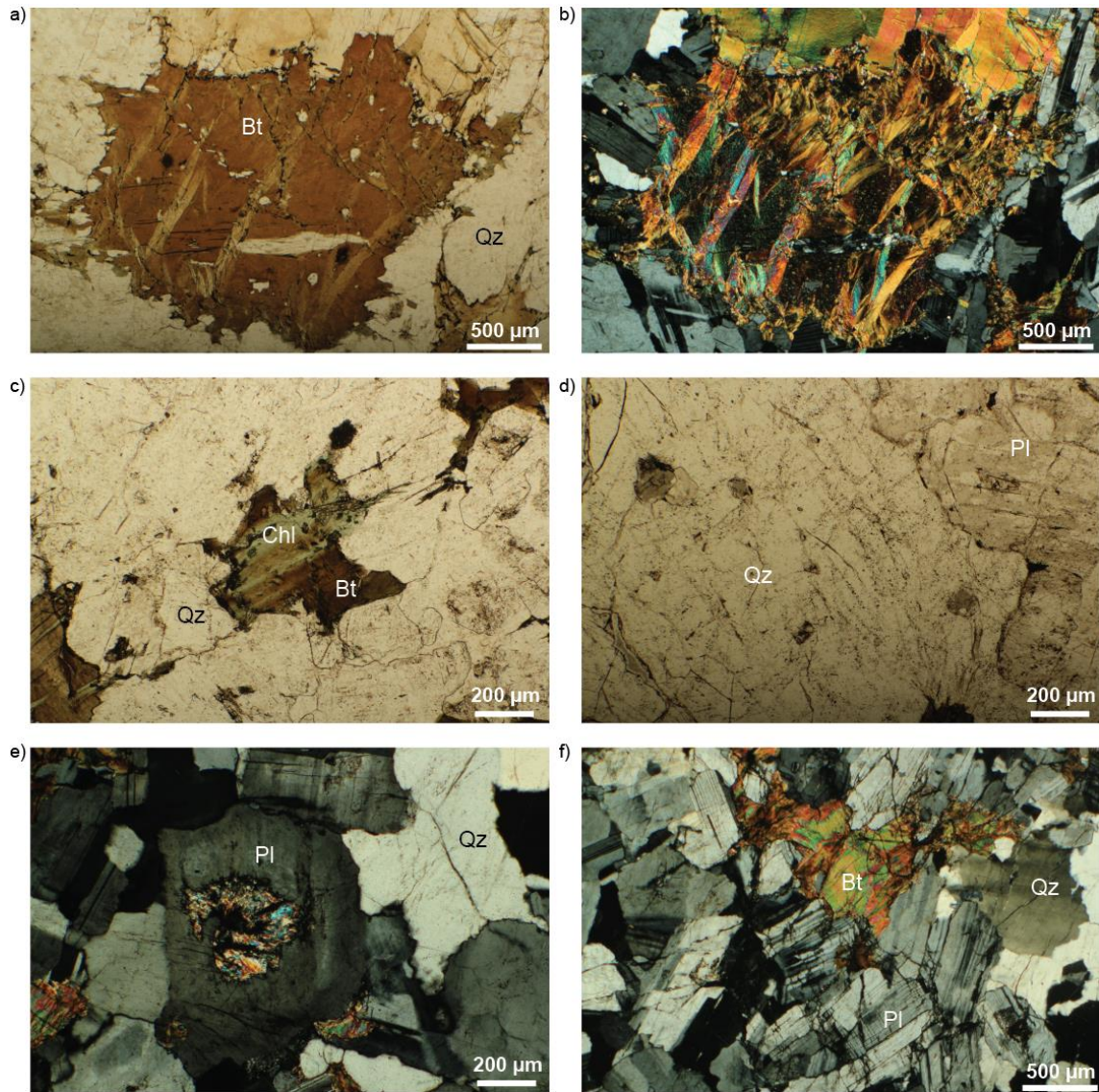
Fig. 4.6 Mineral assemblages and microstructures of the unaltered wall rocks of the natural pseudotachylyte. **a)**, **b)** micrograph of a strongly kinked biotite in thin section WF22-01a, ~ 15 mm from pseudotachylyte fault vein. **c)** Biotite crystal altering to chlorite in thin section L05-08, ~ 5 mm from pseudotachylyte fault vein. **d)** Fluid inclusion trails in a quartz grain, thin section WF22-01a ~25 mm from pseudotachylyte fault vein. **e)** Plagioclase altering to saussurite, ~ 20 mm from pseudotachylyte injection vein, in thin section WF22-01c. **f)** Mineral assemblage of the Avio tonalite, ~ 20 mm from pseudotachylyte injection vein, thin section WF22-01c. a), c), d) optical microscope, parallel Nicols; b), e), f) optical images, crossed Nicols. Bt = biotite, Chl = chlorite, iv = injection vein, KFeld = K-feldspar, Pl = plagioclase, Qz = quartz.
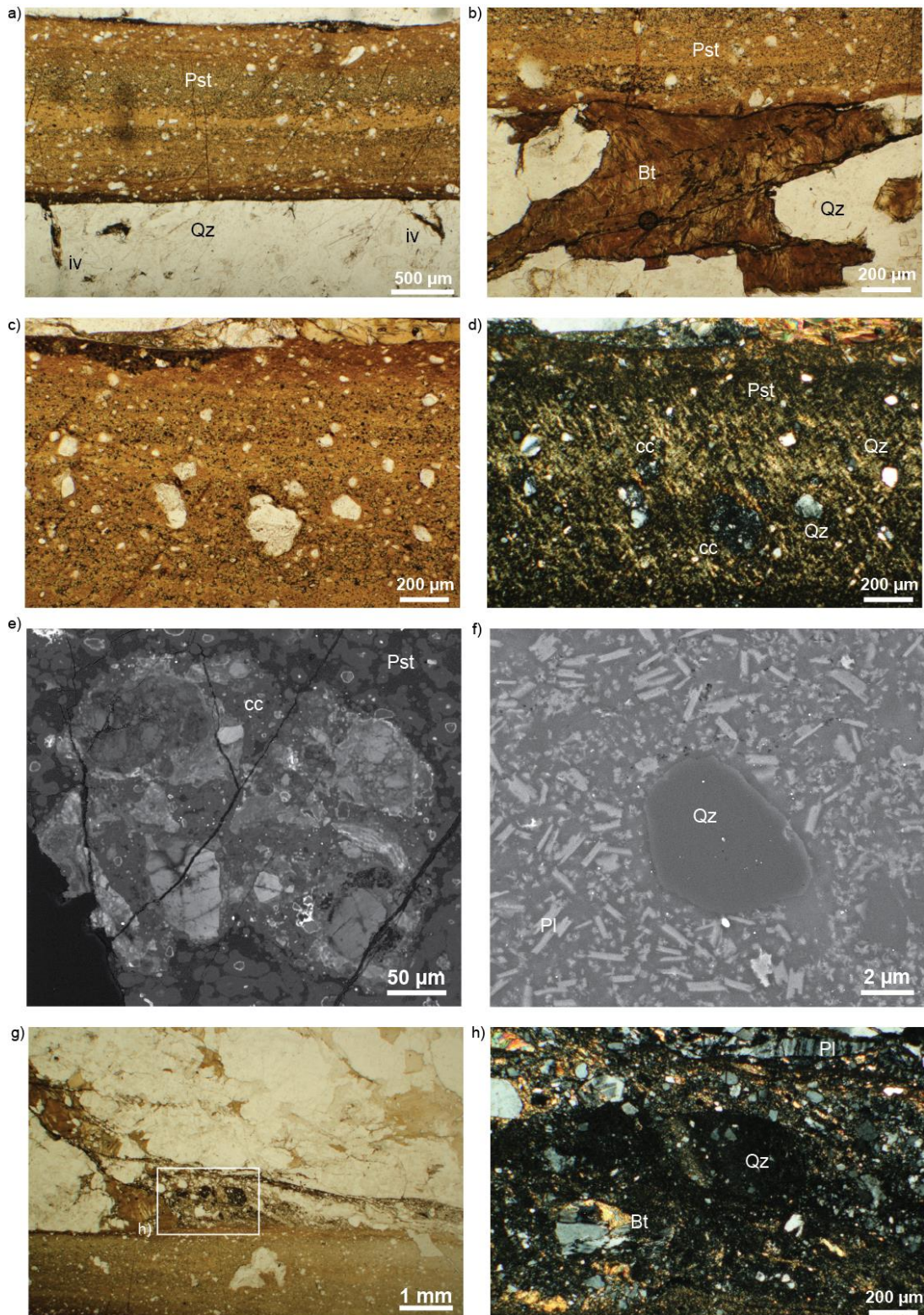
Fig. 4.7 Structure pf the pseudotachylyte fault and injection veins. **a)** Fault vein of sample L05-08, showing chilled margins and a lighter color at the centre; flow structures are also visible. Two injection veins are present in the southern wall rock. **b)** Embayment of a biotite crystal along the pseudotachylyte fault vein of thin section L05-08. **c)**, **d)** Survivor clasts in the pseudotachylyte fault vein; these are quartz and clasts of highly comminuted material (= cc.). Thin section WF22-01b. **e)** Clast of highly comminuted material in the pseudotachylyte, thin section L05-08. **f)** Quartz survivor clast surrounded by microlites of plagioclase, nucleated from the crystallizing melt. Thin section L05-08. **g)** Mixed clasts and melt domain in the northern wall rock of sample WF22-01b. **h)** Zoom of the inner structure of the mixed domain. a), b), c), g) Optical microscope images, parallel Nicols; d), h) optical microscope images, crossed Nicols; e) FESEM-CL microimage, and f) FESEM-BSE microimage.

ction veins have sharp boundaries with the wall rock, with the exception of embayments in correspondence of biotite grains (Fig. 4.7b). These embayments are due to the lower melting point temperature of biotite (ca. 700°C) with respect to quartz (1730°C) and feldspars (1050-1200°C) (Spray, 2010).

Locally, at the pseudotachylyte fault vein-wall rock contact, a ~ 0.1 mm thick layer of highly comminuted wall rock material mixed with solidified frictional melt is visible (Fig. 4.7c, d), and fragments of the same material are found in the pseudotachylyte (Fig. 4.7d, e). In the northern side of sample WF22-01b where a pervasive microfracture system trending WNW-ESE comes into contact with the pseudotachylyte, a domain formed by ultrafine fragments of the wall rock tonalite welded by solidified frictional melt is visible (see also Fig. 3 in Lazari et al., 2023) (Fig. 4.7g, h).

4.2.1 Microfractures in natural pseudotachylytes

Samples L05-08 and WF22-01 are stem from a planar section of the fault that is assumed as a neutral domain, so that the microfractures observed should be less influenced by the bends of the fault and derived stress concentration (Fig 4.2). Sample L05-08 does not show any macroscopic fracture, while two major fracture sets are visible in the southern wall rock and one in the northern wall rock of the polished sample WF22-01 (Fig. 4.3, red arrows). The fracture set in the southern side of sample WF22-01 runs N-S and it is connected to the damage surrounding the 3 cm long mesoscopic injection vein (Fig. 4.3). Instead, the second set, in the northern side, strikes WNW-ESE and joins the pseudotachylyte fault vein in the right end of thin section WF22-01b (see also thin section scans in Appendix A). Under the optical microscope is possible to detect only the bigger and longer fractures and microfractures, including those outlined by fluid inclusions (see Griffith et al., 2010). Other than these, minerals in the wall rock seem intact and no other evidence of the real damage is visible. Similarly, FESEM-SE and FESEM-BSE imaging of the thin sections show little of the real microfracture pattern. Instead, FESEM-CL microimaging are able to detect by far more microfractures, as can be appreciated by comparing the microimages of the same area in sample WF22-01 collected with the optical microscope (Fig. 4.8a, b), the FESEM-BSE (Fig. 4.8c) and the FESEM-CL (Fig. 4.8d).

Microfractures are mostly intragranular in the natural samples (Fig. 4.9, 4.10). FESEM-CL images evidence that minerals are pervasively affected by the microfractures, with feld-
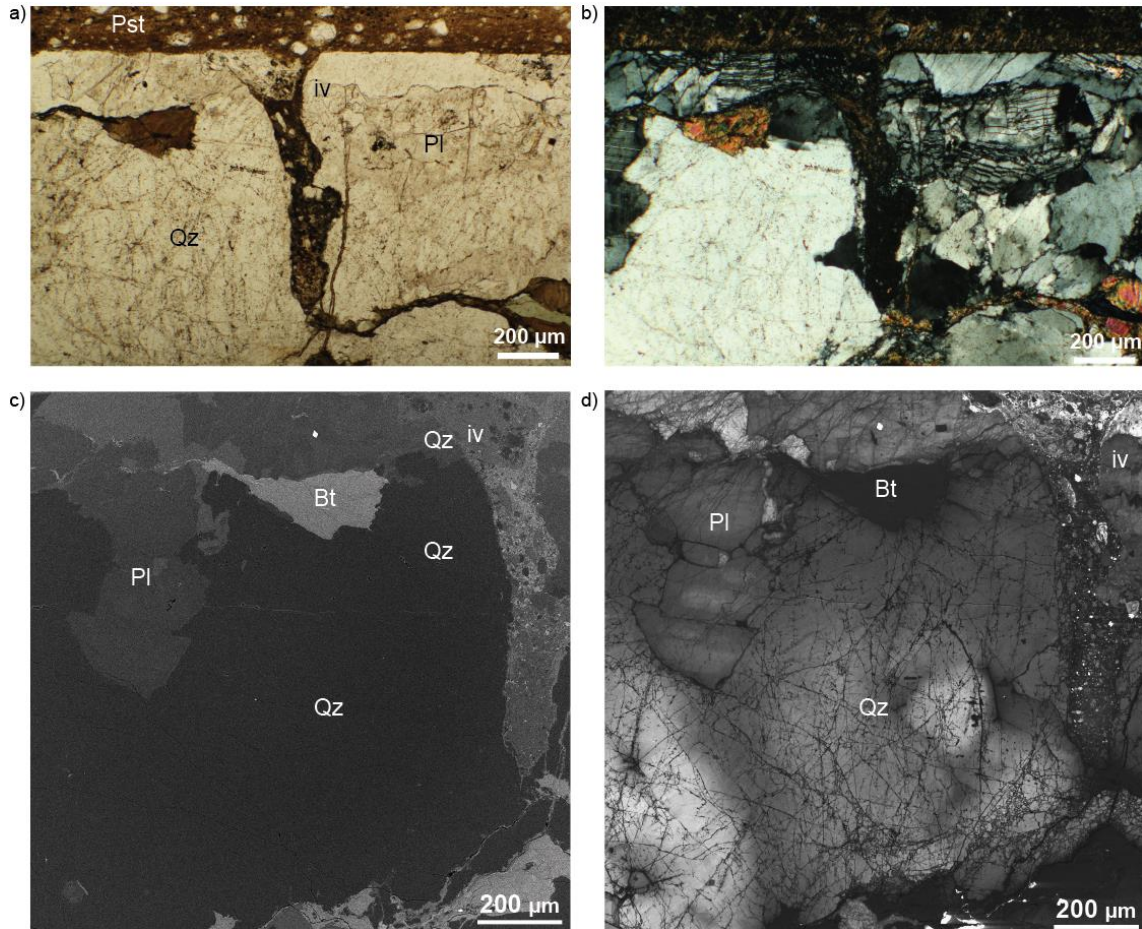
Fig. 4.8 Differences between the microfracture pattern imaged through the analytical techniques employed in this work. All the micrographs represent an injection vein in the southern side of sample WF22-01b. **a)**, **b)** Optical microscope image, parallel and crossed Nicols. **c)** FESEM-BSE microimage. **d)** FESEM-CL microimage.

spars sometimes preferentially fractured along cleavage planes (Fig. 4.9c). Quartz appears to be more fractured with respect to plagioclase and K-feldspar, which contrasts with the observations made by Pittarello et al. (2008), which used only FESEM-BSE (see their Fig. 3). The microfractures evidenced by FESEM-CL are not decorated by fluid inclusions. Microfractures sometimes are clustered at the contact between biotite and quartz or feldspar grains (Fig. 4.10c). In fact, the formation and density of microfractures is favoured by touching minerals with different elastic and fracture toughness (Passchier & Trouw, 2005). The microfracture pattern is extremely complex, especially near the fault and injection veins, but the shape of the individual microfractures is quite planar. The microfracture pattern in the analysed samples is very heterogeneous, with areas, often < 1 mm^2, with few microfractures located at < 1 mm from areas with a pervasive microfracture network (Fig. 4.10c, d). In particular, the wall rock minerals are extremely more damaged in the area surrounding the pseudotachylyte fault and at the tip of the injection veins (Fig. 4.8).
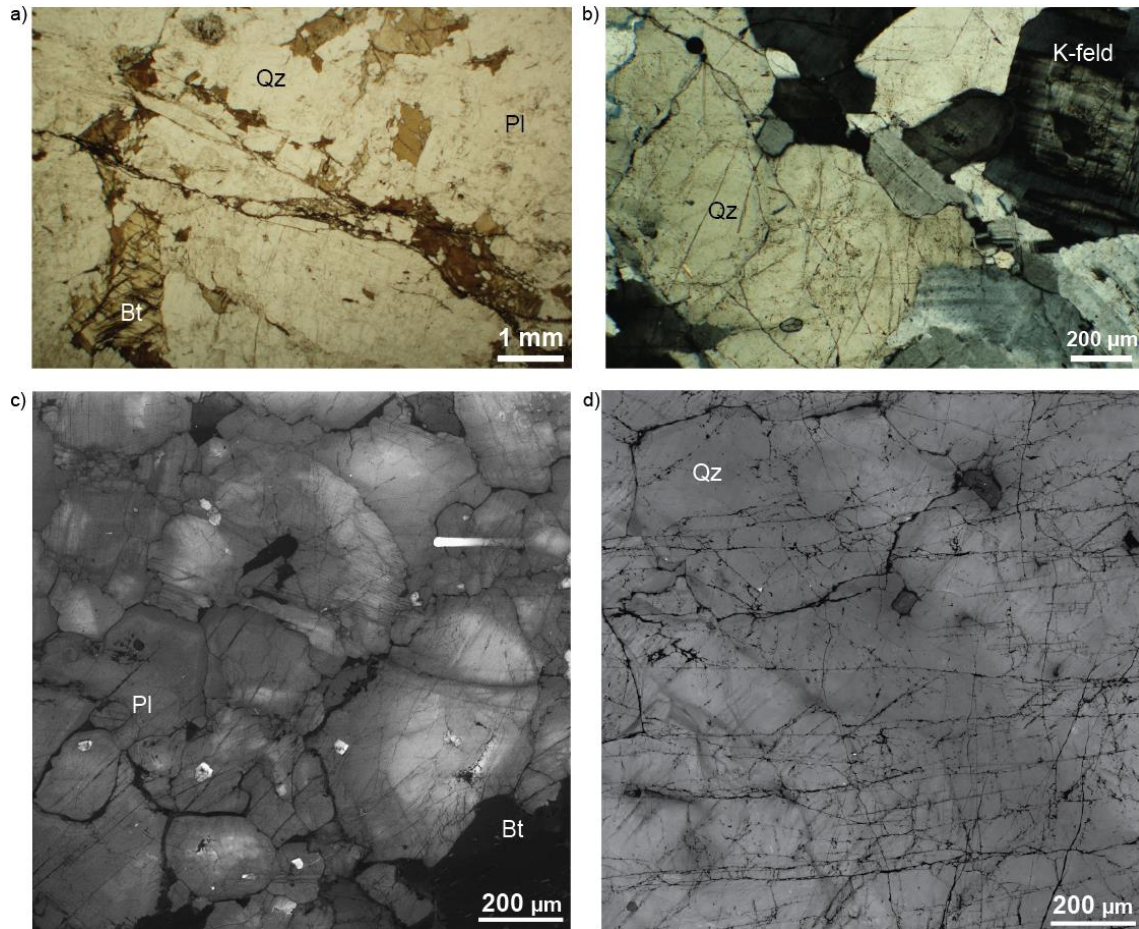
Fig. 4.9 Microfracture pattern characteristics of the northern wall rocks. **a)** Pervasive fracture system in the northern side of thin section WF22-01b, trending WNW-ESE. **b)** Microfractures healed and sealed by fluid inclusion trails at ~ 5 mm from the fault vein, thin section L05-08. A preferential sub-vertical trend is already appreciable. **c)** Microfracture pattern in thin section L05-08 at ~ 2 mm from the pseudotachylyte fault vein. The preferential fracturing of feldspars along cleavage planes is visible. **d)** Microfracture pattern in thin section WF22-01a, with a clear horizontal strike. ~ 12 mm from the pseudotachylyte fault vein. a) Optical microscope image, parallel Nicols; b) optical microscope image, crossed Nicols; c), d) SEM-CL microimages.

Microfracture density broadly decreases moving away from the fault vein (Fig. 4.10c, d, e). Microfractures in general are healed, do not show any opening and are often microscopic brittle faults, accommodating offsets of few micrometres (Fig. 4.10d, f); horsetail splays, conjugated microfaults sets, etc. are common (Fig. 4.10d).

The different distribution, orientation and density of the microfractures in the southern with respect to the northern wall rock, roughly appreciable in the optical microscope images, becomes evident in the FESEM-CL microimages (Fig. 4.9 vs. 4.10). The southern wall rock of the pseudotachylyte-bearing fault appears more damaged, while the northern wall rocks are less damaged, also at the contact with the pseudotachylyte vein. In the northern wall rock of the fault, fluid inclusions trails heal fractures trending E-W to
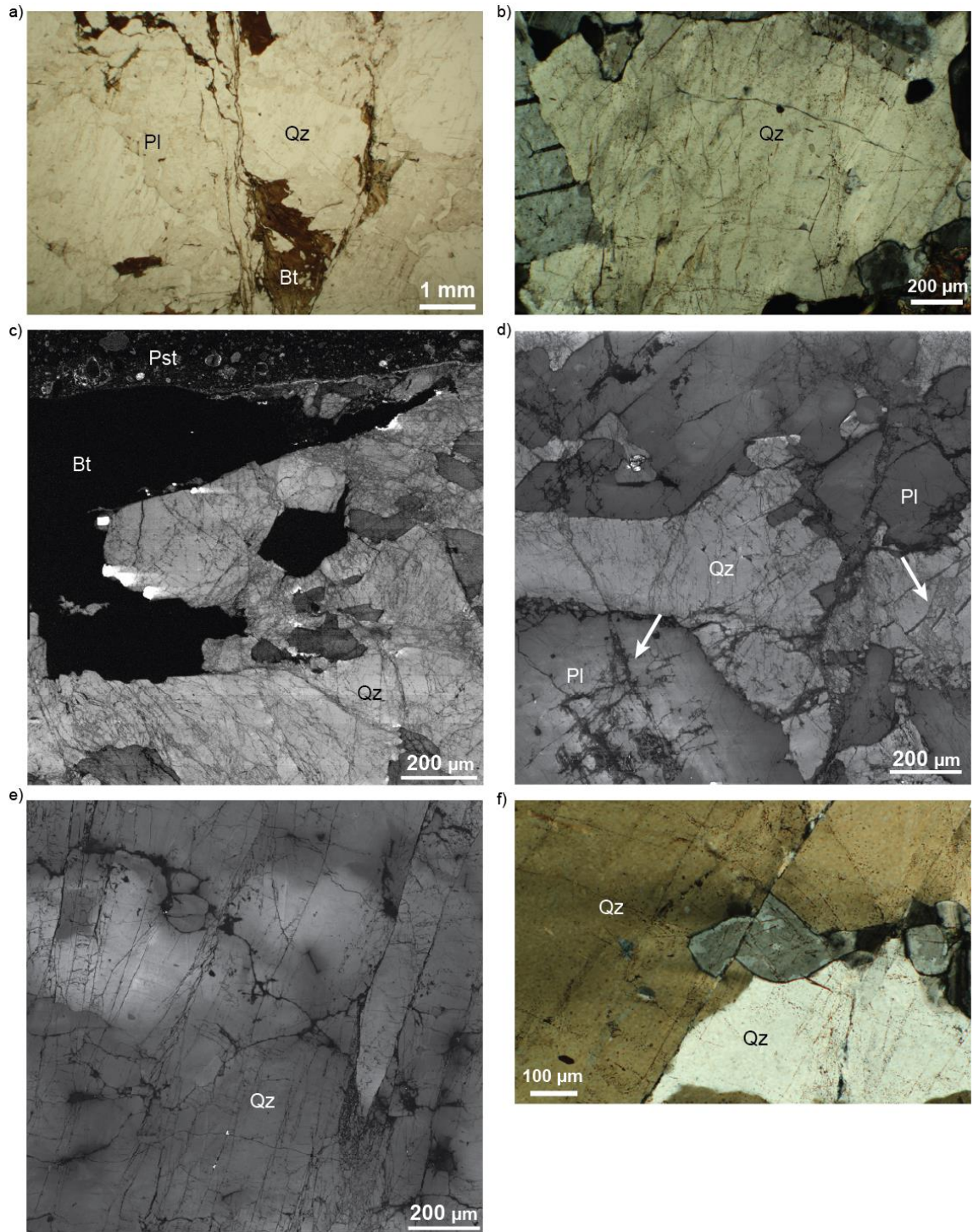
Fig. 4.10 Caption in the next page.

Fig. 4.10 Microfracture pattern characteristics of the southern wall rocks. **a)** Pervasive macroscopic fracture pattern cutting the southern wall rock of sample WF22-01b, with a vertical trend. **b)** Fluid inclusion trails in a quartz grain in thin section WF22-01c, at ~ 20 mm from the pseudotachylyte fault vein. **c)** Concentration of microfractures at the border between biotite and quartz grains in sample L05-08. The microfracture distribution is very heterogeneous, with areas with very high density near to zones much less affected. **d)** Feldspar grains show less damaging than quartz grains. Microfractures behave as microscopic faults: horsetail splay structure, conjugated sets, offset along fractures (white arrows). Thin section L05-08, at 7 mm from the fault vein. **e)** Microfractures in thin section WF22-01, displaying a clear sub-vertical trend (~ 20 mm from the fault vein). The decrease in microfracture density from the areas near the fault vein is appreciable (cfr. with c). **f)** Quartz grain offset by a microfault (thin section WF22-01c, ~ 15 mm from the fault vein). a) Optical microscope image, parallel Nicols; b), f) optical microscope image, crossed Nicols; c), d), e) SEM-CL microimages.

WNW-ESE. Instead, the southern wall rock is cut by a dense microfracture pattern, generally trending N-S to NNE- SSW (Fig. 4.9b, c, d vs 4.10b, c, d, e). Moving away from the fault surface towards both north and south, the number of microfractures per unit area broadly decreases (samples WF22-01a and c, Fig. 4.9d, 4.10e). A late stage set of open sub-vertical fractures cuts the pseudotachylyte vein and both wall rocks, so these fractures are related to a late deformation event and not relevant for the present work. A quantitative characterization of the microfracture pattern of FESEM-CL imaging is reported in Chapter 4.4.2.

The microfracture pattern is locally so intense that defines micro-domains made by ultrafine (< 1 μm in size, so below the resolution of the FESEM-CL technique) fragments of the wall rock (Fig. 4.11). These domains are located (1) along the bigger fractures cutting the wall rock, as those found in the southern wall rock of sample L05-08 and in both wall rocks of sample WF22-01 (Fig. 4.11b, c, d), (2) at the pseudotachylyte fault vein-wall rock contact (Fig. 4.11a), and (3) and at the tip of the injection veins (Fig. 4.11h). The micro-domains, poorly visible under the optical microscope, are evident in FESEM-CL and especially in mid-angle FESEM-BSE microimaging. In fact, the resolution of FESEM-CL imaging is not enough to resolve the finest portion (<< 0.09 μm) of the fragments of the micro-domains, so FESEM-EBSD (resolution < 1 μm) and mid angle FESEM-BSE (resolution < 100 nm) were employed. In particular, the mid angle FESEM-BSE microimaging resolves the ultrafine and non-indexed fragments in the area of the EBSD maps (see Fig. 4.11i and 4.15). The FESEM- CL, FESEM-EBSD and mid angle FESEM-BSE analyses were carried out at the tip of the injection vein in sample L05-08 (Fig. 4.11h). This particular area was selected because the damage in this area is the most intense, and can

represent the extreme fracturing of the wall rock prior to the propagation of the pseudotachylyte fault and injection veins.

The micro-domains are made by randomly oriented fragments of quartz, feldspar and biotite (Fig. 4.11). In the micro-domain at the tip of the injection vein in sample L05-08, the smallest recognizable quartz grains are about 100 nm in size, have sharp grain boundaries forming often triple junction and are not cut by visible microfractures. Some triple junctions have extremely small voids between the grains. This micro-domain disappears moving away from the proximity of the pseudotachylyte injection vein tip (Fig. 4.11j, k).
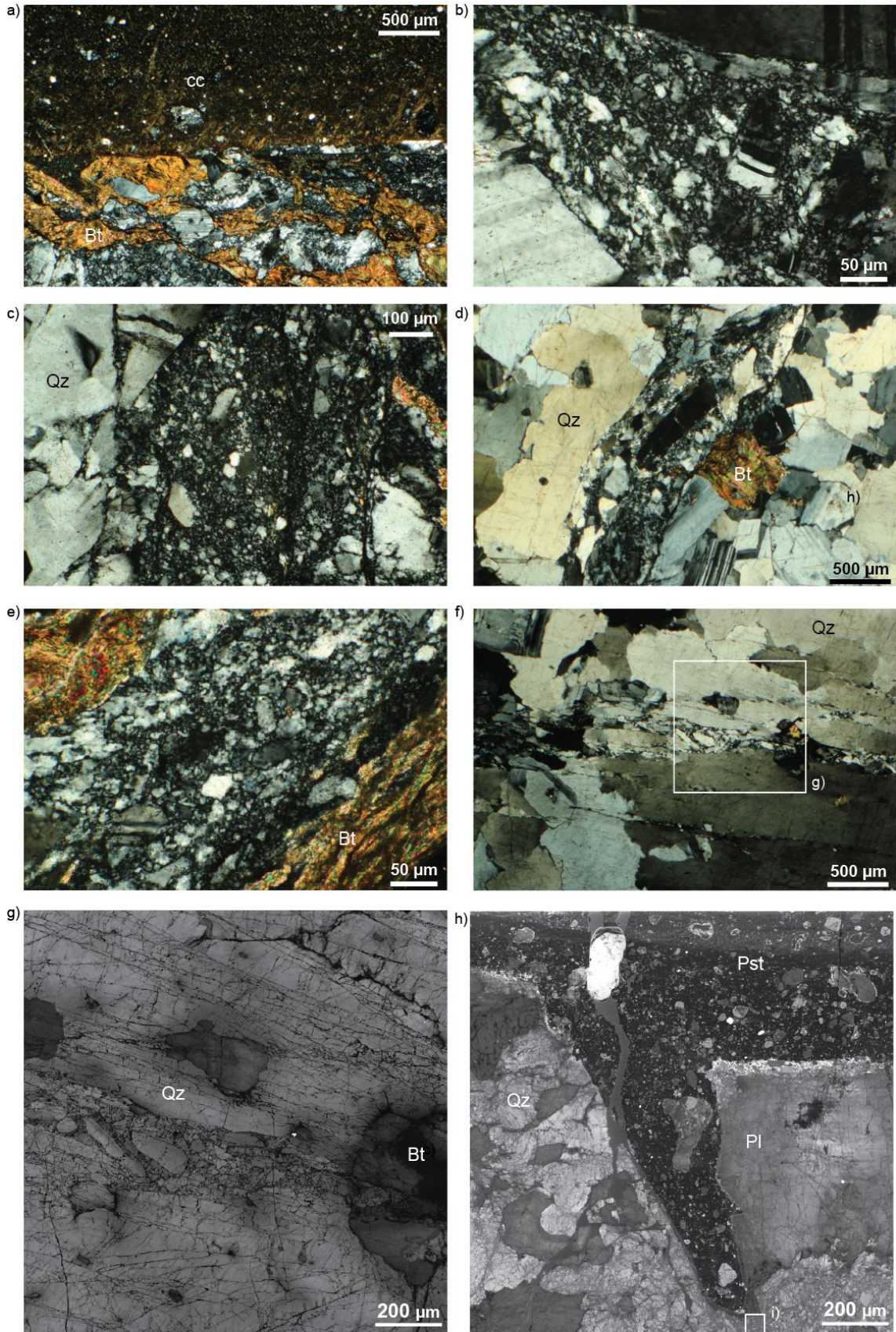
Fig. 4.11 Caption in the next page.
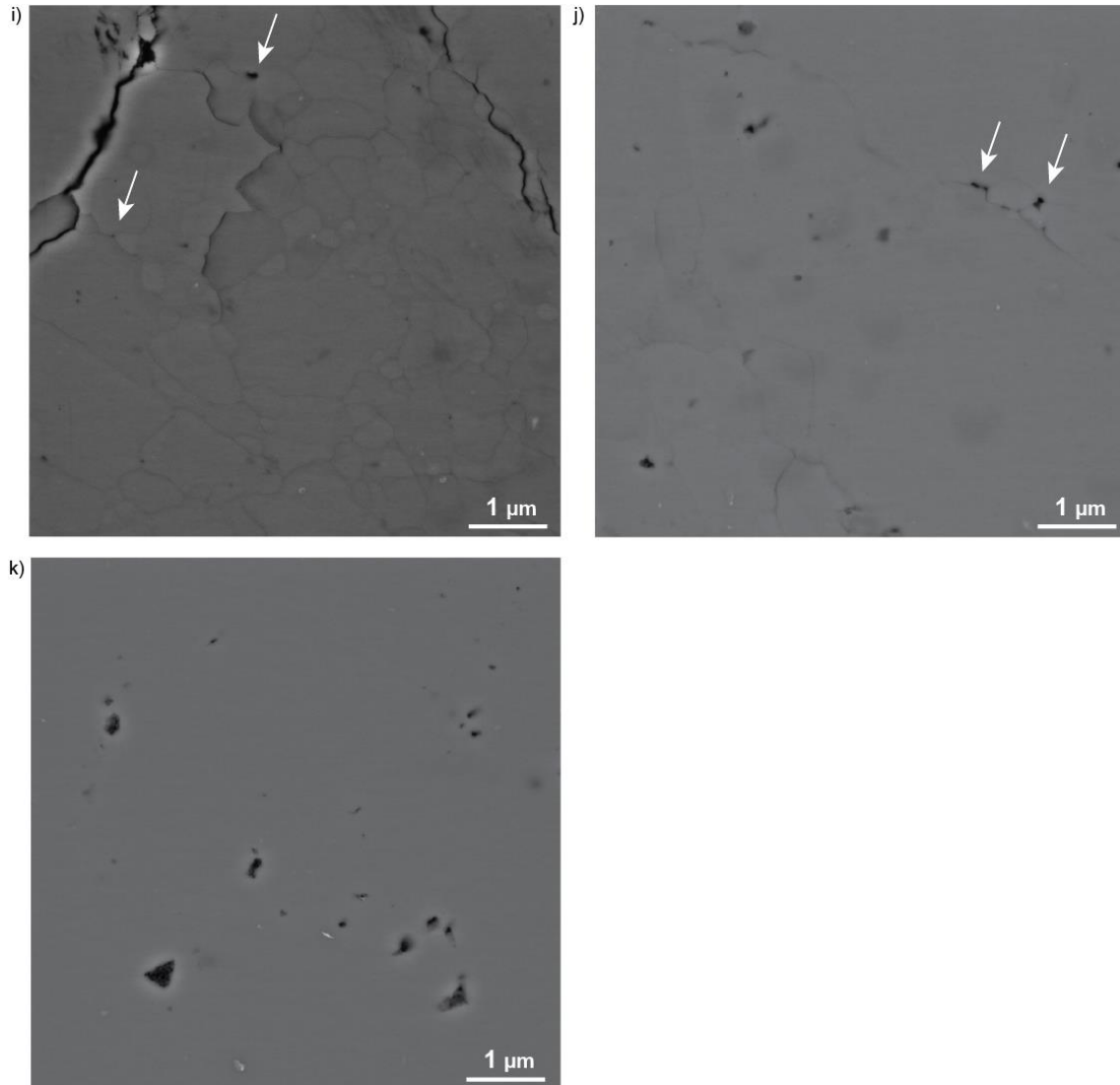
Fig. 4.11 Micro-domain of intense deformation with ultra-fine (< 100 nm) fragments in the natural thin sections. These are not visible at parallel Nicols. **a)** Micro-domain at the southern contact between pseudotachylyte-wall rock in thin section WF22-01b. **b)** Fracture in thin section WF22-01a decorated by the ultrafine micro-domain. Fragments of quartz and feldspars are recognizable. ~ 12 mm from the fault vein. **c)** Micro-domain decorating the macroscopic sub-vertical fracture in the southern side of thin section WF22-01b. ~ 10 mm from the fault vein. **d)** Micro-domain in the southern side of the fault, thin section WF22-01c; ~ 15 mm from the fault vein. **e)** Micro-domain along a fracture between two biotite grain, southern side of thin section L05-08. ~ 4 mm from the fault vein. **f)** Sub-horizontal microfracture with micro-domain in the northern wall rock, thin section WF22-01; ~ 10 mm from the fault vein. **g)** Enlargement of the previous picture; fragments have sharp and angular boundaries. **h)** Microfracture pattern and micro-domain at the tip of the bigger injection vein of thin section L05-08. **i)** Micro-domain at the tip of the injection vein of the previous figure; the quartz grains display triple junctions and straight borders. **j)** Micro-domain at ~ 0.5 mm from the fault vein of thin section L05-08; the grains are bigger, and less triple junctions are present. Small voids are present between grains at the triple junctions (white arrow). **k)** Absence of the micro-domain at higher distances from the fault vein of thin section L05-08 (~ 6 mm). a), b), c), d), e), f) optical microscope image, crossed Nicols; g) SEM-CL microimage; i), l), m) mid angle SEM-BSE microimages.

4.2.2 Microfractures orientation and density in natural pseudotachylytes

Orientation and density of the microfractures in the wall rocks is broadly related to the distance from the pseudotachylyte fault vein and the geographical side (northern or southern) in which they are located (see Fig. 4.9 and 4.10). The microfractures in the FESEM-CL images were first manually drawn on the image and then divided in segments of constant length (10 μm) (see Chapter 3.5.1). The microfracture density δ was calculated as:

$$\delta = \frac{\Sigma\ segments}{A} \quad (seg/mm^2) \quad \text{Eq. 4.1}$$

or the total number of the 10 μm-long segments divided by the area of the FESEM-CL microimage (1.64 mm²). The FESEM-CL microimages used for the production of the data presented in Table 4.1 and Fig. 4.12 are reported in Fig. 4.5 (also available in Appendix A).

Table 4.1. Results of the segment density calculation for the natural thin sections. The area considered is the one of FESEM-CL images, 1.64 mm².

SAMPLE	DISTANCE (from the fault vein)	NUMBER OF SEGMENTS (10 μm)	SEGMENT DENSITY (seg/mm²)
L05-08 (N)	5 mm	10433	6361.585
L05-08 (S)	0 mm	21457	13083.537
L05-08 (N)	0 mm	12495	7618.902
L05-08 (S)	7 mm	16460	10036.585
WF22-01a (N)	20 mm	7791	4750.610
WF22-01b (N)	0 mm	18137	11059.146
WF22-01b (S)	0 mm	22757	13876.220
WF22-01c (S)	22 mm	18832	11482.927

With respect to the pseudotachylyte vein, the microfractures in the northern wall rock are less dense and their orientation less scattered than in the southern wall rock. The latter displays higher complexity and fracture density in all the wall rock thickness analysed (Table 4.1). The microfracture density in both the northern and southern side, at the pseudotachylyte-wall rock contact is comparable between samples L05-08 and WF22-01b. Increasing the distance from the pseudotachylyte vein (5 – 7 mm), the density values are much higher in the southern side, and the same is for even higher distances (20 – 22 mm). However, at these distance, the number of the microfractures is sensibly decreased in both sides. The quantitative analysis of the FESEM-CL microimages evidence a clear decreasing trend in microfracture density moving from the fault vein to the wall rocks (Fig. 4.12).
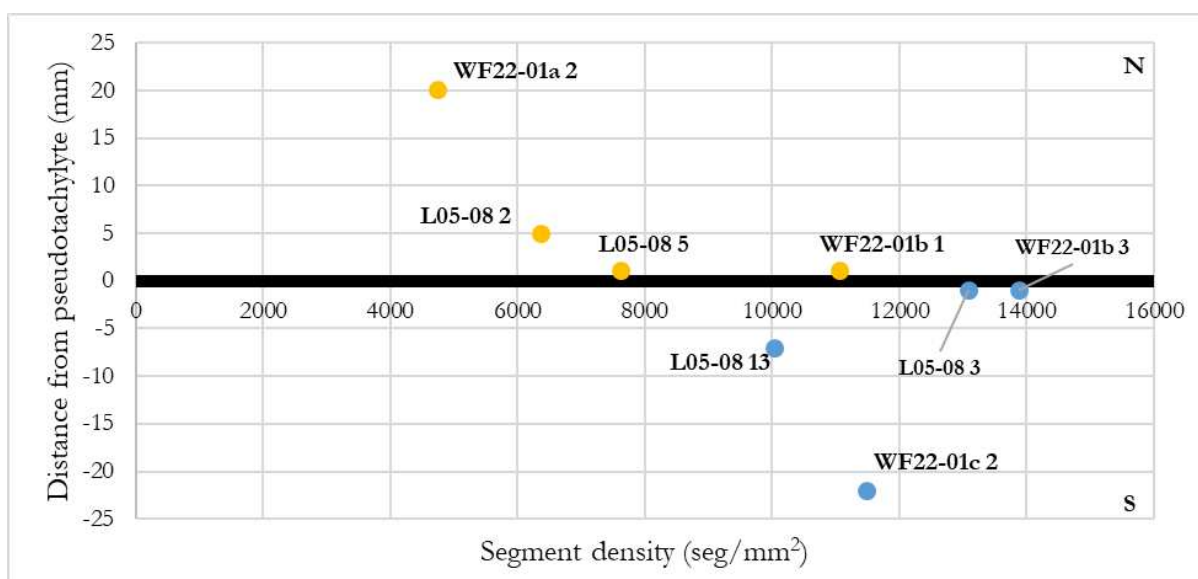
Fig. 4.12 Graph of the variation of the segment density with distance from the pseudotachylyte fault vein in the northern and southern wall rocks. Data are taken from Table 4.1; yellow dots represent N wall rock values and blue S wall rock values. Pseudotachylyte fault vein is at 0 mm, represented by the back line. With the exception of the density at -5 mm, on both sides it is possible to see a decrease in density moving away from the fault. The northern side shows sensibly lower density values.

The northern and southern wall rock display a clear preferential trend of the orientation of the microfractures, that is consistent in all the analysed thickness of wall rock. At the northern boundary between the pseudotachylyte and the tonalites, microfractures in both thin sections L05-08 and WF22-01b have a sub-horizontal trend, but in the first they strike preferentially at 50 – 70° while in the latter at 100 – 120° (Fig. 4.13, 4.14). Moving away from the fault surface, the microfractures horizontal trend becomes more evident, with preferential orientation at 80 – 100° and 90 – 100° respectively at 5 mm and 20 mm (in thin sections L05-08 and WF22-01a). Analysing the southern side, microfractures orientation data are more scattered, but still a preferential sub-vertical trend is always displayed. At 0 mm from the fault vein, sample L05-08 shows a microfracture pattern with two preferred orientations, the most frequent one, sub-vertical, at 0 – 20° and 160 – 180° and the secondary around 110 – 130° (Fig. 4.13, 4.14). Sample WF22-01b, at the same distance from the pseudotachylyte, shows instead only microfractures striking preferentially 0 – 20° and 170 – 180°. Increasing the distance, the microfracture orientation data are quite scattered, with a more pronounced set striking 0 – 10° and 170 – 180°, but also a high number of microfractures striking between 130-160° (thin section L05-08, 7 mm). In the most distal area, in sample WF22-01c, the microfracture has a striking preferential orientation of 20 – 30° (Fig. 4.13, 4.14). These could be correlated to the macroscopic sub-vertical fracture

already described in Chapter 4.2.1. This explains also the higher microfracture density even if at such high distance from the fault (Fig. 4.13, 4.14).
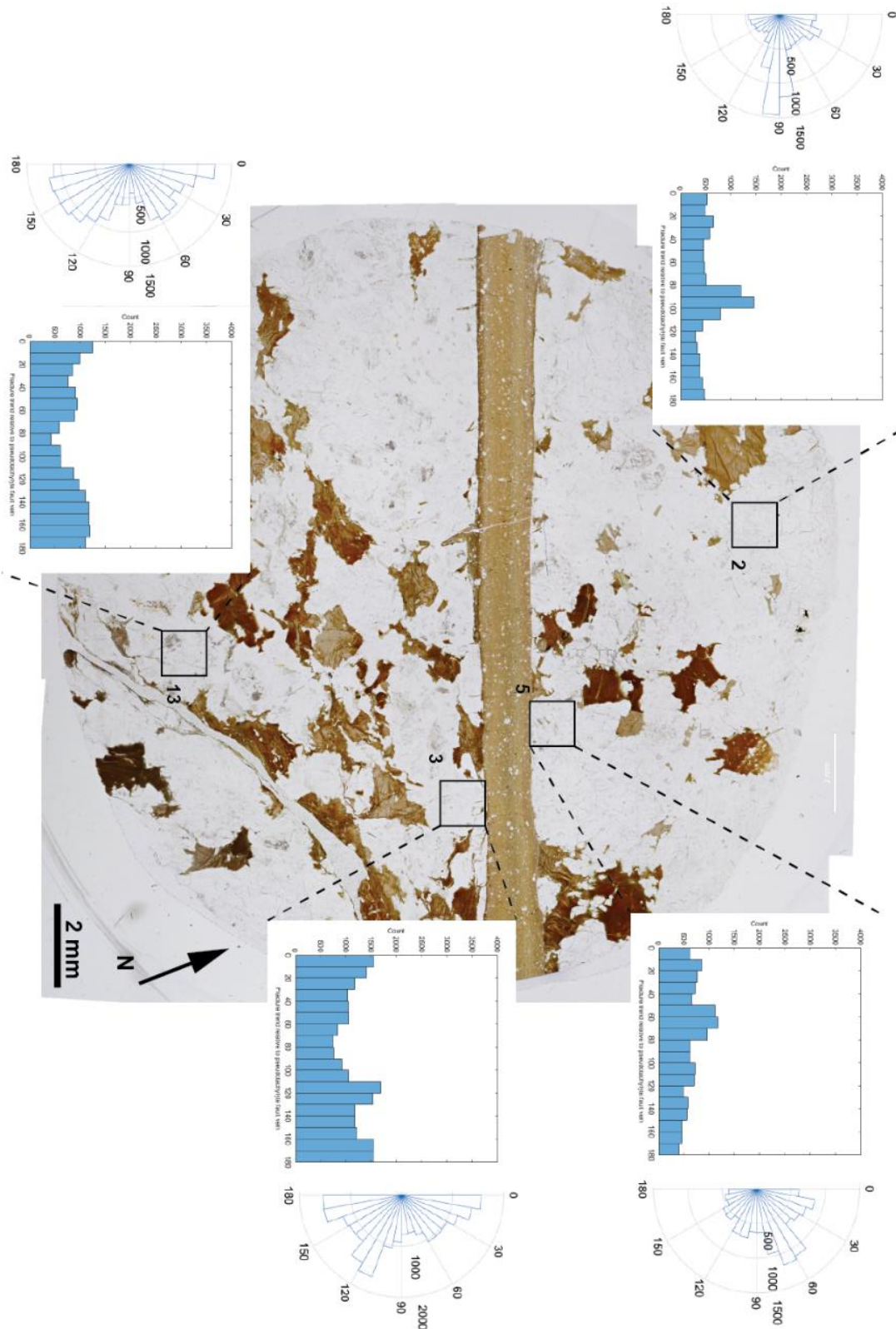
Fig. 4.13 Caption on page 54.
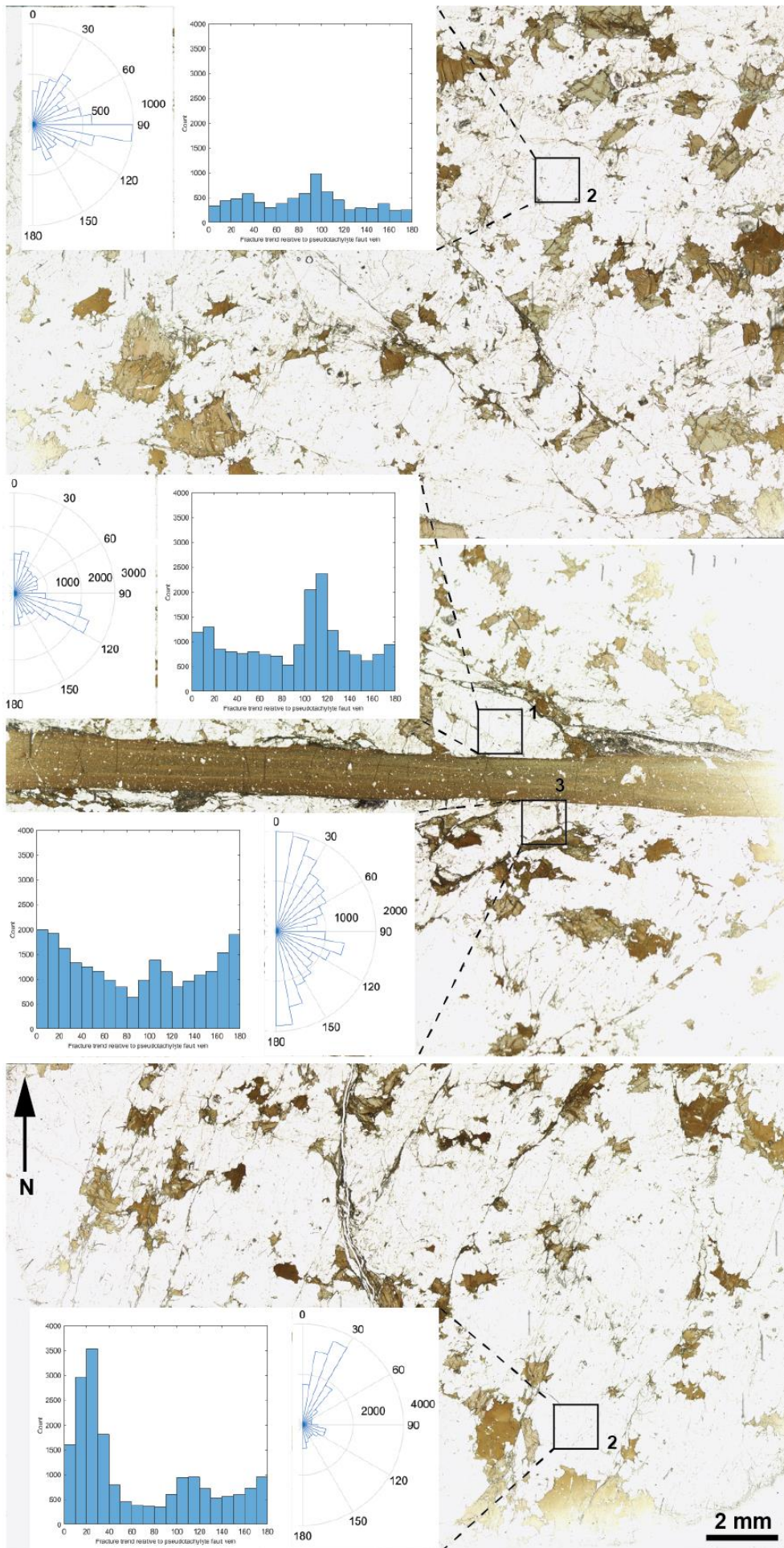
Fig. 4.14 Caption in the next page.

Fig. 4.13 Frequency histograms and rose diagrams of the microfracture pattern of thin section L05-08, with the area of acquisition of the FESEM-CL image for reference. The northern wall rock displays a preferential trend between 80 – 100° (5 mm) and 50 – 70° (0 mm) approaching the fault vein. The microfracture density is lower than in the opposite wall rock. In the southern side the data have more scattering but a sub-vertical preferential trend is still evident, with microfractures striking 0 – 20°, 160 – 180° (0 mm); a secondary trend is represented by the microfractures striking 110-130° in the area at the contact between wall rock and pseudotachylyte. At a distance of 7 mm from the fault vein the microfracture strike is more scattered, between 0 – 10° and 130 – 170°.

Fig. 4.14 Frequency histograms and rose diagrams of the microfracture pattern of thin sections WF22-01a, b, c. In concordance with the data of thin section L05-08, the northern side (WF22-01a, b) displays both near and away the pseudotachylyte fault a sub-horizontal preferential trend (90 – 100° at 20 mm from the fault vein and 100 – 120° at 0 mm), with low microfracture density. In the southern side instead the microfractures strike at 10 – 20°, 170 – 180° at the contact with the fault surface, with also here a secondary trend around 100 – 120° (0 mm), and 20 – 30° in the distal area (22 mm). The microfracture density is sensibly higher.

4.2.3 Clast (fragment) Size Distribution in natural pseudotachylytes

The largest consumption of fracture energy is associated with the formation of ultrafine rock fragments. In fact, fracture energy is proportional to the formation of new rock surfaces (Griffith, 1921). Consequently, a single rock fragment having the same volume as an aggregate of smaller fragments will have a smaller overall surface area and fracture energy than the aggregate. For this reason, as an end-member (i.e., estimate of the maximum seismic fracture energy), I determined the distribution of fragments in the micro-domains, or the areas of the wall rock where the smaller rock fragments are found (Fig. 4.11). The Clast (or fragment) Size Distribution in the micro-domains was built by exploiting (1) the FESEM-CL (i.e., manually drawn microfractures separating the fragments, grain size range 0.1 – 800 µm Fig. 4.5b), (2) the FESEM-EBSD (i.e., fragments distinguished by crystallographic orientation mismatch > 10°, grain size range 0.1-200 µm, Fig. 4.15) and, (3) mid-angle SEM-BSE (grain size range 0.002-2 µm, Fig. 4.11i) images. The FESEM-EBSD map shows for all the mineral phases a low mismatch angle between the fragments from a single grain (Fig. 4.15). The values of the equivalent diameter of the fragments were reported in a log-log graph (diameter of the fragments versus cumulative number of fragments), the standard method to represent grainsize distribution curves in literature (Fig. 4.16) (see also Chapter 3.5.2).
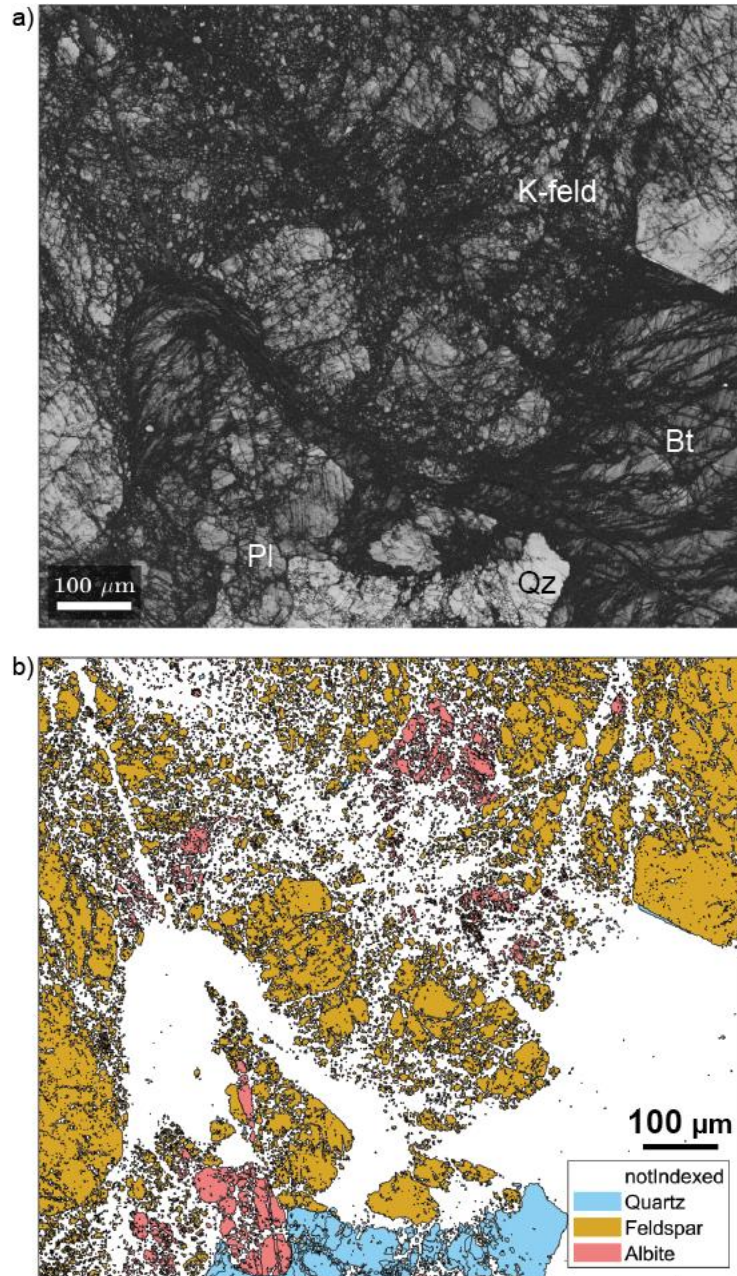
Fig. 4.15 EBSD data of the micro-domain at the tip of the major injection vein of thin section L05-08 (in Fig. 4.11h). **a)** Band contrast map. **b)** Elaborated EBSD map, without biotite, not considered for the calculation of the CSDs. Non-indexed areas are imaged with FESEM-BSE in Fig.4.11i. In the next pages: **c)** Inverse Pole Figure of x axis (IPFX), **d)** IPFY, **e)** IPFZ maps of plagioclase. **f)** Map of the misorientation of the fragments from the mean orientation of the crystal. **g)** IPFX, **h)** IPFY, **i)** IPFZ maps of K-feldspar. **j)** Misorientation from the mean orientation map of K- feldspar. **k)** IPFX, **l)** IPFY, **m)** IPFZ maps of quartz. The subgrains visible are the Dauphiné twins. **n)** Misorientation from the mean orientation map of quartz; the grains of quartz have a slightly higher misorientation with respect to plagioclase and feldspar.
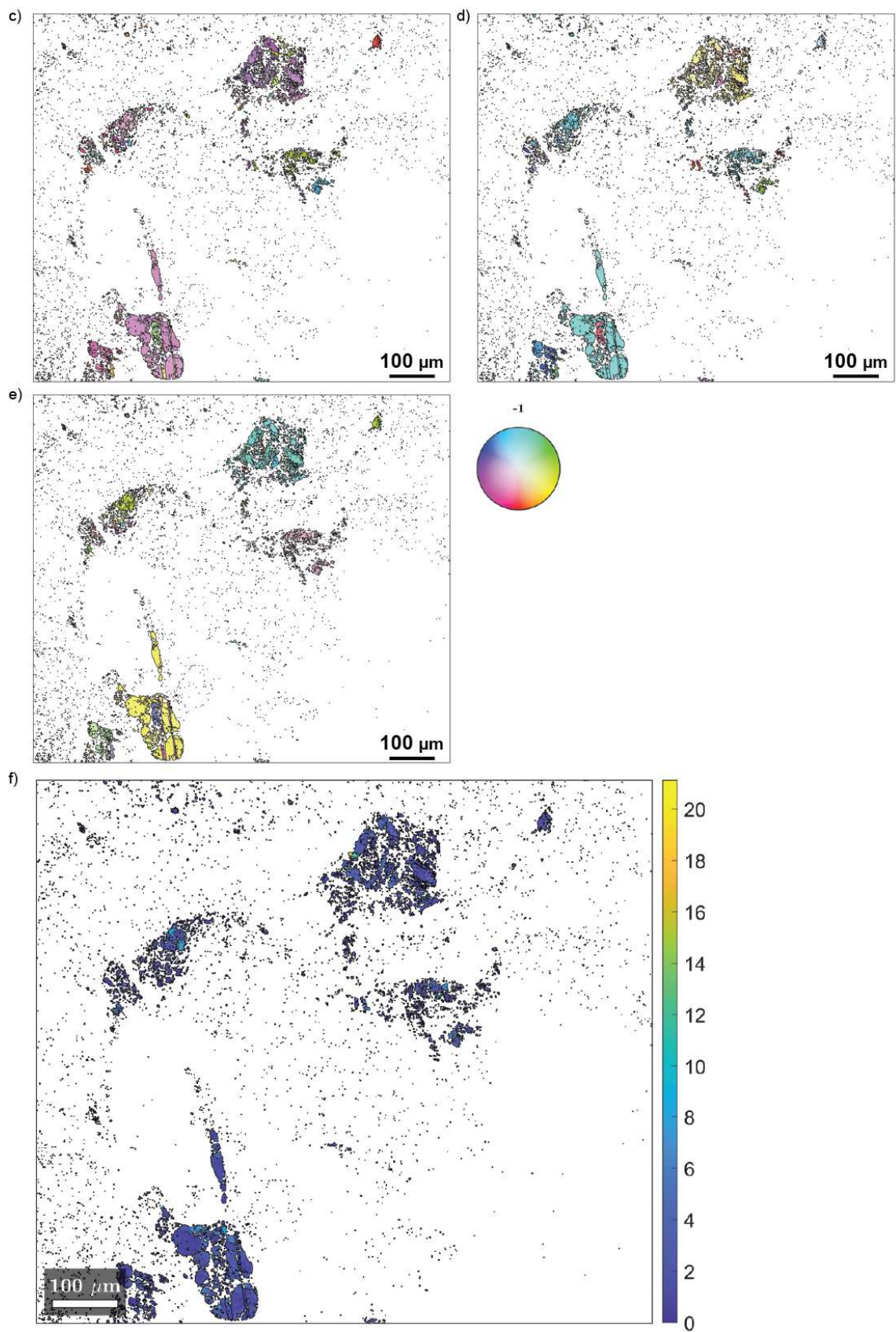
Fig. 4.15 Caption in the previous page.
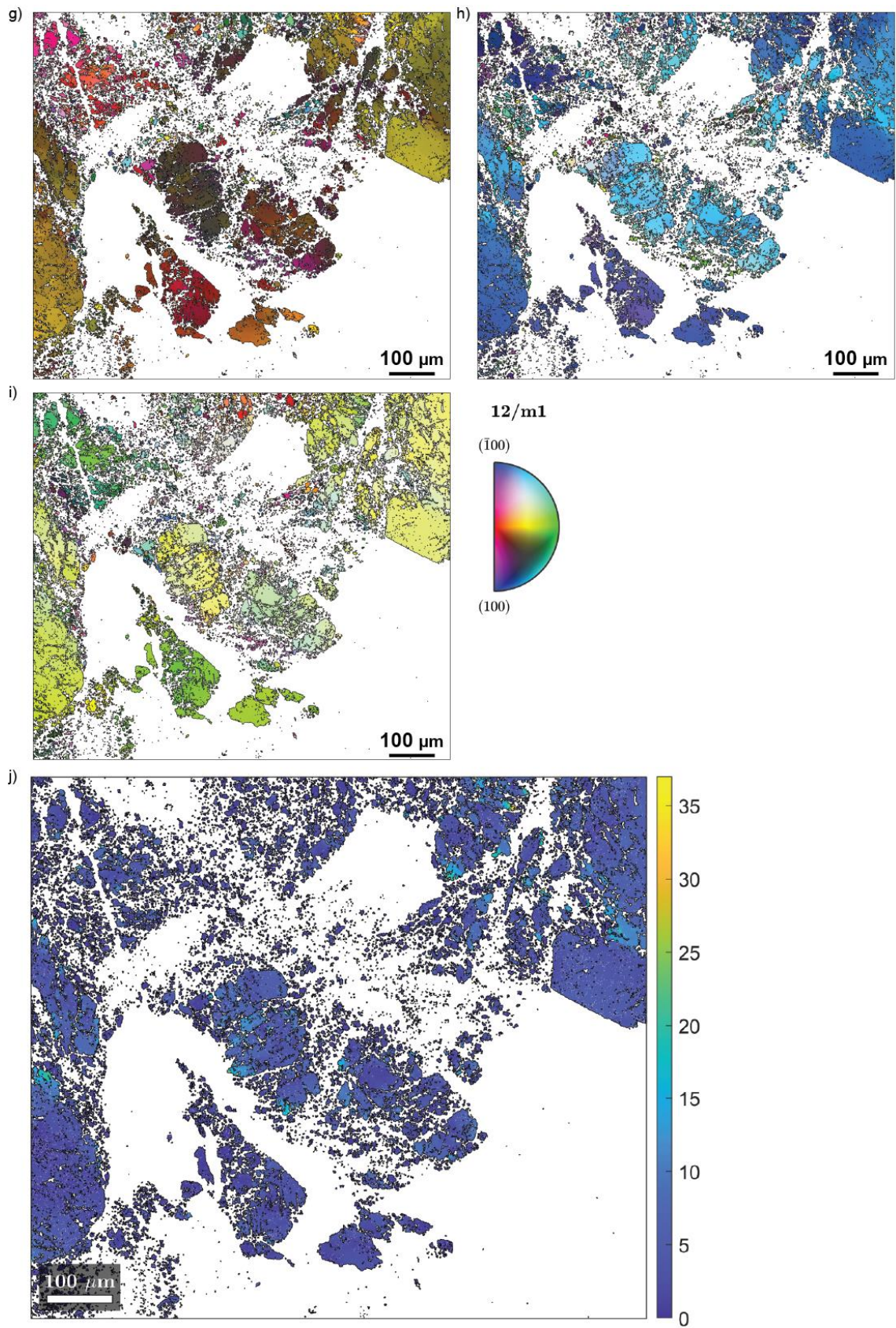
Fig. 4.15 Caption on page 55.
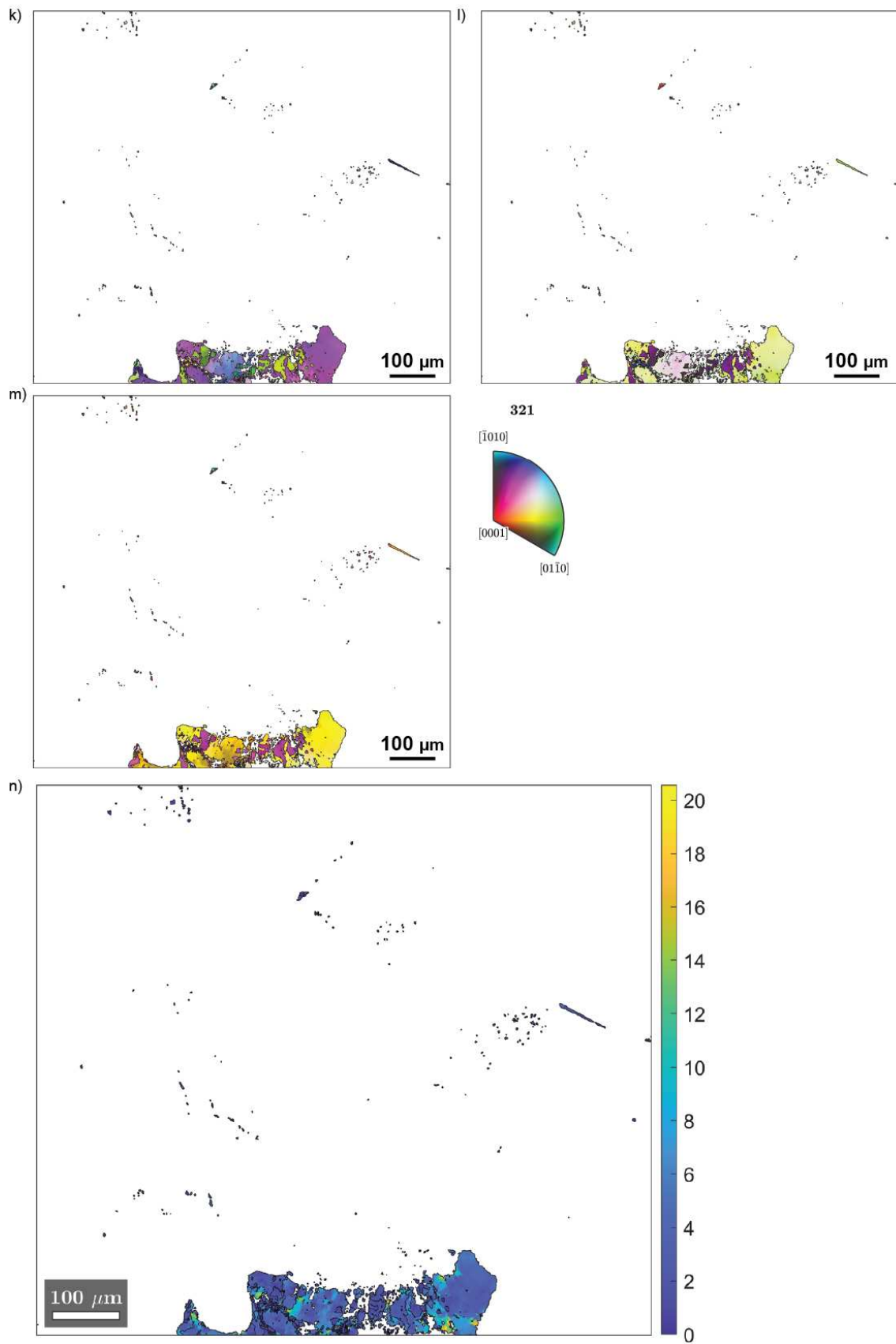
Fig. 4.15 Caption on page 55.
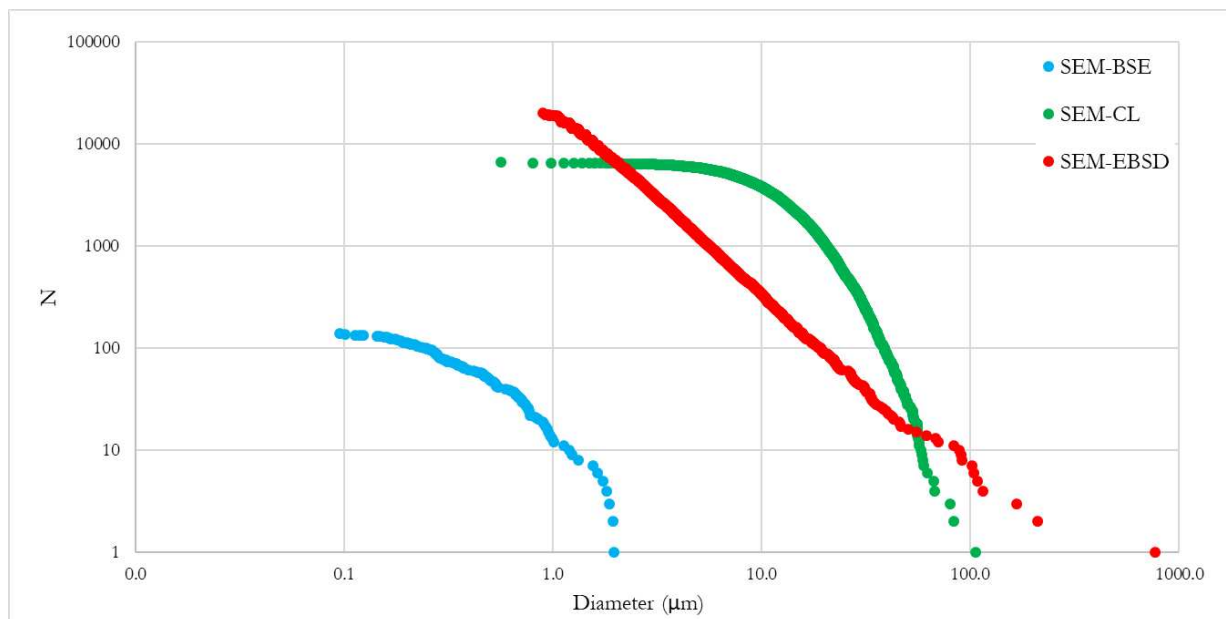
Fig. 4.16 Clast Size Distribution graph of the three analysed fragment intervals. The EBSD data curve displays a linear behaviour while data from FESEM-CL and high resolution mid-angle FESEM-BSE display two different slopes. The number of fragments of the FESEM-BSE microimage are limited due to the small area analysed.

4.3 Microstructures in experimental pseudotachylytes

The rock cylinders used in experiment HVR376 have the same mineral assemblage of the natural samples, though the grainsize is slightly larger and quartz and biotite are more abundant. Under the optical microscope, anomalous interference colours of the minerals are due to the thickness (> 30 μm) of the thin section (Fig. 4.17). Alteration of plagioclase (saussuritization) and of biotite (to chlorite) is widespread (Fig. 4.17a, 4.19c). Both quartz and feldspars often show undulated extinction. Biotite is dark in colour and kinked, possibly due to the diffusion of heat from the sliding surface during simulated seismic slip. At crossed Nicols, K-feldspar and plagioclase show twinning and concentric zoning, the latter visible also in FESEM-CL images (Fig. 4.18e). In FESEM-CL images quartz has a more homogeneous grey colour than in natural samples (compare Fig. 4.19e vs 4.8d).

The experimental pseudotachylyte fault vein is about 0.2 mm thick on average, so thinner than the natural one, and thickens up to ~ 0.5 mm towards the edges of the cylindrical rock specimen. Instead, in the central portion, the fault vein is < 0.05 mm thick and the rock cylinders are almost in contact (Di Toro et al., 2006; Lazari et al., 2023). The fault vein-wall rock contact is relatively rough (see also Lazari et al., 2023) with respect to the natural sample (Fig. 4.18e). The contact of the experimental pseudotachylyte with the wall

rock presents few embayments where the melt is in contact with biotite (Lazari et al., 2023). The pseudotachylyte is composed by a glassy-like matrix with embedded clasts which are more abundant and more angular with respect to clast found in the natural pseudotachylytes. The experimental pseudotachylyte is quite homogeneous in colour, without chilled margins, microlites or larger clasts in the middle portion (see for comparison the natural pseudotachylyte in Fig. 4.7). Few injection veins intrude the two rock cylinders. The experimental pseudotachylyte (Fig. 4.18c, d, e) do not include the micro-domains made of ultrafine fragments typical of natural pseudotachylytes (Fig. 4.11).
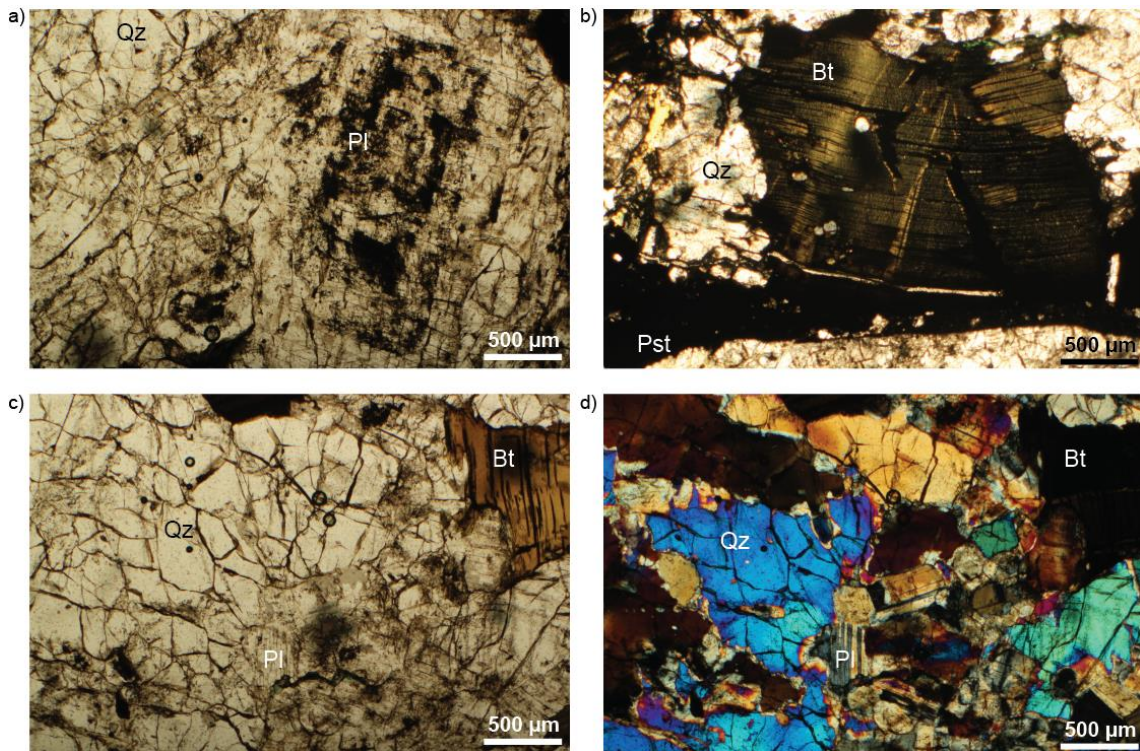
Fig. 4.17 Mineral assemblage of experimental sample HVR376. **a)** Alteration of plagioclase to sausurrite is widespread, more than in the natural thin section. **b)** Kinked biotite in contact with the experimental pseudotachylyte. **c), d)** Mineral assemblage; minerals show anomalous interference colours. a), b), c) Optical microscope image, parallel Nicols; d) Optical microscope image, crossed Nicols.
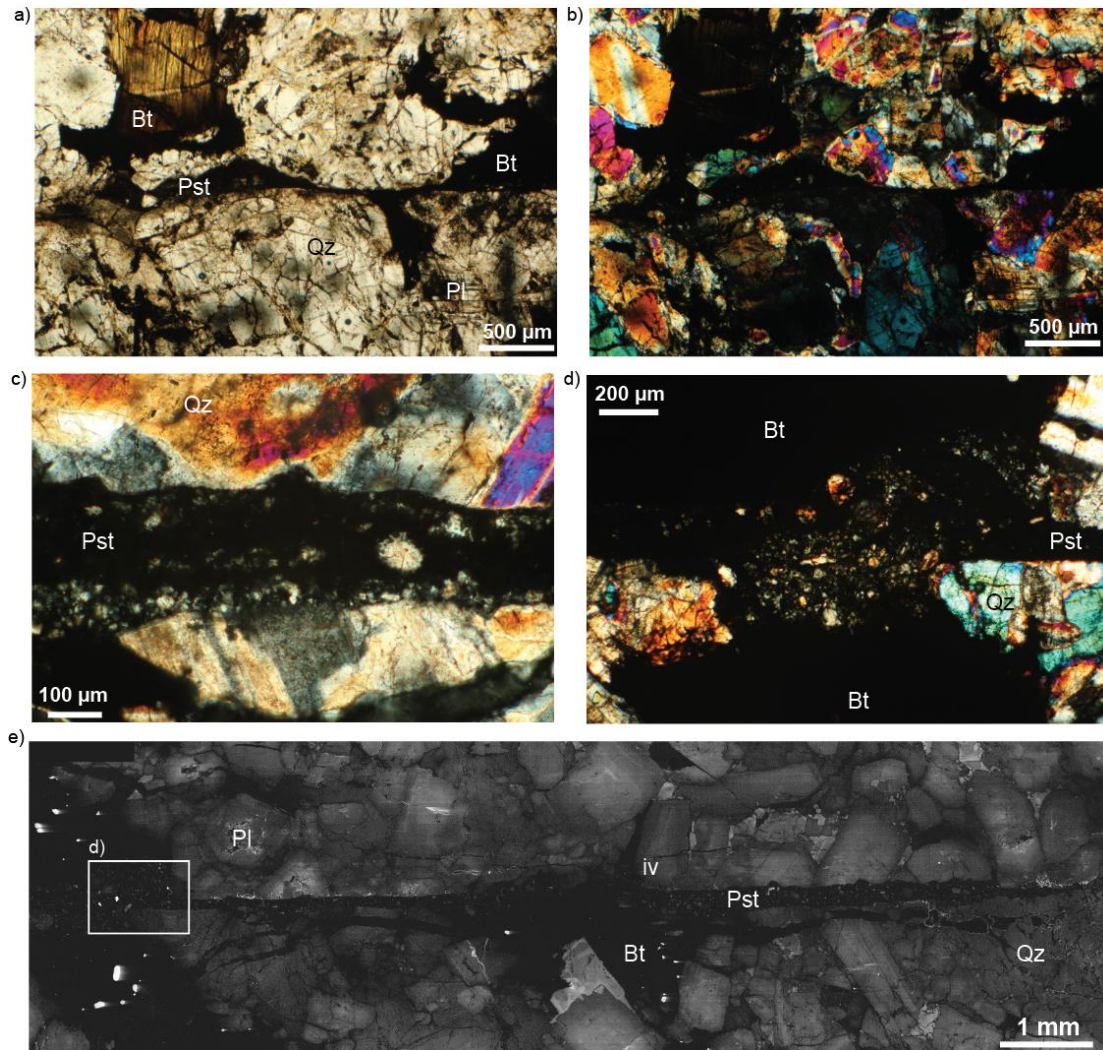
Fig. 4.18 Experimental pseudotachylyte characteristics. **a)**, **b)** Pseudotachylyte fault vein; the thickness is low with respect to the natural one. **c)** Inner structure of the pseudotachylyte, with survivor clasts from the wall rocks of quartz and feldspars. **d)** Embayment in biotite grains on both sides of the pseudotachylyte. **e)** Central portion of the pseudotachylyte fault vein, showing an injection vein intruding the northern wall rock. Absence of the micro-domain along the pseudotachylyte- wall rock contact is evident. The black line under the fault vein is a fracture in the thin section. a) Optical microscope image, parallel Nicols; b), c), d) optical microscope image, crossed Nicols; e) SEM-CL map.

4.3.1 Microfractures in experimental pseudotachylytes

The damage in the wall rocks associated with pseudotachylyte production in sample HVR376 is limited. The microfracture pattern is evident through optical microscopy: quartz, plagioclase and K-feldspar are pervasively cut by the microfractures and are divided in blocky fragments (Fig. 4.19). There is no preferential fracturing of quartz with respect to plagioclase or K-feldspar and most microfractures are intergranular. The microfractures are longer in proximity of the pseudotachylyte fault vein and are sub-horizontal (Fig. 4.19a).

Microfractures usually do not accumulate any offset and are open, and there are no fluid inclusions and mineral fillings healing and sealing the microfractures. A pervasive fracture system trending NNW-SSE is present in the rotary side of the sample, but it likely predates the experiments because of the chlorite mineralization present in the fractures (Fig. 4.19c). Under the optical microscope, the fracture density does not change much moving away from the experimental pseudotachylyte (Fig. 4.19). It is likely that some of the microfractures are
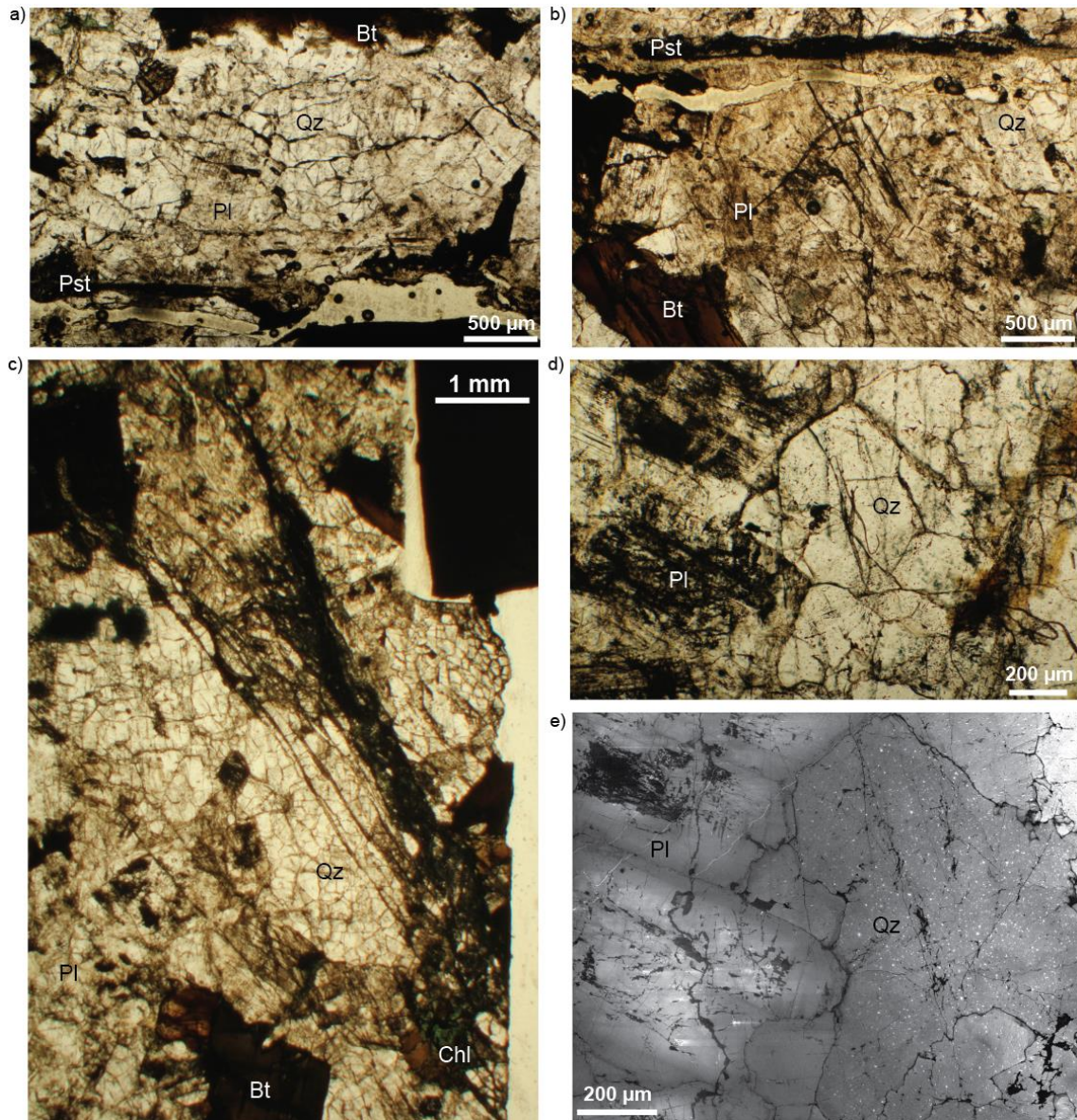
Fig. 4.19 a) Northern (stationary) and **b)** southern (rotary) sides of the thin section in proximity of the pseudotachylytes. The two d not display major differences; the microfractures in this area tend to be subhorizontal and slightly longer than in the domains far from the fault surface. **c)** Pervasive microfracture pattern departing from the lower right corner of the sample, with chlorite mineralization. **d)** Altered plagioclase and quartz affected by the fractures, showing a blocky subdivision. **e)** The same area of the previous image at SEM-CL. The amount of microfractures visible in here is lower than with the optical microscope due to the higher thickness of the thin section. a), b), c), d) optical microscope images, parallel Nicols; e) FESEM-CL image.

generated by edge effects (i.e. stress concentration at the borders of the cylinders), thus these regions were not considered for the microfractures description. There are no evidences of recrystallization processes in the sample (i.e., annealed grains at the tip of the injection vein), also in proximity of the pseudotachylyte.

4.3.2 Microfractures orientation and density in experimental pseudotachylytes

The quantitative analysis of the microfracture pattern was carried using FESEM-CL images both in the rotary and stationary samples, at the contact with the pseudotachylyte fault vein (see Fig. 4.4). Differently from the natural samples (Fig. 4.13, 4.14), the two experimental wall rocks do not show large differences regarding the orientation of the microfractures. The microfractures in the stationary side (N) have a weak preferential orientation towards 50 to 110° or sub-parallel to the pseudotachylyte strike (90°), while in the rotary side (S) microfractures have a weak preferential orientation towards 90 – 100° and 140 – 150° (Fig. 4.20). The microfracture pattern is not pervasive and the damage, based on optical and FESEM-CL observations, in both wall rocks is limited, especially if compared with the one found in the natural samples (compare Fig 4.19 with 4.9, 4.10). Because of this, the analysis of the microfracture pattern in the rest of the thin section was not performed. However, the rotary side has a slightly higher microfracture density with respect to the one of the stationary side (Table 4.2).

Table 4.2 Results of the segment density calculation for the experimental thin section. The area considered is the one of FESEM-CL images, 1.64 mm². The lower fracture density is evident in comparison with the results of Table 4.1.

SAMPLE	NUMBER OF SEGMENTS (10 μm)	SEGMENT DENSITY (seg/mm^2)
HVR376 1 (stationary, N)	4364	2660.976
HVR376 2 (rotary, S)	5025	3064.024

Because of the absence of the micro-domains found in the natural pseudotachylytes (Fig. 4.11), the Clast (fragment) Size Distribution curves for the experimental thin sections were not computed.
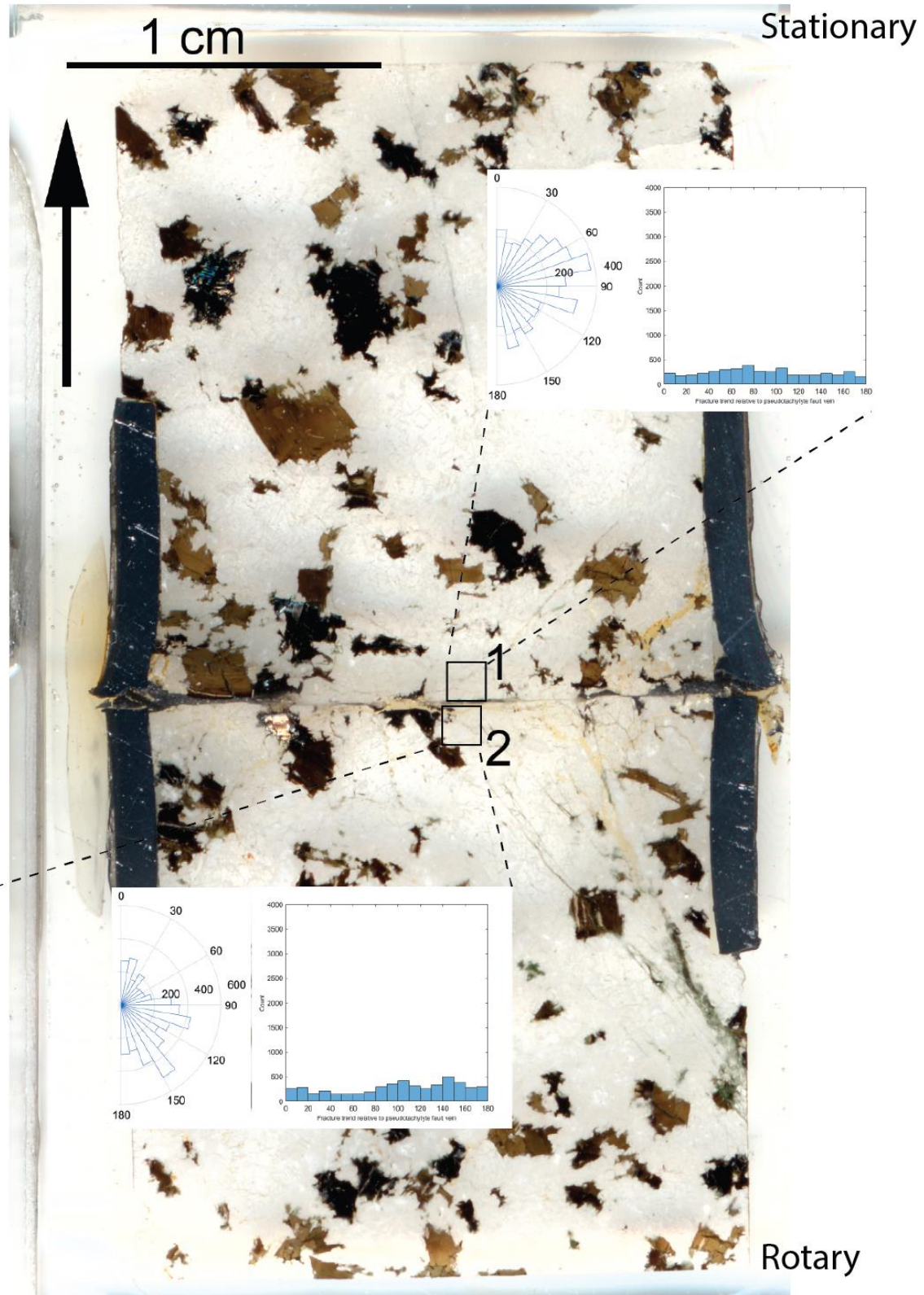
Fig. 4.20 Frequency histograms and rose diagrams of the microfracture pattern of thin section HVR376. The rotary and stationary side do not exhibit a huge difference in the microfracture pattern preferential orientation. The rotary side has a slightly higher fracture density, and a preferential strike around 140 – 150°. The microfracture pattern of the stationary side instead has a preferential strike around 60 – 80° and 100 – 110°.

5. Discussion

In the present Chapter, the formation of the natural microfractures described in Chapter 4 is discussed, along with the differences between the microfractures in natural and experimental faults. Following the work of Pittarello et al. (2008), the most dense micro-domain found at the tip of the selected injection vein is employed as a proxy for the estimate of the fracture surface energy per unit fault area U_S, or a fraction of the mechanical work dissipated during seismic faulting. A second energy sink, or the heat energy dissipated per unit fault area Q, is also calculated, and the values of U_S and Q are compared to estimate, at the scale of the studied outcrop, the partitioning of mechanical energy during earthquakes. The significance of these energy estimates is discussed in the framework of other estimates from the literature based on geological, seismological and experimental observations.

5.1 Seismic origin of the microfractures in natural pseudotachylytes

The interpretation of field and microstructural data suggests that the selected pseudotachylyte-bearing fault recorded possibly one seismic rupture (see Chapters 4.1 and 4.2). In fact, the absence of (1) mylonites and of sub-greenschist facies cataclasites nearby and inside the fault or in the form of clasts in the pseudotachylyte, (2) of the greenschist facies alteration around the fault, and instead (3) the presence of a continuous and homogeneous pseudotachylyte in the fault, are all evidences supporting this interpretation. Similar conclusions were made by previous studies on the same fault and other similar pseudotachylyte-bearing faults of the GLFZ (Pittarello et al., 2008; Griffith et al., 2010). Consequently, in the absence of other precursory slip events, most of the total offset of the fault can be attributed to a single seismic event. However, the slip displacement is not measurable from the fault outcrop, because markers such as aplitic dykes, gabbroic enclaves etc., that are often crossed by faults in the GLFZ, are missing. So, the fault offset was estimated with two methods (see also Chapter 4.1). The studied fault is 7 mm thick on average. In this field area, based on the statistics of pseudotachylyte-bearing faults where fault displacement can be measured because of the presence of displaced structural markers, the mean offset for a pseudotachylyte fault vein with thickness of ~ 7 mm is slightly less than 100 cm (Fig. 5 in Di Toro et al., 2005b). However, the statistics include also faults showing both cataclastites and pseudotachylytes, and the displacement associated to the formation of the pseudotachylyte might be overestimated. Griffith et al. (2010) estimated the offset of the

selected fault by measuring the length of the dilational jog (30 cm) located to the right of sample L05-08 at ~ 3.3 m along the fault sketch reported in Fig. 4.2. These estimates constrain the fault offset value between 30 and 100 cm. If the selected fault segment hosted a single seismic rupture, the estimated offset would be compatible with an earthquake of magnitude M_W 6 − 7 (Sibson, 1989).

From the microstructural observations presented in Chapter 4, the extreme difference between the microfracture pattern in the northern and southern wall rock is evident, both in orientation and density. The northern wall rock is systematically less affected by damage than the southern one, both in the volume just next to the pseudotachylyte fault vein and in the entire thickness of the wall rock surrounding it, and damage decreases moving away from the fault vein (Fig. 4.13, 4.14). The microfracture pattern varies systematically from northern to southern wall rocks, but is consistent between the different analysed volumes located on the same side, and at all distances from the fault vein. In fact, though with some scatter, the two patterns have a broad ~ 90° difference in orientation: with respect to the fault vein trend, most microfractures strike about perpendicular in the southern wall rock and sub-parallel in the northern wall rock (Fig. 4.9, 4.10, 4.13, 4.14) The above distribution is consistent, at the meso-scale, with the preferential orientation of the pseudotachylyte injection veins. Statistical analysis of 624 injection veins from 29 fault segments of the GLFZ showed that ~ 68 % of the injection veins intrude, often at ~ 90°, the southern wall rock (Di Toro et al., 2005a; Griffith et al., 2010; Lazari et al., 2023). This is especially true for pseudotachylyte-bearing faults with no cataclastic precursor (Fig. 5.1).

In the thin sections of the natural pseudotachylytes analysed in this thesis, no north-verging injection veins are present. However, microfractures are found also at ~ 2 cm from the fault vein, though their density is lower (4750.610 segments mm^{-2}) than in the southern rock (11482.927 segments mm^{-2}) at this distance (Fig. 4.12, 4.14). The dominant strike of the microfractures is similar to those measured next to the fault (Fig. 4.9, 4.10), so we infer that they were generated in the same stress field. In general, the highest damage (13083.537 segments mm^{-2}) is found just next to the pseudotachylyte fault vein, and especially at the tips of the injection veins, and decreases moving towards the wall rocks. In sample L05-08 there are no visible deformation structures in the nearby wall rocks and its microfracture density of 13083.537 segments mm^{-2} can be considered related only to the selected fault. Instead, sample WF22-01c, which has a very high microfracture density (11482.927 segments mm^{-2}), contains a long sub-vertical fracture, associated with a macroscopic injection vein, so the
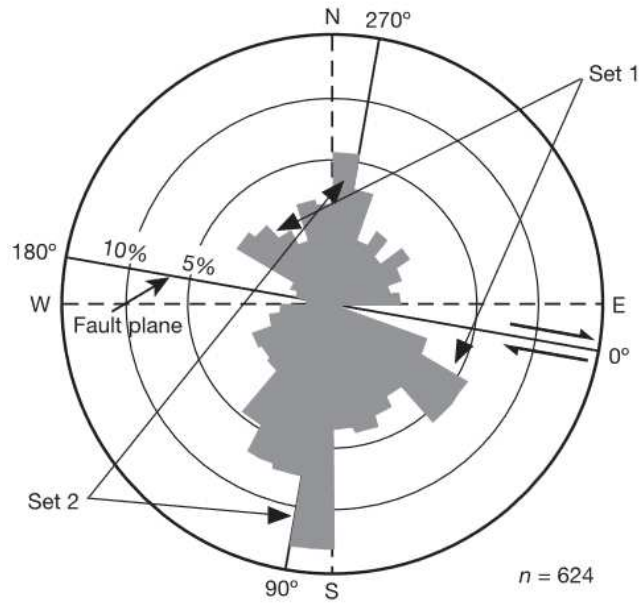
Fig. 5.1 Rose diagram of 624 injection veins from 29 fault segments of the GLFZ showing the preferential intrusion of the pseudotachylyte in the southern wall rocks. The grey area is proportional to the number of injection veins with that particular orientation. Set 1 has a preferential strike of 30-210°, while Set 2 of 90-270°. The microfractures discussed in this thesis have similar preferred orientation (see Fig. 4.10). From Di Toro et al. (2005a).

measured microfracture density might be related to both fractures (Fig. 4.3, red arrows). The wall rock volumes located more than 20 mm away from the fault vein were not analysed because, based on the measured decrease of microfracture density in the first 20 mm (Fig. 4.12) the contribution of this volume to the bulk fracture surface energy of the entire fault is considered irrelevant, compared to the one from the volume next to the fault. Moreover, nano-grains, which contribute the most to the bulk fracture surface energy (see Chapter 4.2.3) were not found in FESEM imaging of samples located at more than 1 mm from the fault vein (e.g., sample L05-08, Fig. 4.11k).

Previous studies also analysed the microfracture pattern associated to this and other faults of the GLFZ (Pittarello et al., 2008; Griffith et al., 2010). In particular, Pittarello et al. (2008) analysed the microfracture pattern of a single fragmented plagioclase clast located inside the pseudotachylyte with high resolution (down to 30 nm) SEM-BSE, and estimated the U_S in the slip zone. However, the microfracture pattern in the wall rocks was investigated without FESEM-CL. Because of this technical limitation, healed microfractures were not detected and their abundance largely underestimated. Instead, Griffith et al. (2010) analysed the microfracture pattern in the wall rocks of sample L05-08, among others, but with optical microscope. The microfractures were individuated through the presence of fluid inclusion

trails in quartz grains. This technical limitation, compared to the utilization of FESEM-CL as I did, resulted in a large underestimate of the real number of microfractures cutting the wall rocks. However, Griffith et al. (2010) captured some difference in the microfracture patterns in the two wall rocks but with less detail as in the case of the present thesis.

The studied fault probably records only one main seismic event, with no detectable precursory deformation history, so it is assumed that the damage investigated with FESEM-CL is related only to the single earthquake happened on the fault. In fact, the strong asymmetry of the density and orientation of the microfracture pattern (Fig. 4.13, 4.14), and of the pseudotachylyte injection veins (e.g., Fig. 5.1) can be interpreted as the result of the dynamic stress field around the fault during the propagation of the seismic rupture (see also Chapter 2.3). A Mode II fracture propagating along the fault at seismic rupture velocities (3 – 4 km s^{-1}) induces at the rupture tip a transient dynamic stress field in the wall rocks (Andrews, 1976; Di Toro et al., 2005a; Okubo et al., 2019) (Fig. 5.2). Numerical models showed that (1) the magnitude of the transient stress is proportional to the velocity of the rupture and, (2) the orientation of the maximum principal stress acting on the wall rocks is related to the sense of shear and rupture directivity (or direction of propagation of the rupture) (Di Toro et al., 2005a; Okubo et al., 2019). According to the theoretical and numerical models, supported by experimental evidence (Griffith et al., 2009) in the case of faults with dextral sense of shear, like the fault studied in this thesis (Fig. 4.2), a rupture propagating from left to right (or from west to east, see Fig. 5.2) would induce a compressional stress field in the northern wall rock and an extensional one in the southern wall rock. Moreover, the maximum principal stress is sub-parallel to the fault in the wall rock under compression (i.e., the northern one), and perpendicular to the fault in the wall rock under tension (i.e., the southern one) (Di Toro et al., 2005a) (see also Fig. 2.3). Because rocks are at least ten times weaker in tension than in compression, the southern wall rock is subjected to Mode I opening of fractures, and more in general to an extreme fracturing (Fig. 5.2). As a consequence, the injection of coseismic friction melt in the southern wall rock is facilitated (Fig. 5.1). Accordingly, in the southern wall rocks, the microfractures display a preferential sub-vertical trend; on the contrary, in the northern wall rock the compression generates less damage, due to the higher resistance of rocks to compressional stresses, and with a preferential sub-horizontal trend of the microfractures (Fig. 4.13, 4.14). Recent numerical models of earthquake rupture and associated fracturing show that the "coseismic off-fault damage" is triggered on both sides of the fault due to the stress concentrations associated to the dynamic rupturing (Okubo et al., 2019). The microfractures are generated

at the beginning around the rupture tip, and they grow forming a complex network as the rupture moves away and on-fault slip displacement increases. The tensional side of the fault is the most damaged. Instead, less fractures form in the compressional side (Fig. 5.2) (Okubo et al., 2019). According to the Andersonian faulting theory, in the case of a dextral strike-slip fault at failure, the orientation of the maximum and minimum principal stresses is respectively of 30° and 120° to the fault plane. However, with increasing rupture velocity approaching the Rayleigh speed ($v_{rupture} = 0.9\ v_{shear\ waves}$), a common rupture speed in natural earthquakes (Scholz, 2019), the principal stresses rotate until the maximum principal stress is oriented almost perpendicular with respect to the fault surface in the southern wall rock and approximately parallel in the northern wall rock (Di Toro et al., 2005a) (Fig 2.3). The microfracture pattern found in the natural thin sections (Fig. 4.9, 4.10) is thus consistent with a seismic rupture propagating on the selected fault at about the Rayleigh wave velocity. Opening of Mode I cracks occurs at seismogenic depths, even where the fault is subjected to large compressional stresses, because the seismic rupture propagation induces very large (> 1 GPa) tensional stresses (Di Toro et al., 2005a; Griffith et al., 2008; Di Toro et al., 2009; Griffith et al., 2009, 2012). Pre-stresses impact on the magnitude and orientation of the stress
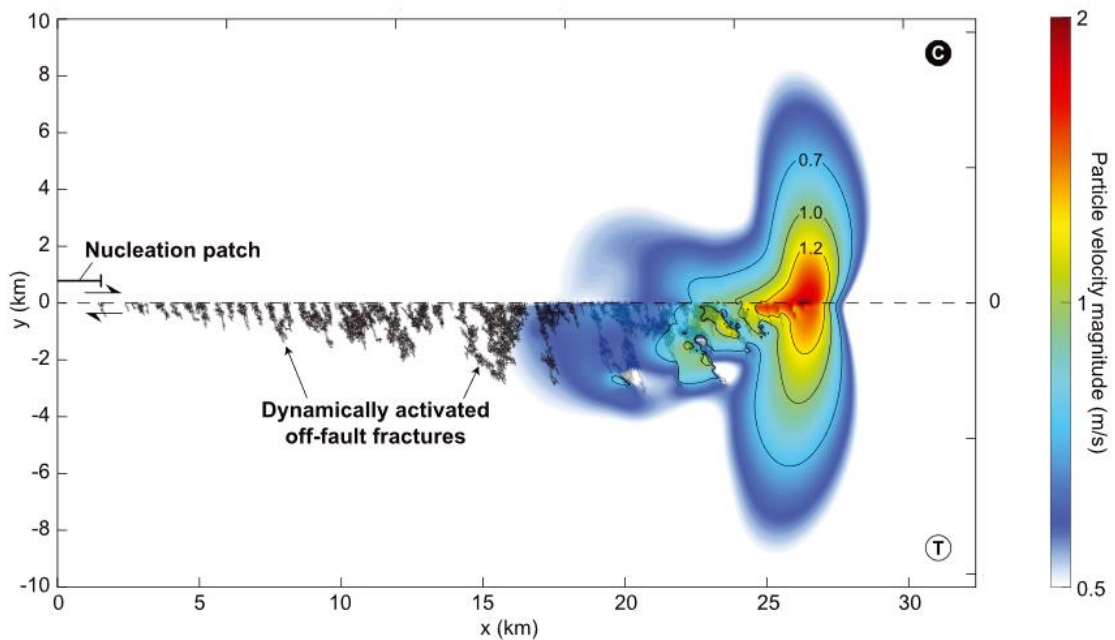
Fig. 5.2 Numerical model showing the strain field and formation of fault damage (off-fault fractures) associated with the stress perturbation at the tip of a seismic rupture propagating at Rayleigh waves velocity (0.9 the speed of the shear waves v_s from left to right on a fault perpendicular to the diagram. The fault has a dextral sense of shear, and tensional microfractures form in the southern wall rock as in the case of the studied natural fault. Though the model reproduces the geometry of a large scale fault (> 30 km long) the results of the model also apply to smaller faults. The colorbar indicates the velocity of the particles with a log scale. C=compression, T=tension. Modified from Okubo et al. (2019).

perturbation at the seismic rupture tip and on the resultant microfracture pattern orientation and density (Griffith et al., 2010; Lazari et al., 2023). In general, (1) fault surface curvature, (2) hydrofracturing related to the increase in volume due to the frictional melting of the rock, (3) presence of pre-existing fractures should be considered when interpreting the measured microfracture pattern. For instance, in the selected fault, the presence of a meso-scale injection vein intruding also the northern wall rock (see Fig. 4.2, sample WF22-03) cannot be related only to transient stress fields associated with rupture directivity. However, this further complexity can be possibly relaxed in the studied microfracture pattern because the selected samples come from a planar section of the fault.

From these evidences the relation between seismic rupture propagation, the related stress perturbation and the formation of a microfracture pattern is relatively clear. The damage caused by the propagation of the rupture is not confined only on the fault surface, but expands for a certain distance also in the wall rocks. According to the numerical model of reference by Di Toro et al. (2005a), the wall rock volume that underwent tensional and compressional stress perturbation is up to $20 - 30$ m thick, even if the stress magnitude decreases fast moving away from the fault surface (Fig. 2.3). However, microstructural evidences denote how the damage decreases rapidly already at distances around 20 mm from the fault vein (Fig. 4.12). Note that sampling of the wall rock was limited to the first ~ 10 cm from the fault vein, because of the presence of other faults, with their respective damage zones, located at few metres of distance.

5.2 Formation of microfractures in experimental pseudotachylytes

I investigated the microfracture pattern at the centre of the experimental sample HVR376 (Fig. 4.19). In fact, all rotary shear experiments, independently of the imposed slip rates and normal stresses, new fractures oriented at ca. $40 - 60°$ (or $130 - 160°$ in Fig. 4.20) with respect to the sliding surface, at the edge of the rock cylinders. Here the applied torque by the rotary column is the largest. This "edge effect" is the reason why external confining rings of aluminium or nickel are often installed in order to confine the rock cylinders and impede sample failure (Di Toro et al., 2006) (Fig. 4.20). As a consequence, the central volume of the experimental fault should be less affected by the peculiar stress field due to the experimental configuration.

Both stationary (referred also as N) and rotary (or S) sides of the sample display a similar but very low microfracture density compared to the natural pseudotachylyte. Instead, the attitude of the microfractures is different, with more microfracture sub-parallel to the fault vein in the stationary side. These sub-horizontal fractures could be the result of thermal cracking related to expansion and contraction of the rock under the applied normal stresses. In fact, rapid frictional sliding results in frictional heating and diffusion of heat in the wall rocks. The isotherms propagate parallel to the slip surface (the heat source), especially in the stationary side, were boundary effects are not as complicated as in the rotary side. Heat diffusion induces volumetric expansion of the rock cylinder perpendicular to the action of the applied normal stresses. Moreover, quartz is subjected to the phase transition $\alpha \rightarrow \beta$ at 573°C (i.e., quartz grains shift from trigonal to hexagonal symmetry) which induces a reduction in its resistance to compression by ca. one order of magnitude, leading to a rapid failure of the quartz-rich rocks also under compressional stresses. At the end of slip, the sample cools down and contracts, and most fractures open sub-parallel to the fault vein (and to the isotherms). In the rotary side, microfractures sub-parallel to the fault vein are less common. The different orientation of the microfractures in the rotary side could be related to (1) the cooling effect of air due to the rapid sample rotation (~ 1500 rotations per minute) and (2) the presence of a pre-existing fracture in the stationary sample. In fact, the main orientation of the microfractures in this side is 140 – 150°, very similar to the orientation of the fracture system present in the lower right corner of the experimental thin section (Fig. 4.19c). This fracture system propagates from the sample side towards the fault surface and may influence the microfracture pattern at the centre of the rock cylinder, where FESEM-CL investigation were performed (Fig. 4.4). These pre-existing fractures (in fact they are filled by chlorite in the bottom right of Fig. 4.19c) could have been reactivated during the experiment, especially because of "edge effects" typical of this experimental configuration. The pre-existing fracture is absent in the stationary side because the rock cylinders used in the experiment are two separated pieces. The microfracture pattern at distances > 2 mm from the experimental pseudotachylyte was not analysed quantitatively because FESEM-CL microimages showed that the damage related to the experiment is located in the first millimetres from the fault surface.

The difference between the microfracture pattern of the natural and experimental faults is evident (see Table 4.1 vs 4.2). Natural samples have a microfracture density next to the pseudotachylyte vein which is one order of magnitude higher than the one measured in the experimental faults (13083.537 segments mm^{-2} vs. 3064.024 segments mm^{-2}, comparing

the southern and the rotary sides). Moreover, the southern wall rock of the natural samples has a larger microfracture density (13083.537 segments mm^{-2}) than the northern wall rock (7618.902 segments mm^{-2}): this asymmetric distribution is absent in the experimental fault (compare Fig. 4.13, 4.14 with 4.20). Second, in natural samples the different orientation of the microfractures between northern and southern wall rocks is striking (Fig. 4.13, 4.14), while the two wall rocks of the experimental thin sections display a subtler difference: in the stationary side, the majority of the microfractures are subhorizontal, even if they have a wide scatter, while in the stationary side the microfractures are preferentially oriented at 140 – 150° (Fig. 4.20). The different pattern of damage in the wall rocks is also recorded by the distribution of the few (micro-) injection veins, visible only under the optical and scanning electron microscopes, found in the natural and experimental samples. In the first case, the injection veins are found only intruding the southern wall rock, while the injection veins of the experimental fault are found intruding also the stationary (N) side (Fig. 4.7, 4.19).

The striking differences listed above between natural and experimental microfracture patterns can be explained by the absence of a propagating seismic rupture, and associated intense and transient stress field in the experimental fault (Lazari et al., 2023; Yao et al., 2023). In the latter, simulated seismic slip occurs along the contact surface of the two rock cylinders. Other than local stress perturbations induced by the sample, "edge effect" and the presence of a pre-existing large fracture, micro-fracturing occurs driven by heat transient propagating inside the rock cylinders which results in a quite symmetric distribution of the damage. Instead, the intense asymmetric damage (i.e., microfracture density and orientation) found in the wall rocks of the natural faults, rather than thermal, is mainly caused by the rupture propagation and the associated large (> 1 GPa) compressional and tensional stress transients (see also discussion in Lazari et al., 2023).

5.3 Estimate of seismic surface energy U_S

In the wall rocks, micro-domains of finely comminuted grains of quartz, plagioclase and K-feldspar are found next to the pseudotachylyte fault and injection veins and interpreted as resulting from seismic rupturing (see discussion in Chapter 5.1; Di Toro and Pennacchioni, 2005). Next to the pseudotachylyte, the crystallographic axes of the neighbour comminuted grains belonging to the same mineral have low mismatch angles (< 10°, see EBSD Inverse Pole Figures and mean orientation maps of Fig. 4.15). The low values of

mismatch angles are interpreted as due to the brittle *in-situ* fracturing process that generated the comminuted grains formed during rupture propagation (coseismic fault damage).

In the micro-domain at the tip of the major injection vein of sample L05-08 the (1) broad grainsize distribution ranging from ~ 90 nm to ~ 2-3 μm (Fig. 4.11i), (2) low crystallographic mismatch between the grains (Fig. 4.15) and (3) presence of sub-euhedral quartz grains with straight grain boundaries often forming triple junctions (Fig. 4.11i) are indicative of brittle fracturing (response of the broad grainsize distribution) followed by diffusion-controlled grain boundary migration (i.e., static recrystallization and annealing) (Passchier & Trouw, 2005; Bestmann et al., 2012) (Fig. 4.11i). These microstructures are less pervasive in the micro-domains located at 0.5 mm from the fault vein (Fig. 4.11j) and absent 6 mm far away (Fig. 4.11k). The presence of this annealed micro-domain only next to the pseudotachylyte fault vein indicates that the static recrystallization was driven by the heat generated during seismic frictional sliding along the fault. Syn- to postseismic (few seconds after seismic faulting) annealing processes may result in the disappearance of the smaller fragments. In fact, bigger grains grow at the expenses of the smaller ones, and this may impact on the measured Clast (fragment) Size Distributions (CSDs) and the estimates of the U_S (see below).

I determined the CSDs curves of the micro-domains using FESEM-CL, FESEM-EBSD and mid-angle FESEM-BSE images (see Chapter 4.2.3). The CSD can be described by a power-law (Pittarello et al., 2008):

$$N(r) = r^{-D} \quad \text{Eq. 5.1}$$

where D, which corresponds the slope of the distribution, is the two-dimensional fractal dimension. All the CSDs curves have problems of undersampling at both ends, towards the smaller and larger grainsizes. This is due to (1) resolution limits towards the smaller grainsize (undersampling: e.g., the FESEM-CL CSD curve saturates at ~ 10 μm, more or less the resolution limit of the technique) or (2) to a physical process (i.e., the mid-angle FESEM-BSE CSD curve might saturate because of the disappearance of the smaller grains because of annealing processes) and (3) towards the large grainsize, the fact that only a few large fragments can be sampled in the limited area of the microimages (undersampling: this is especially the case of the mid-angle FESEM-BSE technique, that imaged an area of ~ 45 μm²). As a consequence, the slope or best-fit lines of the CSDs to obtain D were traced by removing the outliers, such as the tail at 100 μm diameter of the FESEM-CL curve, or the

one above 1.3 µm for the mid-angle FESEM-BSE curve (Fig. 5.3).

The CSD curve obtained from FESEM-EBSD measurements is described by a single best-fit line. Instead, the CSD curves obtained from FESEM-CL and mid-angle FESEM-BSE imaging can be described by at least two best-fit lines (and thus D values), with decreasing grainsize that is probably due to annealing processes (Fig. 5.3). The two D values obtained (1.10 and 1.94) are consistent with the D value (1.83) found by Pittarello et al. (2008) over a similar grainsize range (Fig. 5.4).
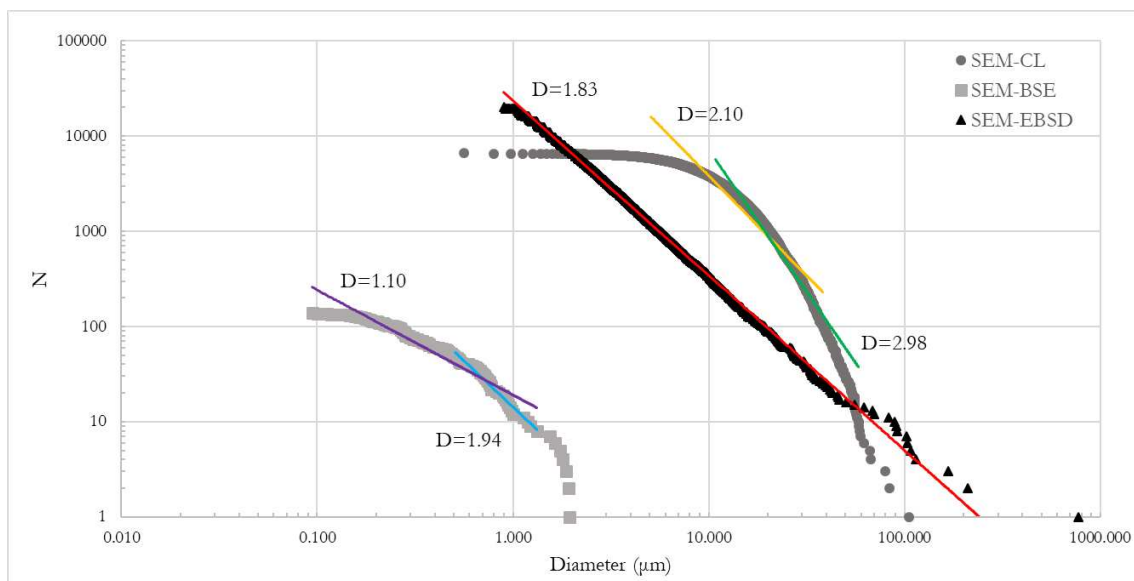
Fig. 5.3 Clast Size Distribution curves for FESEM-CL, FESEM-EBSD, mid-angle FESEM-BSE data. The CSDs of FESEM-CL and mid-angle FESEM-BSE can be described by two D values, obtained from two different best-fit lines (respectively yellow and green lines, and purple and blue lines).
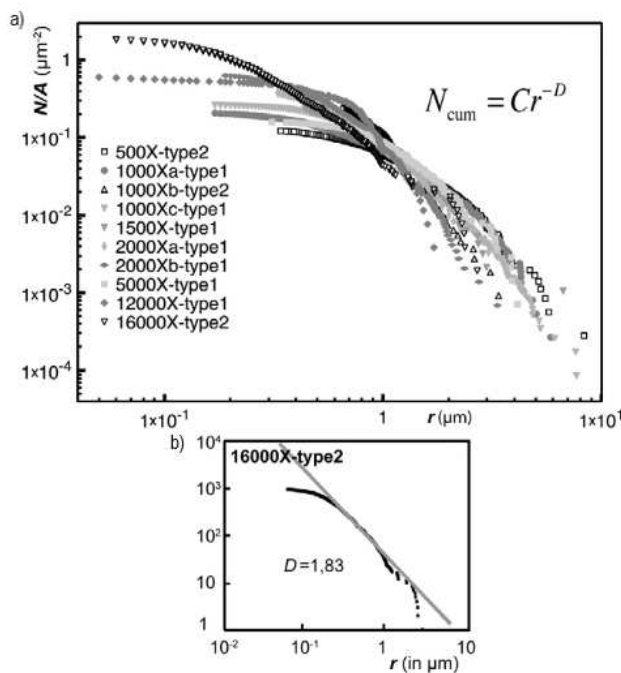
Fig. 5.4 Clast Size Distribution curves obtained by Pittarello et al. (2008), as a comparison to Fig. 5.3. In their case the measurements were done only on fragments of plagioclase grains inside the pseudotachylyte. Still, the distribution is consistent with the data presented in this thesis. **a)** Normalized distributions. **b)** Distribution employed for their surface energy calculation. Note that in the x axis is reported the equivalent radius and not the diameter of the fragments.

Instead, the CSD obtained over the same equivalent grainsize range (1 to 100 µm) in the same micro-domains from FESEM-CL and FESEM-EBSD data (see Chapter 4.2.3) differ substantially. While the CSD obtained from FESEM-EBSD is described by a single D = 1.83 (red best-fit line), the CSD obtained from FESEM-CL is described by two D, 2.10 and 2.98 (yellow and green curves) (Fig. 4.16 and 5.3). This difference could be related to the technique employed for data acquisition. In the FESEM-CL microimage, the grain boundaries were evident thanks to the grey colour contrast of the microfractures (Fig. 4.5b) and the fragments drawn by hand (see also Chapter 3.5.2). However, if the microfracture is sealed by minerals with the same composition of the fragments (eg., same Ti content in the case of quartz), it might not be detected. Instead, FESEM-EBSD technique does not allow to distinguish neighbour fragments with a mismatch angle < 10°, likely resulting in an underestimation of the total number of fragments. In any case, the reasons of the different CSDs resulting from the analysis of the FESEM-CL and FESEM-EBSD images is not clear. Anyway, the dataset was considered complete enough for the objectives of the present thesis, and the three CSDs of Fig. 5.3 were employed for the calculation of U_S.

Following the work of Pittarello et al. (2008) here below I estimate the fracture surface energy U_S associated with seismic rupture propagation. The energy dissipated per unit fault area during seismic slip is the mechanical work E_f, that is composed by frictional heat Q and surface energy U_S (Cocco et al., 2006):

$$E_f = Q + U_S \quad \left(^J/_{m^2}\right) \quad \text{Eq. 5.2}$$

Both these quantities cannot be estimated from seismological studies, but geological field evidences such as pseudotachylyte-bearing faults have proven to be a good proxy for both, as well as other earthquake source parameters (Di Toro et al., 2005b; Di Toro et al., 2006; Pittarello et al., 2008; Di Toro et al., 2009; Johnson et al., 2021; Lazari et al., 2023). The surface energy U_S can be calculated as follows (Chester et al., 2005):

$$U_S = (A_{SZ} + A_{DZ})\gamma \quad \left(^J/_{m^2}\right) \quad \text{Eq. 5.3}$$

with A_{SZ}, A_{DZ} being respectively the total surface of the microfractures (and fragments) per unit fault area in the slip and damage zone, and γ the specific mineral surface energy (about 1 J m^{-2} for quartz and 10 J m^{-2} for plagioclase, Brace & Walsh, 1962). As previously discussed, the damage found in the wall rocks only few millimetres away from the fault vein is negligible

with respect to the one found just next to the slip zone (Fig. 4.9, 4.10, 4.11). As a consequence, the value of A_{DZ} is considered as zero. Instead, the A_{SZ} in the slip zone is virtually unknown, because the grains formed at the rupture tip melted in the slip zone to produce the frictional melt (Spray, 1995; Pittarello et al., 2008). However, A_{SZ} can be approximated by the total surface of the fragments measured in the micro-domains at the tip of the injection vein of sample L05-08 (Fig. 4.11h). In fact, here the micro-fragments associated with seismic rupturing were preserved from melting. So from the CSDs obtained with FESEM-CL, FESEM-EBSD and especially mid-angle FESEM-BSE is possible to determine A_{SZ}, in the micro-domain and then over the entire thickness of the pseudotachylyte vein (see Eq. 5.8 below). The determination of A_{SZ} in the micro-domain requires the estimate of the intercept C of the best-fit lines of the CSDs with the *y*-axis. Because the CSDs can be described by five best-fit lines (two for both FESEM-CL and mid-angle FESEM-BSE, and one for FESEM-EBSD, Fig. 5.3), five intercept values were obtained, considering the smallest fragment diameter of each Clast Size Distribution curve (Fig. 5.5).
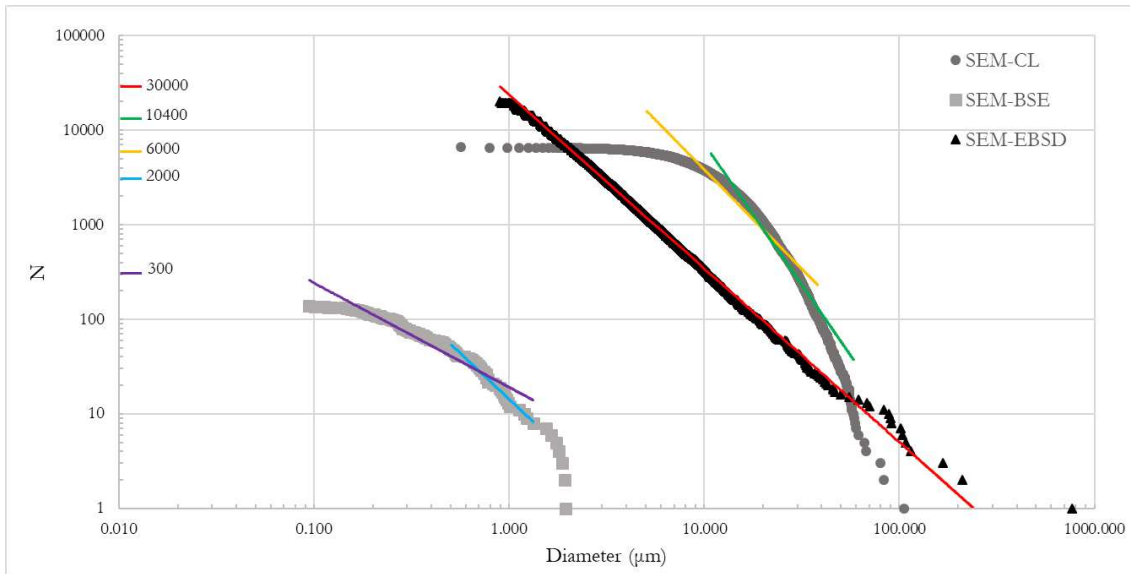
Fig. 5.5 Ordinate- intercept C values for the five best fit lines of the Clast Size Distributions. FESEM-CL: yellow (C ~ 6000) and green (C ~ 10400) values, FESEM-EBSD red value (C ~ 30000), FESEM-BSE purple (C ~ 300) and blue (C ~ 2000) values.

To estimate U_S, the two-dimensional fractal dimension D has to be converted into a three-dimensional D^*, by adding a real number D' between 0 and 1 (Mandelbrot, 1977):

$$D^* = D + D' \quad \text{Eq. 5.4}$$

For the calculations in this thesis two values of D' have been selected as the two end-members, respectively 0 and 1. The total surface area of the fragments in the area of a single microimage is (Pittarello et al., 2008):

$$A_{SZ_i} = \int_{r_{i(min)}}^{r_{i(max)}} 4\pi r^2 dN \approx \frac{4\pi C D_i^*}{2-D_i^*} \left(r_{i(max)}^{2-D_i^*} - r_{i(min)}^{2-D_i^*} \right) \quad \text{Eq. 5.5}$$

where C is the intercept of the best fit line and $r_{i(min)}$, $r_{i(max)}$ are the smallest and biggest fragments radius, respectively. Assuming that the particles are spherical, the volume of the fragments in the area of a microimage of the micro-domain is obtained:

$$V_{SZ_i} = \int_{r_{i(min)}}^{r_{i(max)}} \frac{4}{3}\pi r^3 dN \approx \frac{4\pi C D_i^*}{3(3-D_i^*)} \left(r_{i(max)}^{3-D_i^*} - r_{i(min)}^{3-D_i^*} \right) \quad \text{Eq. 5.6}$$

The ratio n between this volume and the volume of the pseudotachylyte fault vein V_{SZ}, calculated as in Eq. 5.7, is then computed. This is needed to determine how many times n the micro-domain volume fits in the unit volume of the slip zone.

$$V_{SZ} = w * 1 \, m^2 = 7 \, 10^{-3} \, m^3 \quad \text{Eq. 5.7}$$

$$n = \frac{V_{SZ}}{V_{SZ_i}} \quad \text{Eq. 5.8}$$

To obtain the total surface area of the fragments per fault unit area A_{SZ}, the area A_{SZ_i} is multiplied by n. Lastly, A_{SZ} has to be multiplied by γ (Eq. 5.3) to obtain the total surface energy U_S. The grain fragments of the various grainsize distributions belong to different minerals (quartz, plagioclase, K-feldspar). The majority of these is composed by plagioclase, thus the value considered for the specific surface energy γ is the one of plagioclase, as in Pittarello et al. (2008). This also because the specific surface energy of plagioclase is higher than the one of quartz (10 J m^{-2} vs 1 J m^{-2}, Brace & Walsh, 1962), so this will eventually lead to an overestimation of the total U_S. The estimated U_S, calculated for the different CSDs, are reported in Table 5.1.

Table 5.1 Slopes (D) and intercept (C) values of the five best-fit lines describing the CSDs of Fig. 5.3 and 5.5. Data are divided by the technique of data acquisition (FESEM-CL, FESEM-EBSD, mid-angle FESEM-BSE). The slope of the best-fit line corresponds to the two-dimensional fractal dimension D. D^* is the three-dimensional fractal dimension. Values of fracture surface energy U_S are in bold.

FESEM-CL: r_{min} = 5.406 μm, r_{max} = 29.078 μm

C = 6000, D = 2.10

	$D^* = 2.10$	$D^* = 3.10$
A_{SZi} (m^2)	2.07 10^{-7}	2.80 10^{-8}
V_{SZi} (m^3)	9.50 10^{-13}	1.02 10^{-13}
N	7.37 10^9	6.87 10^{10}
A_{SZ} (m^2)	1.53 10^3	1.92 10^3
U_S (MJ/m^2)	**0.015**	**0.019**

C = 10400, D = 2.99

	$D^* = 2.99$	$D^* = 3.99$
A_{SZi} (m^2)	6.02 10^{-8}	8.80 10^{-9}
V_{SZi} (m^3)	2.25 10^{-13}	2.68 10^{-14}
N	3.11 10^{10}	2.61 10^{11}
A_{SZ} (m^2)	1.88 10^3	2.30 10^3
U_S (MJ/m^2)	**0.019**	**0.023**

FESEM-EBSD: r_{min} = 0.448 μm, r_{max} = 105.071 μm

C = 30000, D = 1.83

	$D^* = 1.83$	$D^* = 2.83$
A_{SZi} (m^2)	5.41 10^{-6}	2.48 10^{-6}
V_{SZi} (m^3)	4.55 10^{-11}	2.79 10^{-12}
N	1.54 10^8	2.51 10^9
A_{SZ} (m^2)	8.33 10^2	6.21 10^3
U_S (MJ/m^2)	**0.008**	**0.062**

FESEM-BSE: r_{min} = 0.047 μm, r_{max} = 0.976 μm

C = 300, D = 1.10

	$D^* = 1.10$	$D^* = 2.10$
A_{SZi} (m^2)	4.21 10^{-9}	2.81
V_{SZi} (m^3)	6.93 10^{-16}	2.68
N	1.01 10^{13}	2.61
A_{SZ} (m^2)	4.26 10^{-4}	7.34
U_S (MJ/m^2)	**0.43**	**0.73**

C = 2000, D = 1.94

	$D^* = 1.94$	$D^* = 2.94$
A_{SZi} (m^2)	1.35 10^{-7}	1.31 10^{-6}
V_{SZi} (m^3)	1.43 10^{-14}	6.82 10^{-14}
N	4.88 10^{11}	1.03 10^{11}
A_{SZ} (m^2)	6.59 10^4	1.35 10^5
U_S (MJ/m^2)	**0.66**	**1.35**

The fracture surface energy values U_S obtained range from 0.008-0.062 MJ m^{-2} for the FESEM-EBSD data, to 0.015-0.019 MJ m^{-2} and 0.019-0.023 MJ m^{-2} for FESEM-CL, to 0.43-0.73 MJ m^{-2} and 0.66-1.35 MJ m^{-2} for mid-angle FESEM-BSE. The surface energies obtained from FESEM-CL and FESEM-EBSD investigations of the micro-domains are comparable, and this is consistent with the fact that they sample the same grainsize interval. The highest values of surface energy are estimated from the CSD curve obtained from the mid-angle FESEM-BSE imaging, as expected. In fact, for a given bulk volume occupied by particles, the total surface of the particles is higher if these are smaller. The obtained values of U_S in the slip zone are in agreement with those calculated by Pittarello et al. (2008), ranging 0.10-0.85 MJ m^{-2} (see also Fig. 5.4).

5.4 Earthquake energy budget

The other quantity to account for in the estimate of the mechanical work is the heat per unit fault area Q (Eq. 5.2). This can be calculated with (Di Toro, Pennacchioni, et al., 2005):

$$Q = \left[H(1 - \phi) + c_p(T_m - T_{hr}) \right] \rho w \quad \left({}^{J}\!/_{m^2} \right) \quad \text{Eq. 5.9}$$

with (reported values are for tonalites and pseudotachylytes of the GLFZ) H the latent heat of fusion (3.32 10^5 J kg^{-1}, Di Toro and Pennacchioni, 2004), ϕ the volume ratio between the residual clasts in the frictional melt and the pseudotachylyte matrix (0.2, Di Toro and Pennacchioni, 2004), c_p the isobaric specific heat (1200 J kg^{-1} K^{-1}, Di Toro and Pennacchioni, 2004), T_m the maximum temperature of the melt (1450°C, Di Toro and Pennacchioni, 2004), T_{hr} the temperature of the host rock during the seismic event (250°C, Di Toro and Pennacchioni, 2004), ρ the density of tonalite (2700 kg m^{-3}, Philpotts, 1990) and w the mean thickness of the pseudotachylyte vein (7 mm, Griffith et al., 2010). Based on Eq. 5.9, the value of Q is ~ 32 MJ m^{-2}. Again the result is comparable to the one obtained by Pittarello et al. (2008), 27 MJ m^{-2}.

Even if the obtained values of fracture surface energy U_S are possibly overestimated (i.e., considering the specific surface energy of plagioclase and examining the highest value interval coming from mid-angle FESEM-BSE grainsize data) their values are still very low compared to the energy dissipated in frictional heating Q (0.66-1.35 MJ m^{-2} vs. 32 MJ m^{-2}).

Surface energy U_S constitutes ~ 4 % of the energy dissipated into heat, so according to Eq. 5.2 the mechanical work can be approximated as:

$$E_f \approx Q$$

This means that in moderate magnitude earthquakes in the continental crust most of the mechanical work is dissipated as heat (Pittarello et al., 2008; Cocco et al., 2023).

Both values of U_S and Q obtained in the present thesis are consistent to those of Pittarello et al. (2008) and in general with those obtained in other works estimating the surface energy from geological evidences (red arrows in Fig. 5.6). However, in this thesis I investigated in detail the microfracture pattern also in the wall rocks and, thanks to the FESEM-CL investigation, I detected a dense network of microfractures that could not be detected with other techniques, or were largely underestimated (e.g., fluid inclusion trails, Griffith et al., 2010). Still, the contribution of this microfracture network and the density of the microfractures drastically reduces just few millimetres far away from the fault (Fig. 4.12).

The estimates of U_S from the literature cover a wide range of values (0.03 – 100 MJ m^{-2}, see Fig. 5.6), because of the uncertainty given by the many factors that influence the results of the calculations, such as (1) the difficulty to determine the number of seismic events hosed by the fault, (2) the fault structures and its heterogeneities and more in general the characteristics of the fault zone, (3) the influence of healing and sealing processes, etc. (Johnson et al., 2021; Cocco et al., 2023). Moreover, the energy balance of an earthquake based on geological approaches cannot consider the energy dissipated by seismic waves (the radiated energy). This goes to the relation between the seismic fracture energy G', obtained by seismological means (Abercrombie & Rice, 2005; Tinti et al., 2005) and U_S.

Seismic fracture energy G' is the energy dissipated during the propagation of the rupture (also called breakdown work) (Abercrombie & Rice, 2005; Tinti et al., 2005; Scholz, 2019; Cocco et al., 2023). According to Linear Elastic Fracture Mechanics (LEFM, Griffith, 1921) fracture energy G is a material property, so it should be independent of slip distance. Instead, G' depends on the constitutive law adopted to describe the seismic process and is represented by the area (i.e., a triangle) comprised between the shear stress curve and the residual stress (Fig. 1.4). In this framework, G' scales with seismic slip (and thus earthquake moment magnitude). This scaling relation is evident both from seismological and laboratory studies (Nielsen et al., 2016; Cocco et al., 2023) (Fig. 1.5). Still, due to the differences in the

results obtained with these methods, the true physical meaning of G' is unclear (Cocco et al., 2023). Di Toro et al. (2005) by using a slip weakening law in numerical models of seismic ruptures of M_w $6-7$ earthquakes and propagating along the GLFZ, estimated G' values ranging between $8-67$ MJ m^{-2}. Clearly, the surface energy U_S estimated in the present thesis (0.66-1.35 MJ m^{-2}) is only a fraction of G'. Instead, the estimated G' is in the range of Q values (32 MJ m^{-2}). It arises that fracture energy G' includes the contribution of the "geological" fracture surface energy U_S and, to a much large extent, frictional heat Q (compare Fig. 1.4 with Fig. 5.6). In other words, U_S is in practice unrelated to G' because U_S includes only the energy dissipated in fracturing processes.
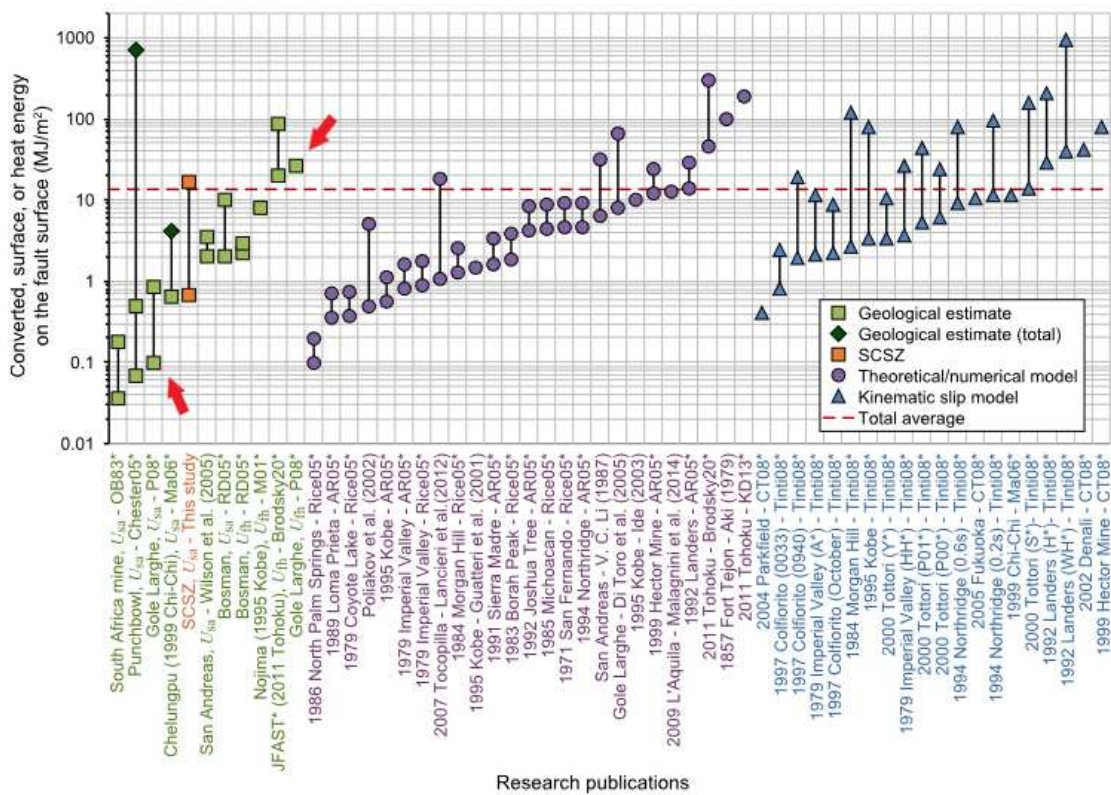
Fig. 5.6 Estimates of surface energy U_S, converted energy and heat energy from different works. Approaches are divided into geological estimates (green and orange data), theoretical estimates (purple data) and from inversion of ground motion waveforms (blue data). The data of this thesis overlap with the ones estimated by Pittarello et al. (2008) (red arrows). Modified from Johnson et al. (2021).

6. Conclusion and future work

The total energy budget involved in an earthquake is still not known, and the same is valid for its partitioning into the various energy sinks during a seismic event (see Chapter 1). Qualitatively, most of the elastic strain energy stored in the wall rocks and released during an earthquake goes into dissipation processes such as frictional heat and fracturing (without considering the energy radiated as seismic waves) (Scholz, 2019; Cocco et al., 2023). Estimates of these radiated energies, frictional heat, etc. can be done with seismological, experimental and geological approaches, to better understand earthquake mechanics. The geological approach can rely on the analysis of the wall rock damage associated with pseudotachylyte-bearing faults, extensively recognized as evidences of past earthquakes preserved in the rock record (Sibson, 1975). Fault exposures that allow the estimates of earthquake source parameters such as fault offset, rupture length, etc. have already been employed in literature to constrain the energy dissipated both in fracture process (Chester et al., 2005) and, if pseudotachylytes are present, frictional heat (Pittarello et al., 2008). The well-exposed outcrops of the Gole Larghe Fault Zone offer a great opportunity to estimate both fracture surface energy U_S and frictional heat Q.

For this reason, in the present thesis microstructural analysis of four thin sections of a natural pseudotachylyte-bearing fault of the GLFZ (Adamello batholith, Italy, Fig. 2.1) and one thin section of an experimental pseudotachylyte obtained from the same host rock of the natural case (Fig. 4.4) was carried out with FESEM techniques. Thanks to the utilization of the FESEM-CL, FESEM-EBSD and mid-angle FESEM-BSE techniques, the analysis of the microfractures over a ~ 2 cm thickness around the natural fault, and at the contact with the experimental pseudotachylyte, evidenced on both sides:

- In the natural fault, extreme fragmentation in the wall rock at the contact with the pseudotachylyte fault vein and at the tip of the injection veins (Fig. 4.5, 4.11);
- In the natural fault, a systematic difference in the orientation of the microfractures in the northern (mainly striking E-W) and southern (mainly striking N-S) wall rocks, and in microfracture density (higher in the southern wall rock) (Fig. 4.13, 4.14);
- In the natural fault, a rapid decrease of the microfracture density moving from the pseudotachylyte-bearing fault towards the wall rocks (Fig. 4.9, 4.10);

· In the experimental fault, the absence of a neat asymmetric distribution of the microfractures and, compared to the natural fault, a much lower microfracture density (Fig. 4.20).

These microstructural evidences lead to the conclusion that:

· The microfractures in the natural pseudotachylyte are coseismic and formed by the transient stresses and dynamic loading associated with the rupture propagation;

· Most of the mechanical energy is dissipated within the fault slip zone and, to a less extent, in the first ~ 1 mm of thickness around it. Instead, the damage further away from the fault surface is significantly lower (both at the microscale and at the outcrop scale), and thus its contribution negligible for the estimate of the fracture surface energy U_S;

Because of the sharp decrease in microfracture density in the wall rocks, I determined the Clast Size Distributions in the micro-domains at the tip of a single injection vein next to the pseudotachylyte fault vein (Fig. 4.11). I assumed that these CSDs represent the grainsize resulting from seismic rupture propagation but survived from frictional melting. The CSDs curves can be described by one (the one obtained from FESEM-EBSD analysis) or at least two (these obtained from FESEM-CL and mid-angle FESEM-BSE analysis) best fit lines (Fig. 5.3). As a consequence, I estimated a range of fractal dimensions D and intercepts C from the CSDs (Table 5.1 and Fig. 5.5). Then, following Pittarello et al. (2008), form the CSDs I estimated the surface energy U_S (maximum values of $0.66 - 1.35$ MJ m^{-2}) associated with the earthquake produced by the selected fault (see Chapter 5.3). Comparison of U_S with the estimated frictional heat Q (32 MJ m^{-2}) dissipated by the fault and with seismological estimates of fracture energy G' (Chapter 5.4) yield the following conclusions:

· The largest contribution to U_S is from the smallest fragments (analysed through mid-angle FESEM-BSE);

· The geological estimates of the fracture surface energy U_S are negligible with respect to the energy dissipated as heat (~ 4 % of Q);

· The values of fracture surface energy U_S estimated with geological approaches are systematically lower than the values of G' calculated through experiments and seismological analysis.

The results obtained in the present thesis are consistent to the estimates of U_S made by Pittarello et al. (2008), though they employed different methods (FESEM-BSE), estimated the surface energy only for a single clast of plagioclase in the pseudotachylyte and did not detect the large density of microfractures in the wall rocks. Our results show that most of the mechanical work of continental crust earthquakes, at least at seismogenic depths (here 8 – 11 km), is dissipated as frictional heat. Also, surface energy U_S is likely not the same quantity as the seismologically-determined fracture energy G', but a small fraction of it.

The estimates of fracture surface energy U_S through the method adopted in the present work are sensible to the grainsize values obtained from the FESEM analysis. To obtain more accurate results, future analysis should include the investigation of the micro-domains with higher resolution techniques, such as Scanning Transmission Electron Microscopy (STEM), that would allow the recognition of smaller particles with respect to the present dataset. Another issue is the difference of the FESEM-CL and FESEM-EBSD Clast Size Distribution curves, that has not been fully understood. The two CSDs should follow the same power-law, but the EBSD technique does not distinguish two neighbour grains if their orientation mismatch is > 10°. Instead, FESEM-CL may not detect the microfracture if the sealing material has the same composition of the fragments.

References

Abercrombie, R. E., & Rice, J. R. (2005). Can observations of earthquake scaling constrain slip weakening? *Geophysical Journal International*, *162*(2), 406–424. https://doi.org/10.1111/j.1365-246X.2005.02579.x

Andrews, D. J. (1976). Rupture propagation with finite stress in antiplane strain. *Journal of Geophysical Research (1896-1977)*, *81*(20), 3575–3582. https://doi.org/10.1029/JB081i020p03575

Bachmann, F., Hielscher, R., & Schaeben, H. (2011). Grain detection from 2d and 3d EBSD data—Specification of the MTEX algorithm. *Ultramicroscopy*, *111*(12), 1720–1733. https://doi.org/10.1016/j.ultramic.2011.08.002

Ben-Zion, Y., Dresen, G. (2022). Fracture, friction and damage processes in earthquake rupture zones, PREPRINT (Version 1) available at *Research Square*. https://doi.org/10.21203/rs.3.rs-1861418/v1

Bestmann, M., & Pennacchioni, G. (2015). Ti distribution in quartz across a heterogeneous shear zone within a granodiorite: The effect of deformation mechanism and strain on Ti resetting. *Lithos*, *227*, 37–56. https://doi.org/10.1016/j.lithos.2015.03.009

Bestmann, M., Pennacchioni, G., Mostefaoui, S., Göken, M., & de Wall, H. (2016). Instantaneous healing of micro-fractures during coseismic slip: Evidence from microstructure and Ti in quartz geochemistry within an exhumed pseudotachylyte-bearing fault in tonalite. *Lithos*, *254–255*, 84–93. https://doi.org/10.1016/j.lithos.2016.03.011

Bestmann, M., Pennacchioni, G., Nielsen, S., Göken, M., & de Wall, H. (2012). Deformation and ultrafine dynamic recrystallization of quartz in pseudotachylyte-bearing brittle faults: A matter of a few seconds. *Journal of Structural Geology*, *38*, 21–38. https://doi.org/10.1016/j.jsg.2011.10.001

Brace, W. F., & Walsh, J. B. (1962). Some direct measurements of the surface energy of quartz and orthoclase. *American Mineralogist*, *47*(9–10), 1111–1122.

Callegari, E., & Brack, P. (2002). Geological map of the Tertiary Adamello batholith (northern Italy): Explanatory notes and legend. *Memorie di Scienze Geologiche*, *54*, 19-49.

Chester, J. S., Chester, F. M., & Kronenberg, A. K. (2005). Fracture surface energy of the Punchbowl fault, San Andreas system. *Nature*, *437*(7055), Article 7055. https://doi.org/10.1038/nature03942

Cocco, M., Aretusini, S., Cornelio, C., Nielsen, S. B., Spagnuolo, E., Tinti, E., & Di Toro, G. (2023). Fracture Energy and Breakdown Work During Earthquakes. *Annual Review of Earth and Planetary Sciences*, *51*(1), null. https://doi.org/10.1146/annurev-earth-071822-100304

Cocco, M., Spudich, P., & Tinti, E. (2006). *On the mechanical work absorbed on faults during earthquake ruptures*. AGU. https://www.earth-prints.org/handle/2122/2290

Cowan, D. S., 1999. Do faults preserve a record of seismic slip? A field geologist's opinion. *Journal of Structural Geology* 21, 995–1001.

Del Moro, A., Pardini, G., Quercioli, C., Villa, I. M., & Callegari, E. (1983). Rb/Sr and K/Ar chronology of Adamello granitoids, southern Alps. *Memorie Della Societa Geologica Italiana*, *26*(1), 285–299.

Dempsey, E. D., Holdsworth, R. E., Imber, J., Bistacchi, A., & Di Toro, G. (2014). A geological explanation for intraplate earthquake clustering complexity: The zeolite-bearing fault/fracture networks in the Adamello Massif (Southern Italian Alps). *Journal of Structural Geology*, *66*, 58–74. https://doi.org/10.1016/j.jsg.2014.04.009

Di Toro, G., Hirose, T., Nielsen, S., Pennacchioni, G., & Shimamoto, T. (2006). Natural and Experimental Evidence of Melt Lubrication of Faults During Earthquakes. *Science*, *311*(5761), 647–649. https://doi.org/10.1126/science.1121012

Di Toro, G., Nielsen, S., & Pennacchioni, G. (2005a). Earthquake rupture dynamics frozen in exhumed ancient faults. *Nature*, *436*(7053), Article 7053. https://doi.org/10.1038/nature03910

Di Toro, G., & Pennacchioni, G. (2004). Superheated friction-induced melts in zoned pseudotachylytes within the Adamello tonalites (Italian Southern Alps). *Journal of Structural Geology*, *26*(10), 1783–1801. https://doi.org/10.1016/j.jsg.2004.03.001

Di Toro, G., & Pennacchioni, G. (2005). Fault plane processes and mesoscopic structure of a strong-type seismogenic fault in tonalites (Adamello batholith, Southern Alps). *Tectonophysics*, *402*(1), 55–80. https://doi.org/10.1016/j.tecto.2004.12.036

Di Toro, G., Pennacchioni, G., & Nielsen, S. (2009). Pseudotachylytes and Earthquake Source Mechanics. In *International Geophysics* (Vol. 94, pp. 87–133). Academic Press. https://doi.org/10.1016/S0074-6142(08)00005-3

Di Toro, G., Pennacchioni, G., & Nielsen, S. (2009). Pseudotachylytes and earthquake source mechanics. *International Geophysics*, *94*(C), 87–133. Scopus. https://doi.org/10.1016/S0074-6142(08)00005-3

Di Toro, G., Pennacchioni, G., & Teza, G. (2005b). Can pseudotachylytes be used to infer earthquake source parameters? An example of limitations in the study of exhumed faults. *Tectonophysics*, *402*(1), 3–20. https://doi.org/10.1016/j.tecto.2004.10.014

Fondriest, M., Balsamo, F., Bistacchi, A., Clemenzi, L., Demurtas, M., Storti, F., & Di Toro, G. (2020a). Structural Complexity and Mechanics of a Shallow Crustal Seismogenic Source (Vado di Corno Fault Zone, Italy). *Journal of Geophysical Research: Solid Earth*, *125*(9), e2019JB018926. https://doi.org/10.1029/2019JB018926

Fondriest, M., Mecklenburgh, J., Passelegue, F. X., Artioli, G., Nestola, F., Spagnuolo, E., Rempe, M., & Di Toro, G. (2020b). Pseudotachylyte Alteration and the Rapid Fade of Earthquake Scars From the Geological Record. *Geophysical Research Letters*, *47*(22), e2020GL090020. https://doi.org/10.1029/2020GL090020

Gomila, R., Fondriest, M., Jensen, E., Spagnuolo, E., Masoch, S., Mitchell, T. M., Magnarini, G., Bistacchi, A., Mittempergher, S., Faulkner, D., Cembrano, J., & Di Toro, G. (2021). Frictional Melting in Hydrothermal Fluid-Rich Faults: Field and Experimental Evidence From the Bolfín Fault Zone (Chile). *Geochemistry, Geophysics, Geosystems*, *22*(7), e2021GC009743. https://doi.org/10.1029/2021GC009743

Griffith, A. A. (1921). *VI. The phenomena of rupture and flow in solids | Philosophical Transactions of the Royal Society of London. Series A, Containing Papers of a Mathematical or Physical Character.* https://royalsocietypublishing.org/doi/abs/10.1098/rsta.1921.0006

Griffith, W. A., Mitchell, T. M., Renner, J., & Di Toro, G. (2012). Coseismic damage and softening of fault rocks at seismogenic depths. *Earth and Planetary Science Letters*, *353–354*, 219–230. https://doi.org/10.1016/j.epsl.2012.08.013

Griffith, W. A., Nielsen, S., Di Toro, G., & Smith, S. A. F. (2010). Rough faults, distributed weakening, and off-fault deformation. *Journal of Geophysical Research: Solid Earth*, *115*(B8). https://doi.org/10.1029/2009JB006925

Griffith, W. A., Rosakis, A. J., Pollard, D. D., & Ko, C. (2008). *Tensile cracks: A new link between geological observations of faults and seismological models of earthquake dynamics. 2008*, T22A-05.

Griffith, W. A., Rosakis, A., Pollard, D. D., & Ko, C. W. (2009). Dynamic rupture experiments elucidate tensile crack development during propagating earthquake ruptures. *Geology*, *37*(9), 795–798. https://doi.org/10.1130/G30064A.1

Hirose, T., & Shimamoto, T. (2005). Growth of molten zone as a mechanism of slip weakening of simulated faults in gabbro during frictional melting. *Journal of Geophysical Research: Solid Earth*, *110*(B5). https://doi.org/10.1029/2004JB003207

Ida, Y. (1972). Cohesive force across the tip of a longitudinal-shear crack and Griffith's specific surface energy. *Journal of Geophysical Research (1896-1977)*, *77*(20), 3796–3805. https://doi.org/10.1029/JB077i020p03796

Johnson, S. E., Song, W. J., Vel, S. S., Song, B. R., & Gerbi, C. C. (2021). Energy Partitioning, Dynamic Fragmentation, and Off-Fault Damage in the Earthquake Source Volume. *Journal of Geophysical Research: Solid Earth*, *126*(11), e2021JB022616. https://doi.org/10.1029/2021JB022616

Lazari, F., Castagna, A., Nielsen, S., Griffith, A., Pennacchioni, G., Gomila, R., Resor, P., Cornelio, C., & Di Toro, G. (2023). Frictional power dissipation in a seismic ancient

fault. *Earth and Planetary Science Letters*, *607*, 118057. https://doi.org/10.1016/j.epsl.2023.118057

Mandelbrot, B.B. (1977). Fractals: Form, Chance, and Dimension. San Francisco: W. H. Freeman.

McKenzie, D., & Brune, J. N. (1972). Melting on Fault Planes During Large Earthquakes. *Geophysical Journal International*, *29*(1), 65–78. https://doi.org/10.1111/j.1365-246X.1972.tb06152.x

Menegon, L., Campbell, L., Mancktelow, N., Camacho, A., Wex, S., Papa, S., Toffol, G., & Pennacchioni, G. (2021). The earthquake cycle in the dry lower continental crust: Insights from two deeply exhumed terranes (Musgrave Ranges, Australia and Lofoten, Norway). *Philosophical Transactions of the Royal Society A: Mathematical, Physical and Engineering Sciences*, *379*(2193), 20190416. https://doi.org/10.1098/rsta.2019.0416

Mitchell, T. M., Toy, V., Di Toro, G., Renner, J., & Sibson, R. H. (2016). Fault welding by pseudotachylyte formation. *Geology*, *44*(12), 1059–1062. https://doi.org/10.1130/G38373.1

Mittempergher, S., Zanchetta, S., Caldiroli, F., Zanchi, A., Bistacchi, A., Hanchar, J. M., & Villa, I. M. (2022). The timescale of solid-state deformation in the Northern Adamello igneous intrusive suite. *Journal of the Geological Society*, *179*(4), jgs2021-101. https://doi.org/10.1144/jgs2021-101

Nielsen, S., Spagnuolo, E., Smith, S. a. F., Violay, M., Di Toro, G., & Bistacchi, A. (2016). Scaling in natural and laboratory earthquakes. *Geophysical Research Letters*, *43*(4), 1504–1510. https://doi.org/10.1002/2015GL067490

O'Hara, K. (1992). Major- and trace-element constraints on the petrogenesis of a fault-related pseudotachylyte, western Blue Ridge province, North Carolina. *Tectonophysics*, *204*(3), 279–288. https://doi.org/10.1016/0040-1951(92)90312-T

Okubo, K., Bhat, H. S., Rougier, E., Marty, S., Schubnel, A., Lei, Z., Knight, E. E., & Klinger, Y. (2019). Dynamics, Radiation, and Overall Energy Budget of Earthquake Rupture With Coseismic Off-Fault Damage. *Journal of Geophysical Research: Solid Earth*, *124*(11), 11771–11801. https://doi.org/10.1029/2019JB017304

Palmer, A. C., & Rice, J. R. (1973). The growth of slip surfaces in the progressive failure of over-consolidated clay. *Proceedings of the Royal Society of London. A. Mathematical and Physical Sciences*. https://doi.org/10.1098/rspa.1973.0040

Passchier, C. W., & Trouw, R. A. J. (2005). *Microtectonics* (Second). Springer-Verlag. https://doi.org/10.1007/3-540-29359-0

Passelègue, François. X., Schubnel, A., Nielsen, S., Bhat, H. S., Deldicque, D., & Madariaga, R. (2016). Dynamic rupture processes inferred from laboratory microearthquakes. *Journal of Geophysical Research: Solid Earth*, *121*(6), 4343–4365. https://doi.org/10.1002/2015JB012694

Pennacchioni, G., Di Toro, G., Brack, P., Menegon, L., & Villa, I. M. (2006). Brittle–ductile–brittle deformation during cooling of tonalite (Adamello, Southern Italian Alps). *Tectonophysics*, *427*(1), 171–197. https://doi.org/10.1016/j.tecto.2006.05.019

Philpotts, A. R. (1990). Principles of igneous and metamorphic petrology Prentice Hall. *Englewood cliffs*.

Pittarello, L., Di Toro, G., Bizzarri, A., Pennacchioni, G., Hadizadeh, J., & Cocco, M. (2008). Energy partitioning during seismic slip in pseudotachylyte-bearing faults (Gole Larghe Fault, Adamello, Italy). *Earth and Planetary Science Letters*, *269*(1), 131–139. https://doi.org/10.1016/j.epsl.2008.01.052

Reid, H. F. (1910). The mechanism of the earthquake, the California earthquake of April 18, 1906. *Report of the Research Senatorial Commission, Carnegie Institution, Washington, DC*, *2*, 16-18.

Rowe, C. D., & Griffith, W. A. (2015). Do faults preserve a record of seismic slip: A second opinion. *Journal of Structural Geology*, *78*, 1–26. https://doi.org/10.1016/j.jsg.2015.06.006

Scambelluri, M., Pennacchioni, G., Gilio, M., Bestmann, M., Plümper, O., & Nestola, F. (2017). Fossil intermediate-depth earthquakes in subducting slabs linked to differential stress release. *Nature Geoscience*, *10*(12), Article 12. https://doi.org/10.1038/s41561-017-0010-7

Schaltegger, U., Nowak, A., Ulianov, A., Fisher, C. M., Gerdes, A., Spikings, R., Whitehouse, M. J., Bindeman, I., Hanchar, J. M., Duff, J., Vervoort, J. D., Sheldrake, T., Caricchi, L., Brack, P., & Müntener, O. (2019). Zircon Petrochronology and 40Ar/39Ar Thermochronology of the Adamello Intrusive Suite, N. Italy: Monitoring the Growth and Decay of an Incrementally Assembled Magmatic System. *Journal of Petrology*, *60*(4), 701–722. https://doi.org/10.1093/petrology/egz010

Scholz, C. H. (2019). *The Mechanics of Earthquakes and Faulting*. Cambridge University Press.

Schroeder, A. B., Dobson, E. T. A., Rueden, C. T., Tomancak, P., Jug, F., & Eliceiri, K. W. (2021). The ImageJ ecosystem: Open-source software for image visualization, processing, and analysis. *Protein Science*, *30*(1), 234–249. https://doi.org/10.1002/pro.3993

Shimamoto, T., and A. Tsutsumi, A new rotary-shear high-speed frictional testing machine: its basic design and scope of research (in Japanese with English abstract), *J. Tectonic Res. Group of Japan*, 39, 65-78, 1994

Sibson, R. H. (1975). Generation of Pseudotachylyte by Ancient Seismic Faulting. *Geophysical Journal International*, *43*(3), 775–794. https://doi.org/10.1111/j.1365-246X.1975.tb06195.x

Sibson, R. H. (1989). Earthquake faulting as a structural process. *Journal of Structural Geology*, *11*(1), 1–14. https://doi.org/10.1016/0191-8141(89)90032-1

Sibson, R. H., & Toy, V. G. (2006). The habitat of fault-generated pseudotachylyte: Presence vs. Absence of friction-melt. *Geophysical Monograph Series*, *170*. https://doi.org/10.1029/170GM16

Smith, S. A. F., Bistacchi, A., Mitchell, T. M., Mittempergher, S., & Di Toro, G. (2013). The structure of an exhumed intraplate seismogenic fault in crystalline basement. *Tectonophysics*, *599*, 29–44. https://doi.org/10.1016/j.tecto.2013.03.031

Spray, J. G. (1995). Pseudotachylyte controversy: Fact or friction? *Geology*, *23*(12), 1119–1122. https://doi.org/10.1130/0091-7613(1995)023<1119:PCFOF>2.3.CO;2

Spray, J. G. (2010). Frictional Melting Processes in Planetary Materials: From Hypervelocity Impact to Earthquakes. *Annual Review of Earth and Planetary Sciences*, *38*(1), 221–254. https://doi.org/10.1146/annurev.earth.031208.100045

Stipp, M., Stünitz, H., Heilbronner, R., & Schmid, S. M. (2002). The eastern Tonale fault zone: A 'natural laboratory' for crystal plastic deformation of quartz over a temperature range from 250 to 700°C. *Journal of Structural Geology*, *24*(12), 1861–1884. https://doi.org/10.1016/S0191-8141(02)00035-4

Swanson, M. T. (1992). Fault structure, wear mechanisms and rupture processes in pseudotachylyte generation. *Tectonophysics*, *204*(3), 223–242. https://doi.org/10.1016/0040-1951(92)90309-T

Techmer, K. S., Ahrendt, H., & Weber, K. (1992). The development of pseudotachylyte in the Ivrea—Verbano Zone of the Italian Alps. *Tectonophysics*, *204*(3), 307–322. https://doi.org/10.1016/0040-1951(92)90314-V

Tinti, E., Spudich, P., & Cocco, M. (2005). Earthquake fracture energy inferred from kinematic rupture models on extended faults. *Journal of Geophysical Research: Solid Earth*, *110*(B12). https://doi.org/10.1029/2005JB003644

Violay, M., Nielsen, S., Gibert, B., Spagnuolo, E., Cavallo, A., Azais, P., Vinciguerra, S., & Di Toro, G. (2014). Effect of water on the frictional behavior of cohesive rocks during earthquakes. *Geology*, *42*(1), 27–30. https://doi.org/10.1130/G34916.1

Wong, T. (1982). Shear fracture energy of Westerly granite from post-failure behavior. *Journal of Geophysical Research: Solid Earth*, *87*(B2), 990–1000. https://doi.org/10.1029/JB087iB02p00990

Yao, L., Ma, S., & Di Toro, G. (2023). Coseismic fault sealing and fluid pressurization during earthquakes. *Nature Communications*, *14*(1), Article 1. https://doi.org/10.1038/s41467-023-36839-9

Appendices

Appendix A
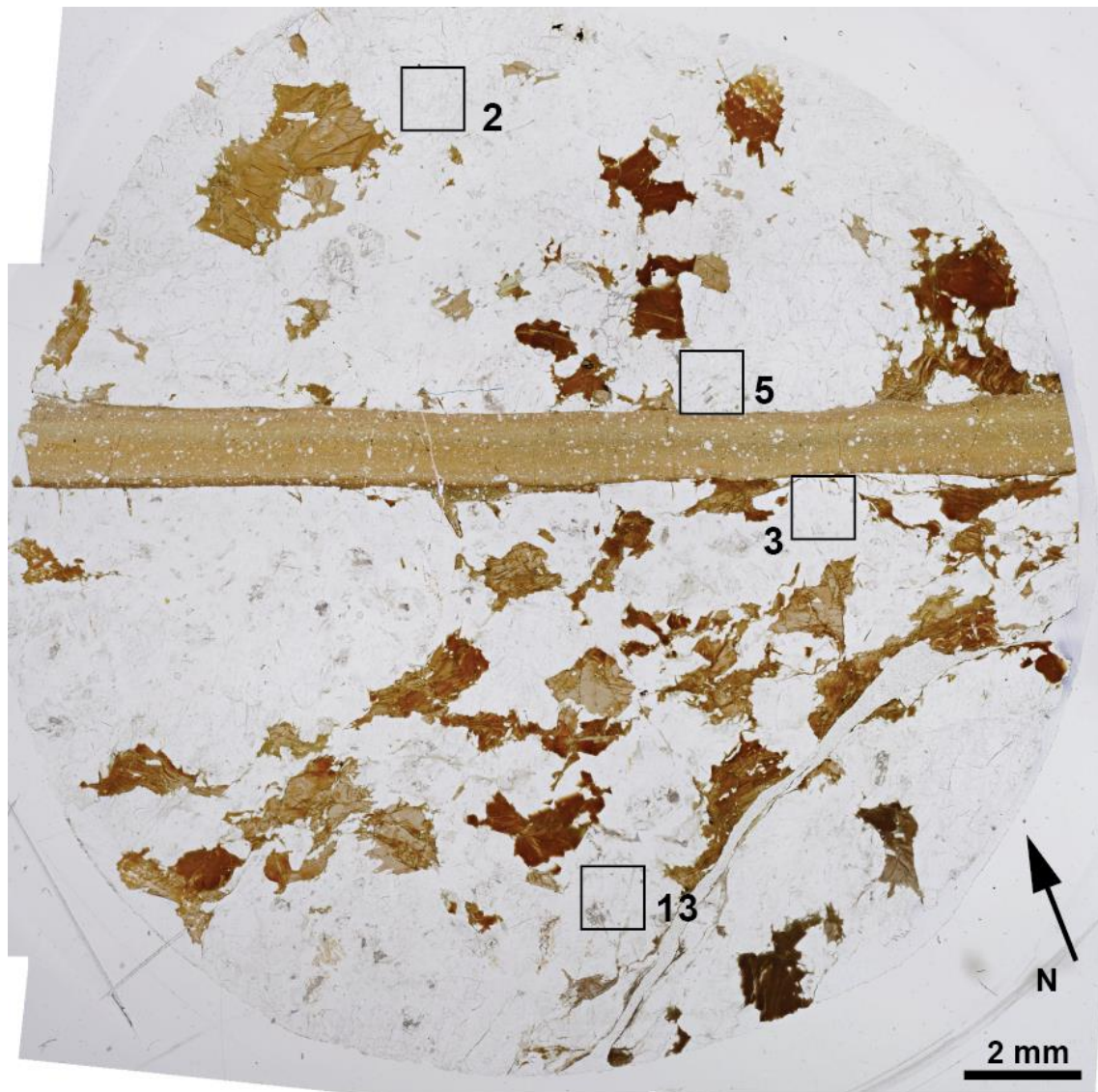
Fig. A.1 Scan of thin section L05-08 with location of the FESEM-CL microimages employed in the microfracture pattern characterization.

Fig. A.2 Scan of thin section WF22-01a with location of the FESEM-CL microimages employed in the microfracture pattern characterization.
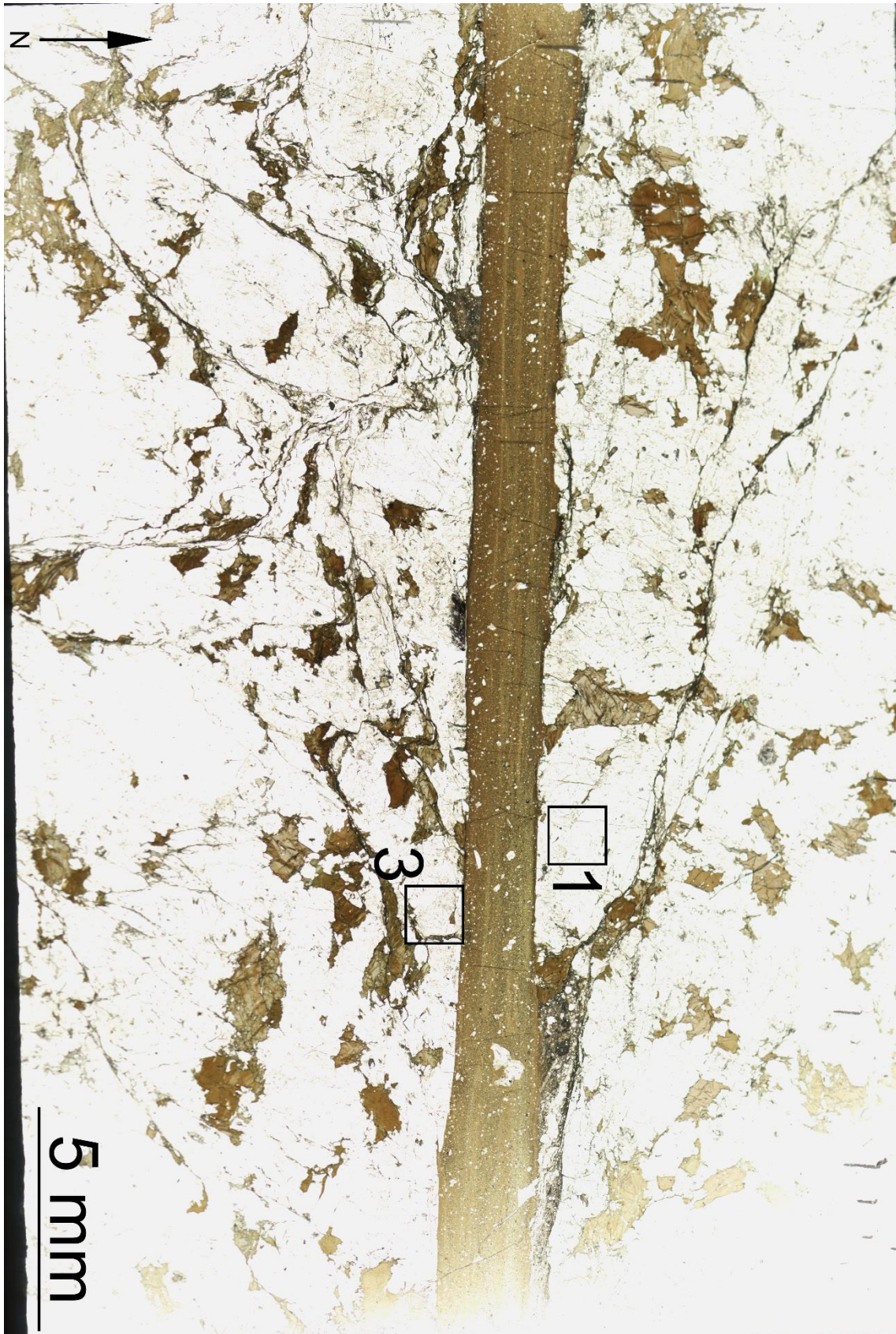
Fig. A.3 Scan of thin section WF22-01b with location of the FESEM-CL microimages employed in the microfracture pattern characterization.
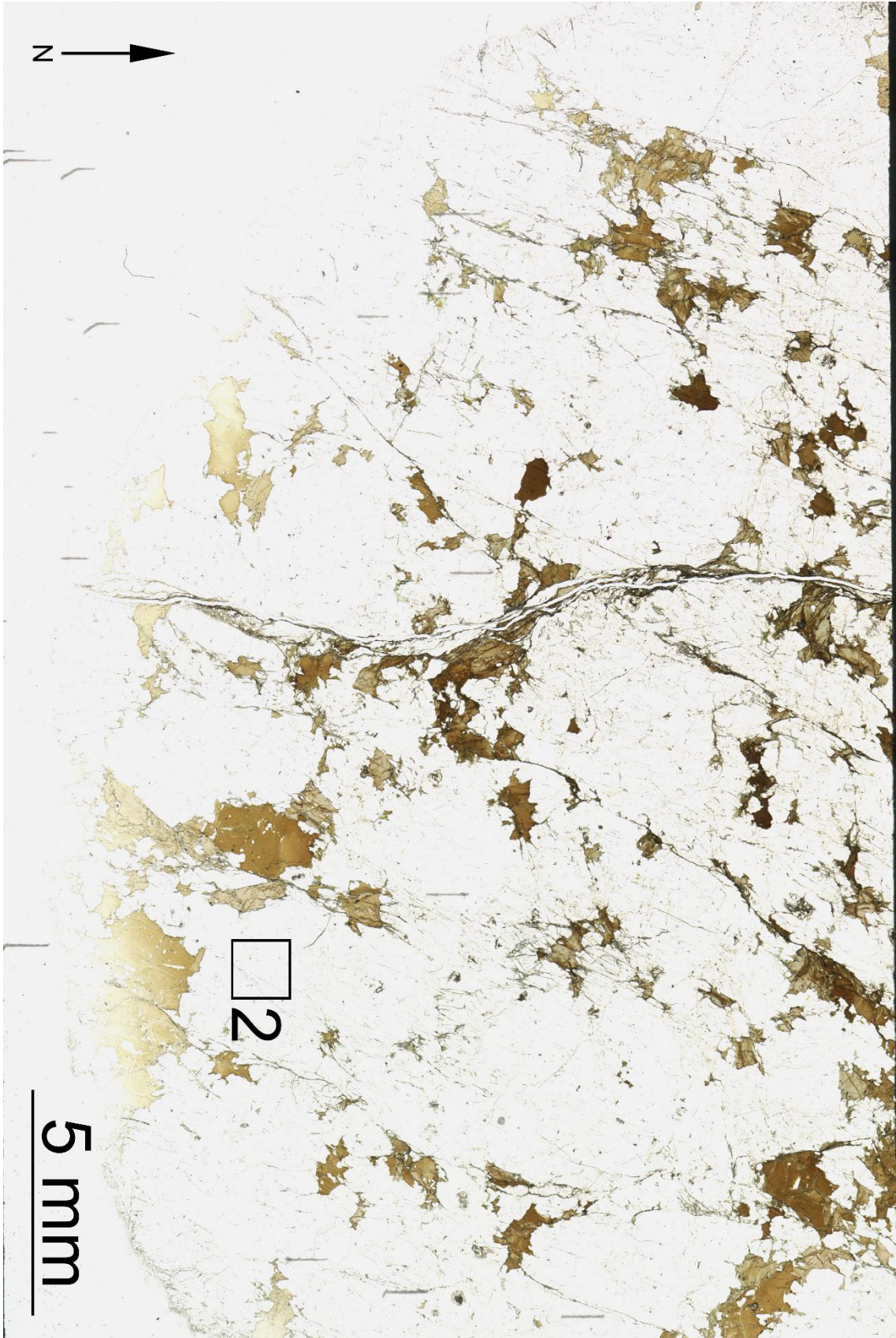
Fig. A.4 Scan of thin section WF22-01c with location of the FESEM-CL microimages employed in the microfracture pattern characterization.
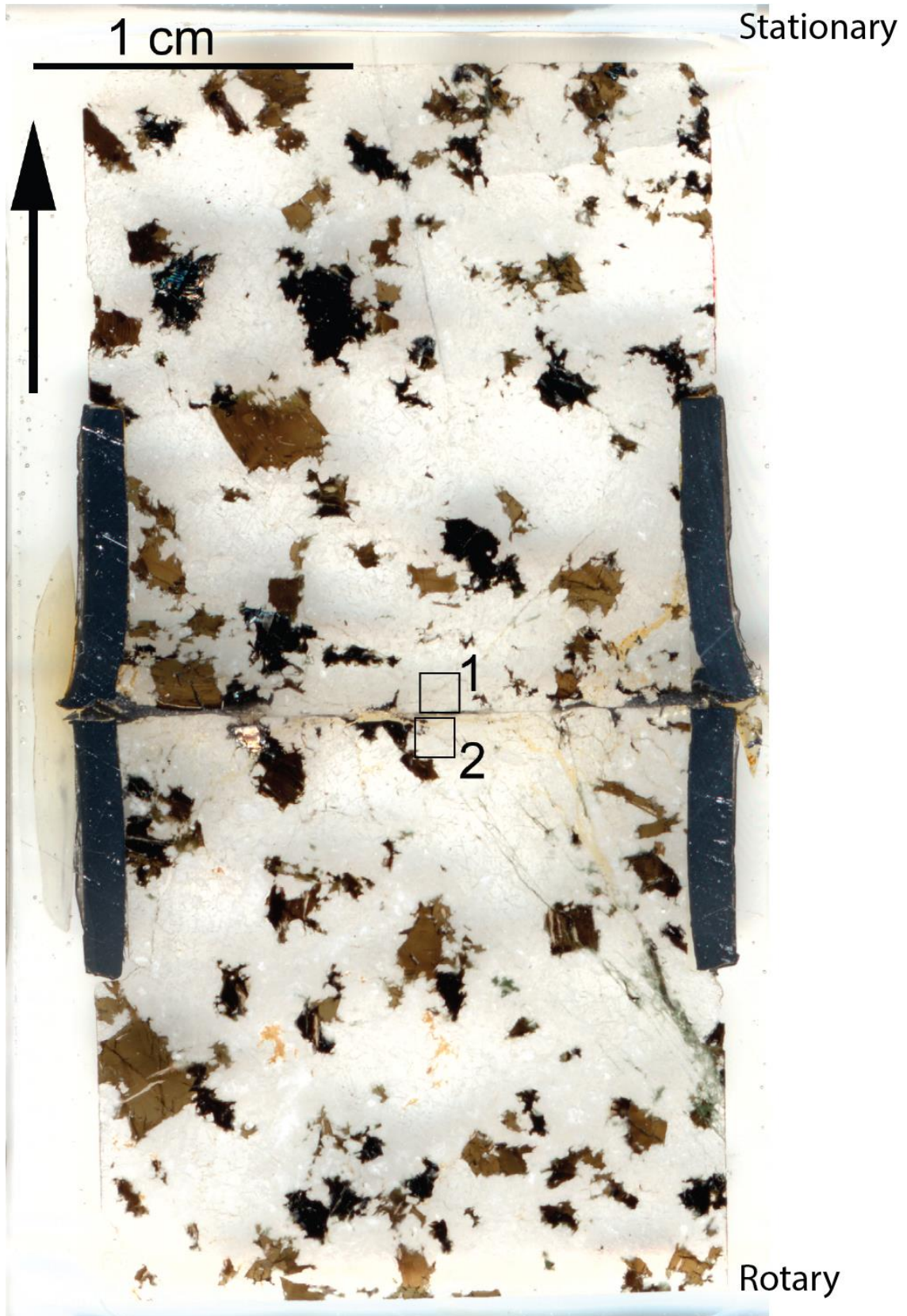
Fig. A.5 Scan of thin section HVR376 with location of the FESEM-CL microimages employed in the microfracture pattern characterization.
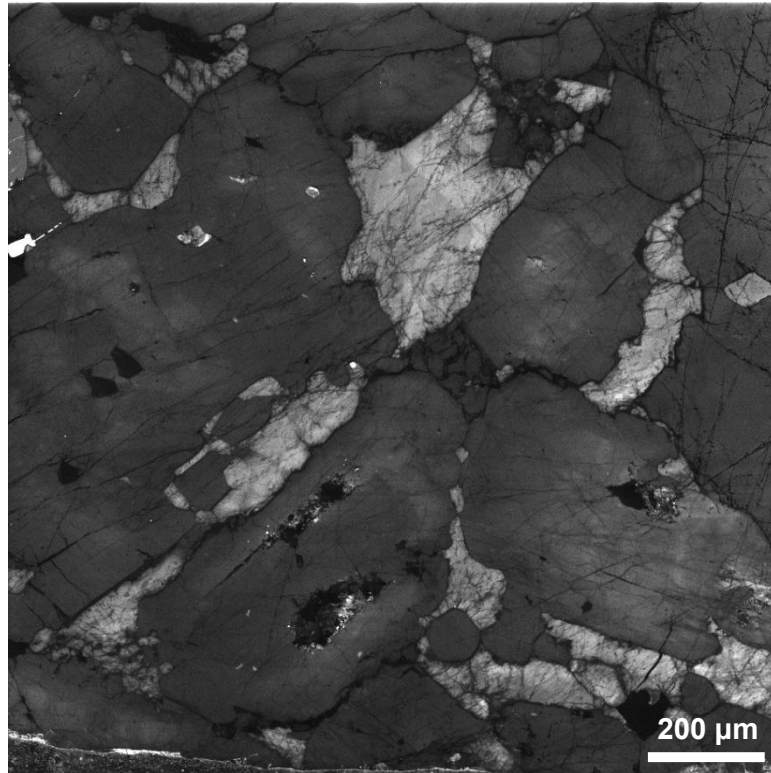
MATLAB® microfracture pattern
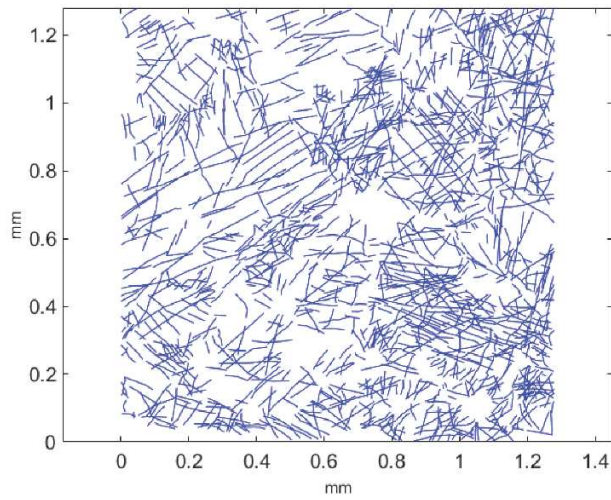
Frequency histogram
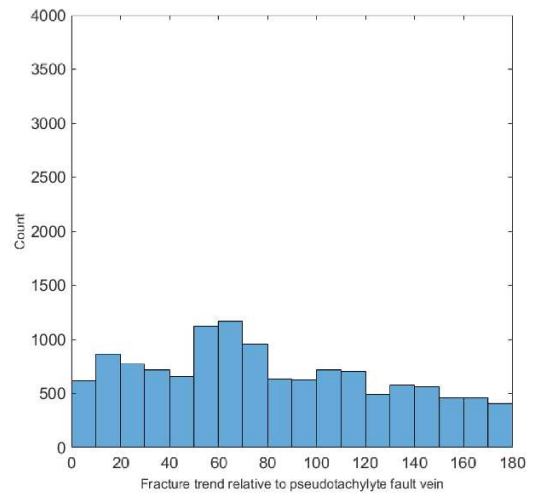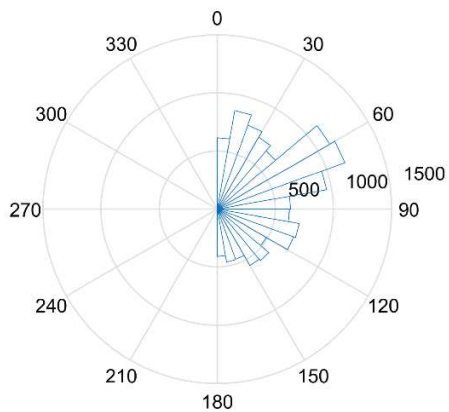
Rose diagram

Fig. A.6 FESEM-CL microimage L05-08 5. Northern wall rock, 0 mm from the pseudotachylyte fault vein.
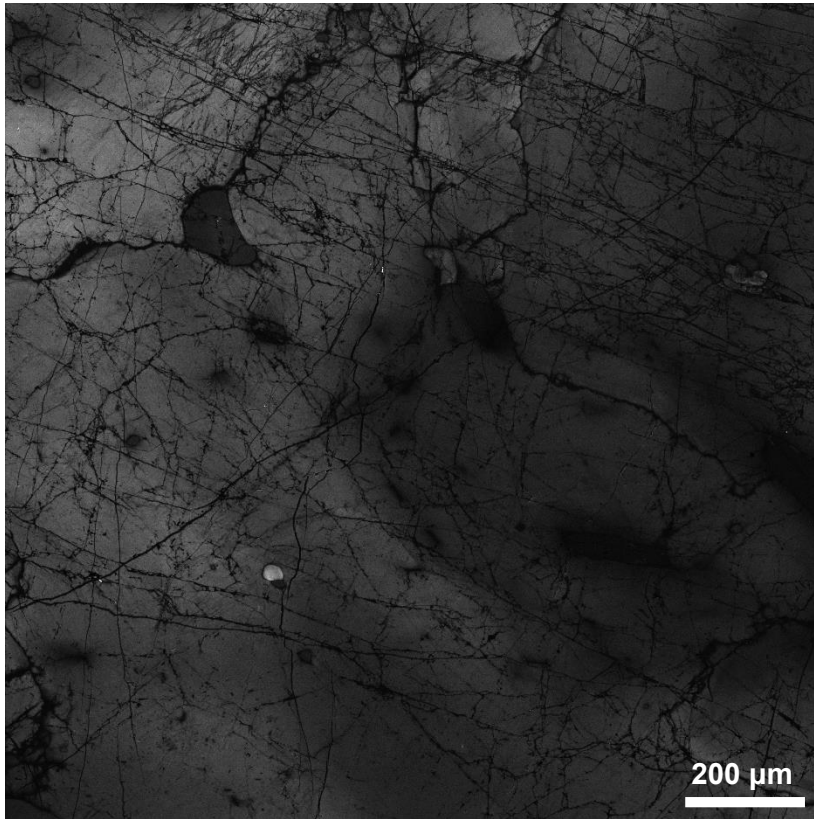
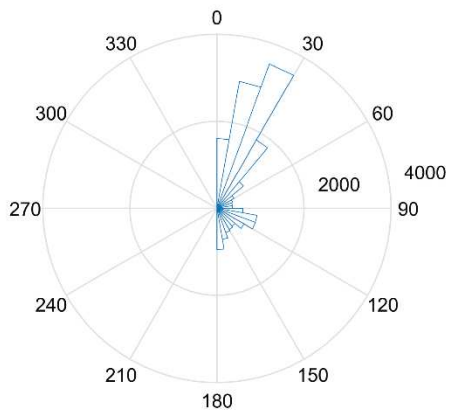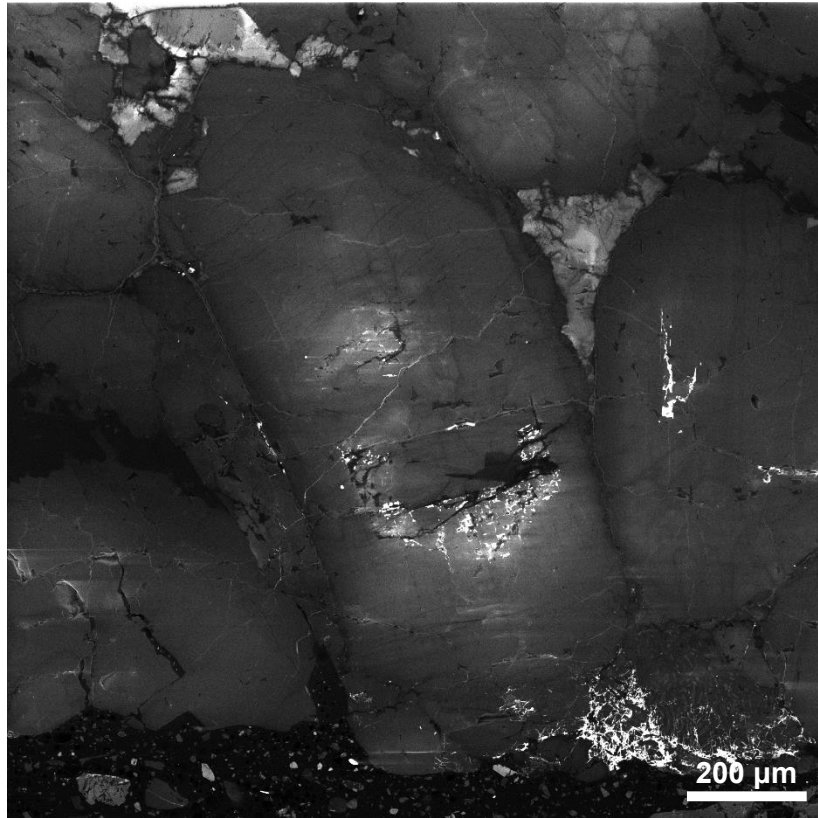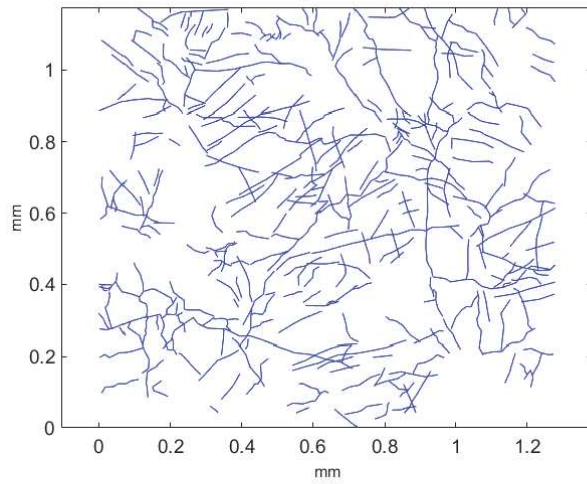MATLAB® microfracture pattern
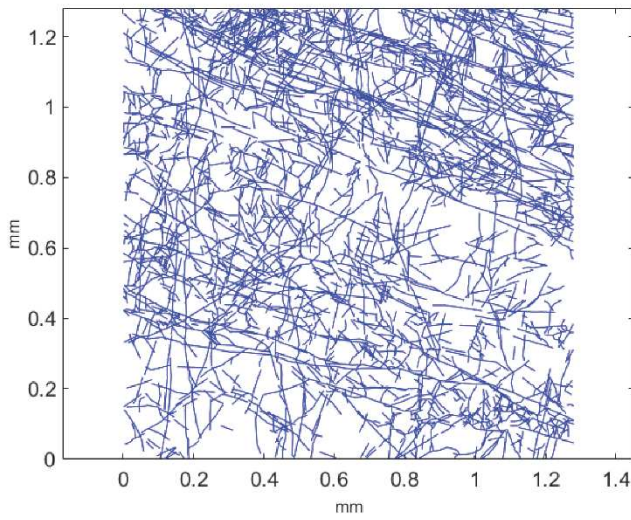
Frequency histogram
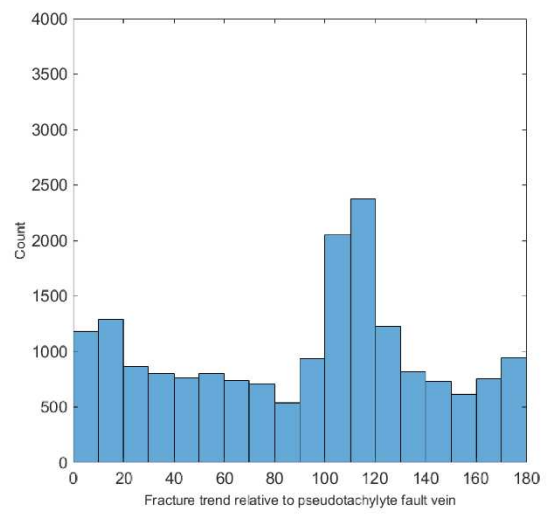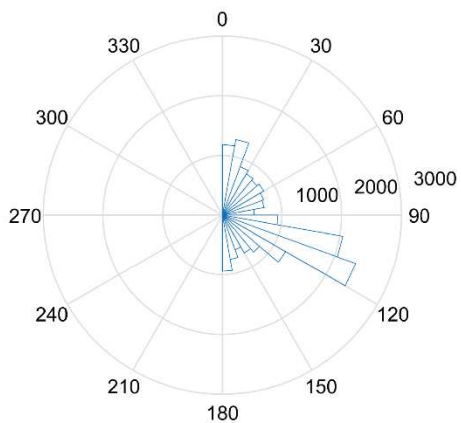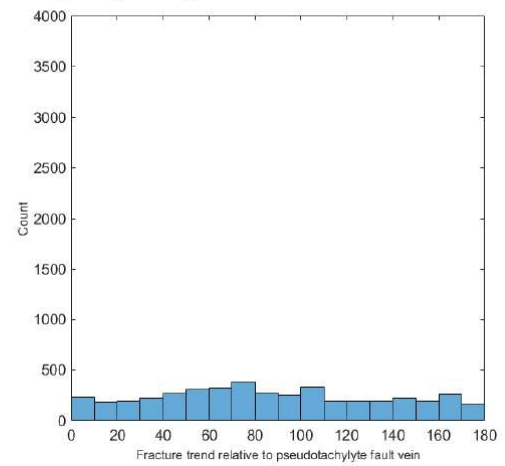

Rose diagram

Fig. A.7 FESEM-CL microimage WF22-01b 1. Northern wall rock, 0 mm from the pseudotachylyte fault vein.
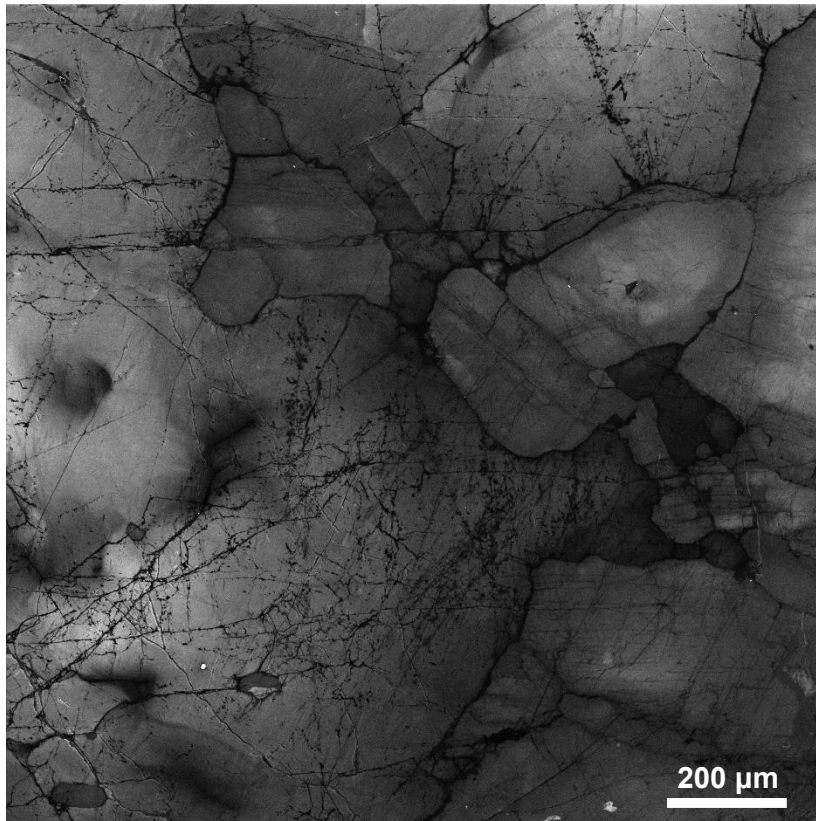
MATLAB® microfracture pattern
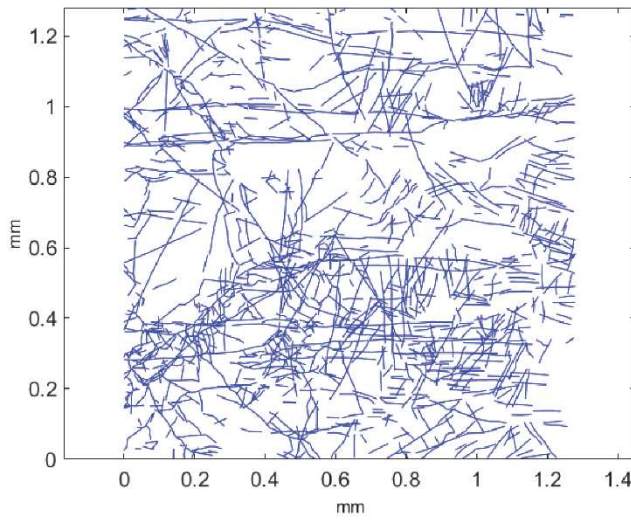
Frequency histogram
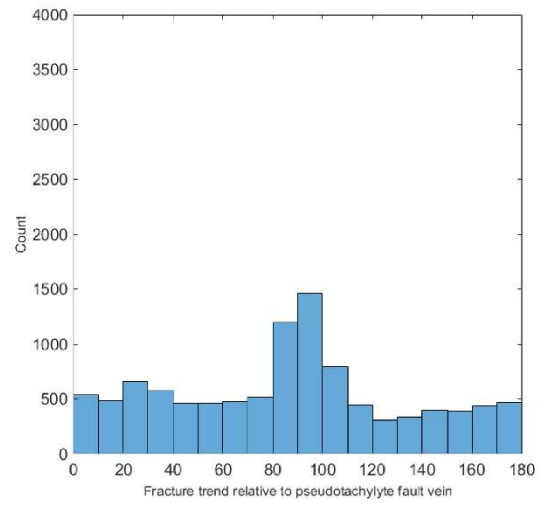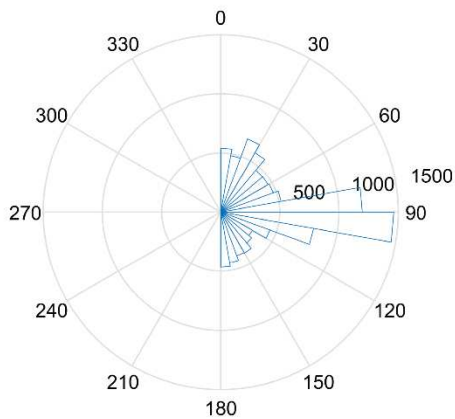
Rose diagram

Fig. A.8 FESEM-CL microimage L05-08 2. Northern wall rock, 5 mm from the pseudotachylyte fault vein.
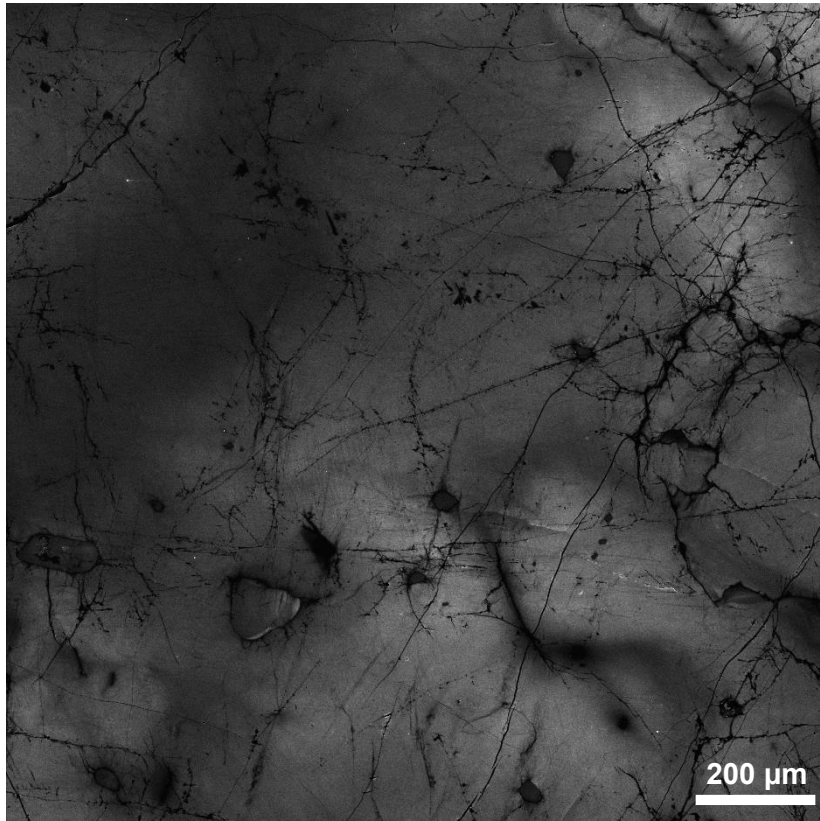
MATLAB® microfracture pattern
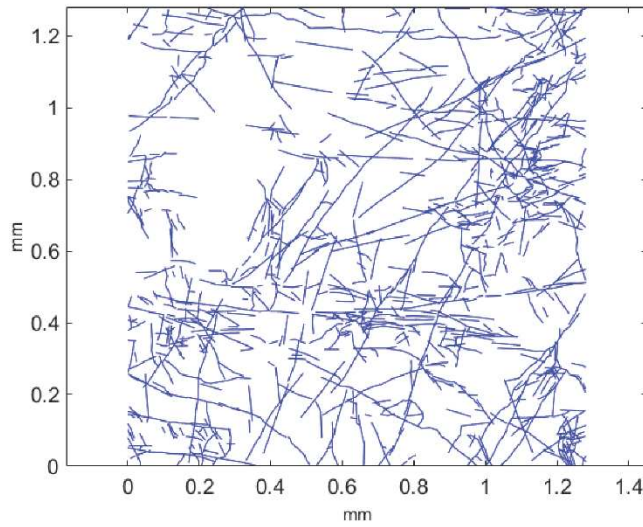
Frequency histogram
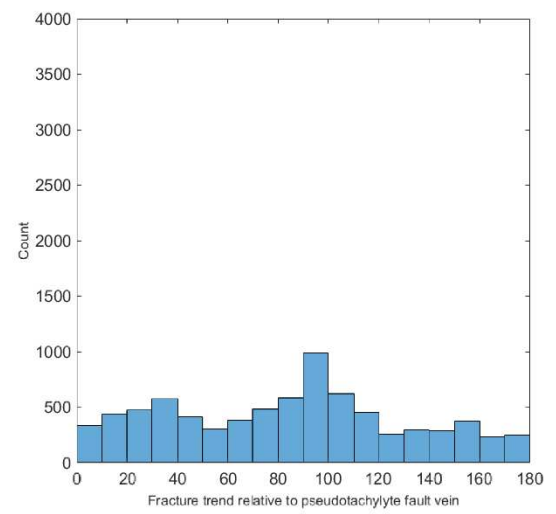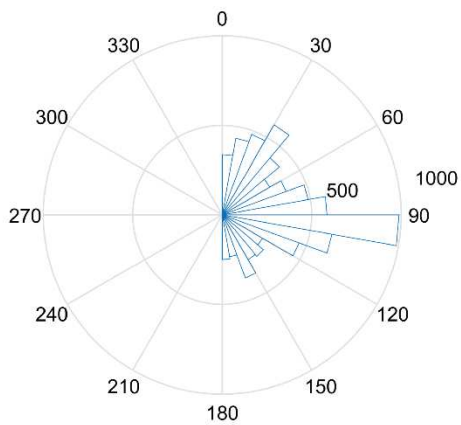
Rose diagram
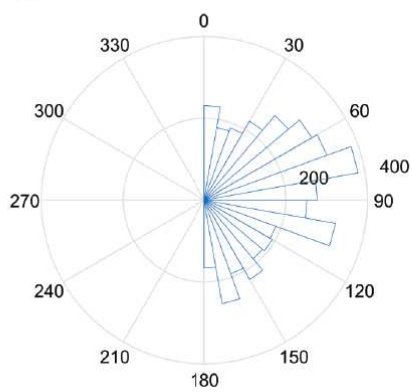

Fig. A.9 FESEM-CL microimage WF22-01a 2. Northern wall rock, 20 mm from the pseudotachylyte fault vein.

100

200 μm
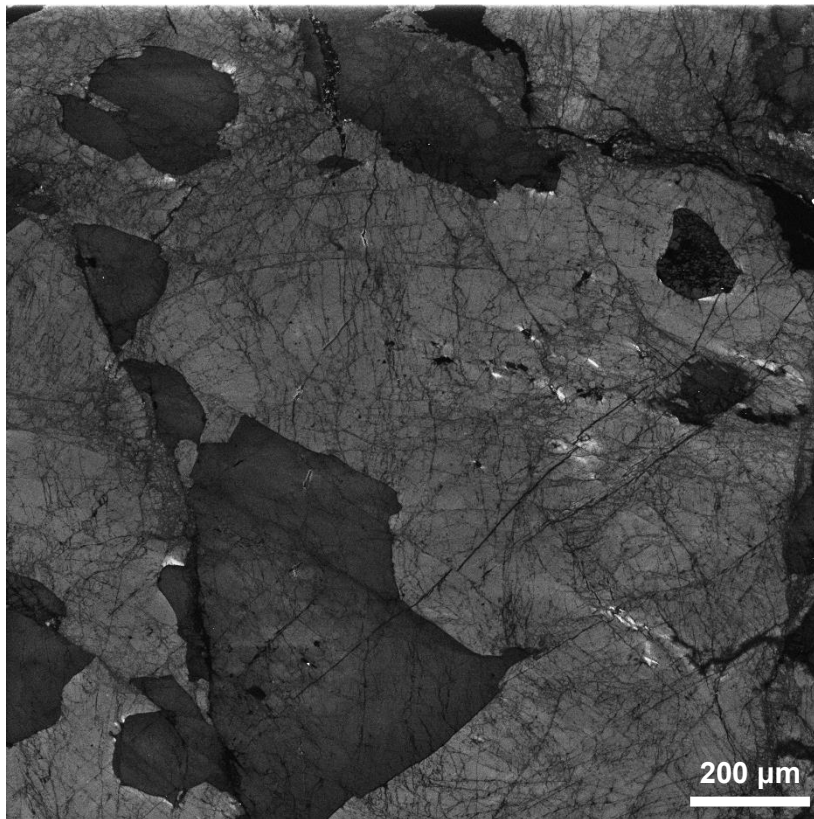
MATLAB® microfracture pattern
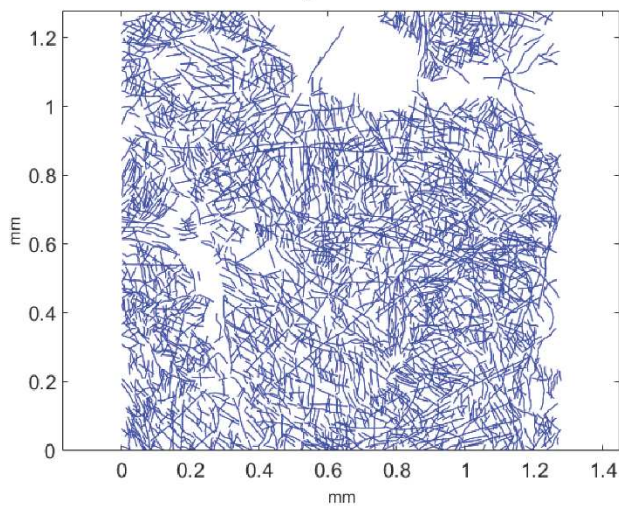
Frequency histogram
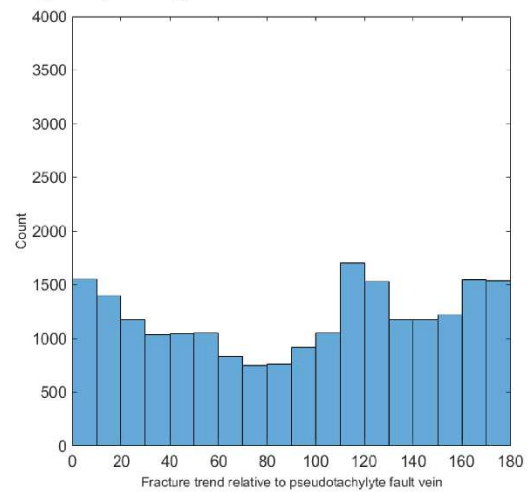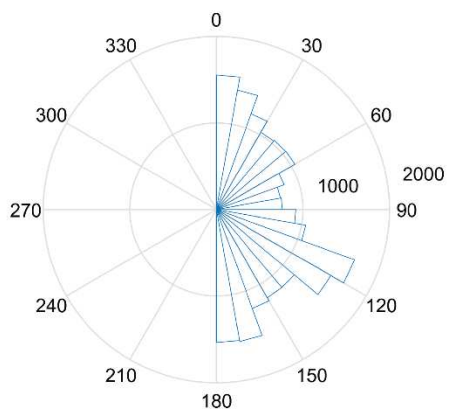
Rose diagram

Fig. A.10 FESEM-CL microimage L05-08 3. Southern wall rock, 0 mm from the pseudotachylyte fault vein.

200 µm

MATLAB® microfracture pattern

Frequency histogram

Fracture trend relative to pseudotachylyte fault vein
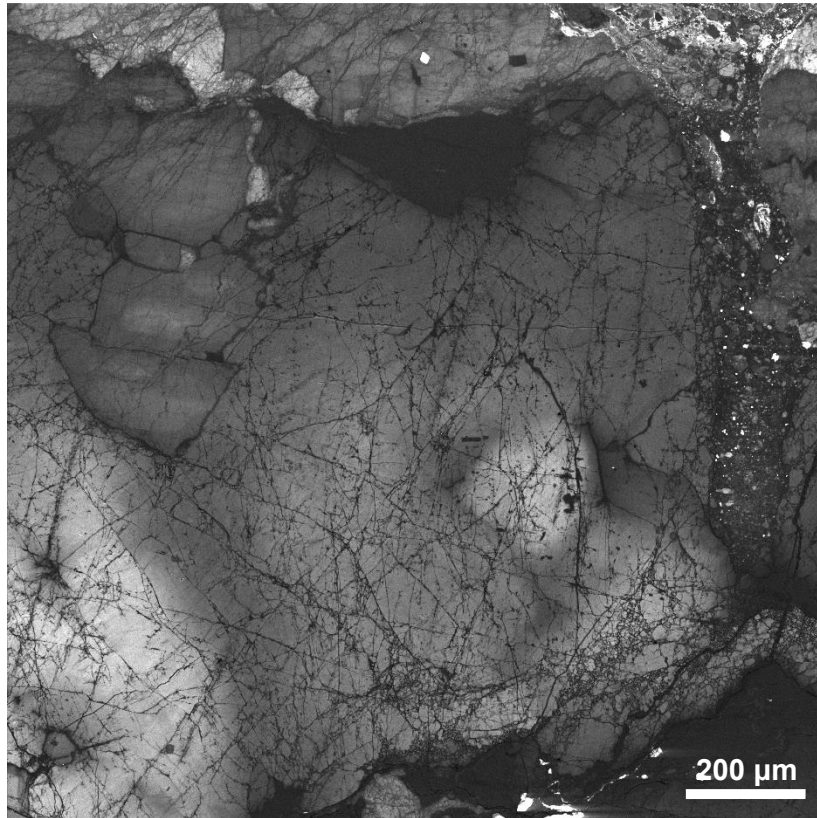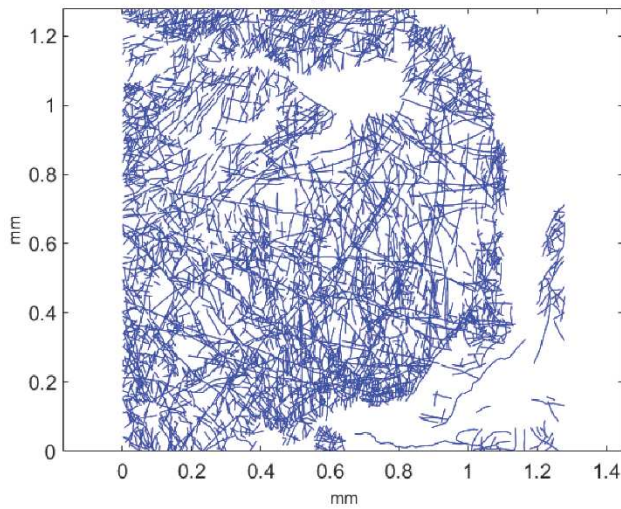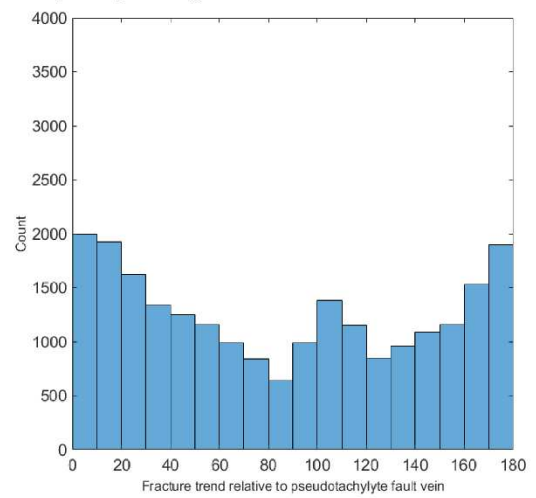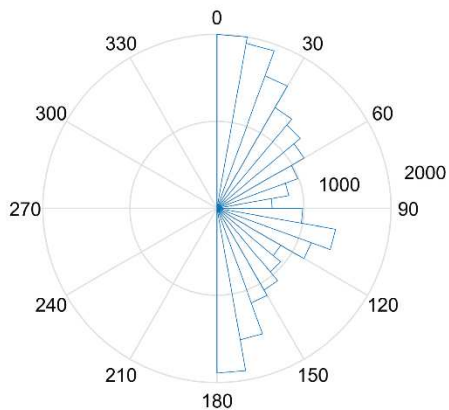
Rose diagram

Fig. A.11 FESEM-CL microimage WF22-01b 3. Southern wall rock, 0 mm from the pseudotachylyte fault vein.

102
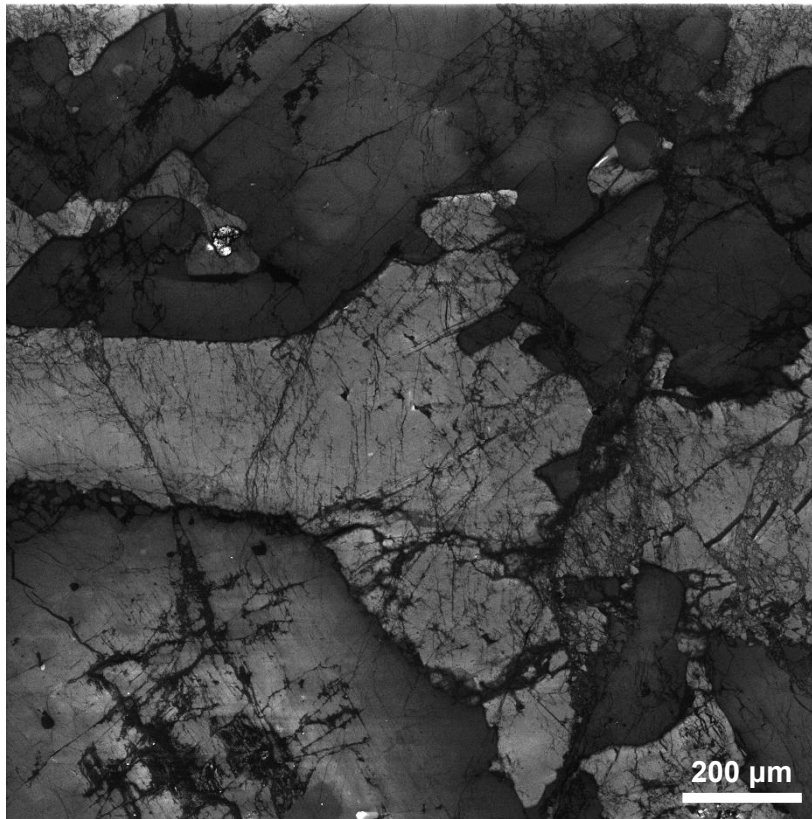
MATLAB® microfracture pattern
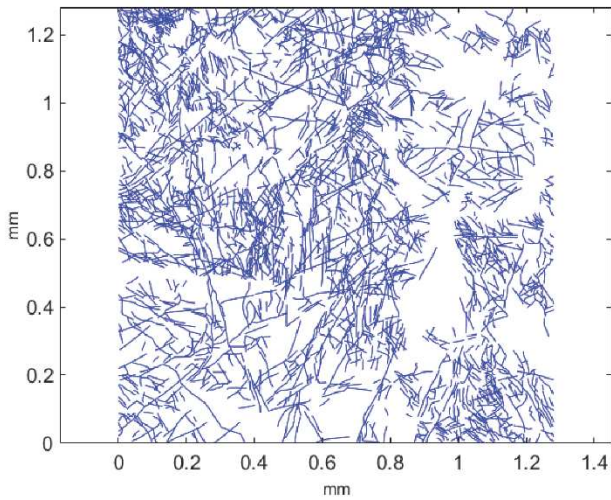
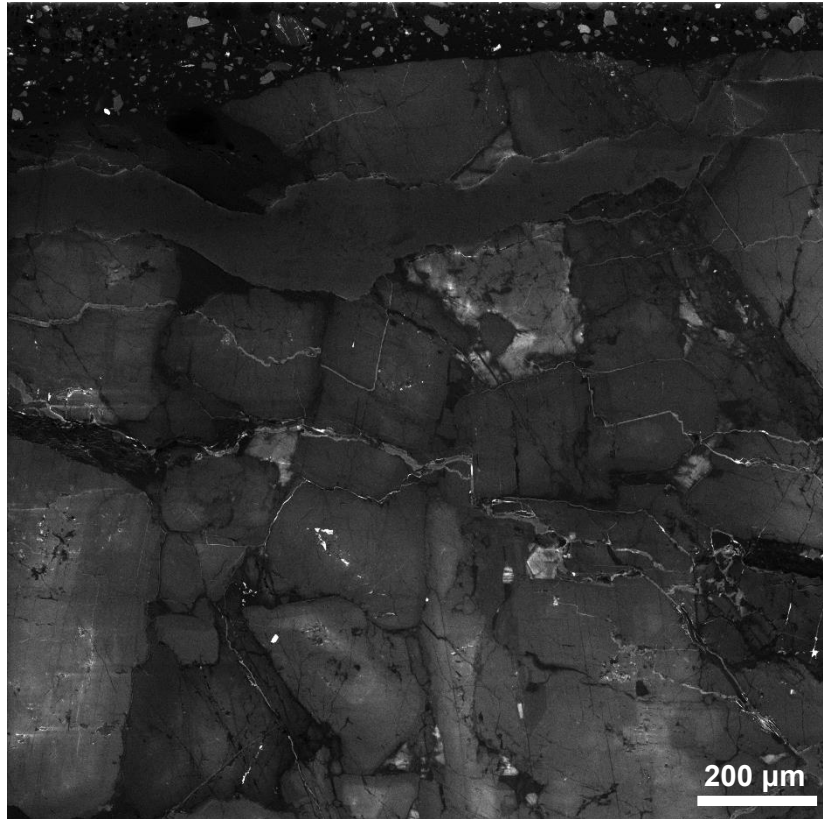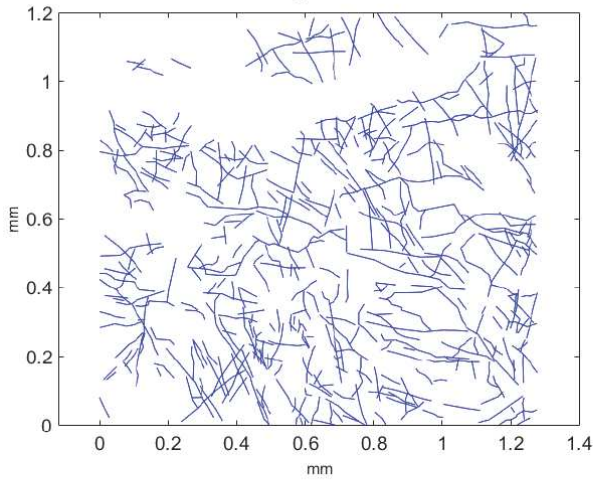Frequency histogram
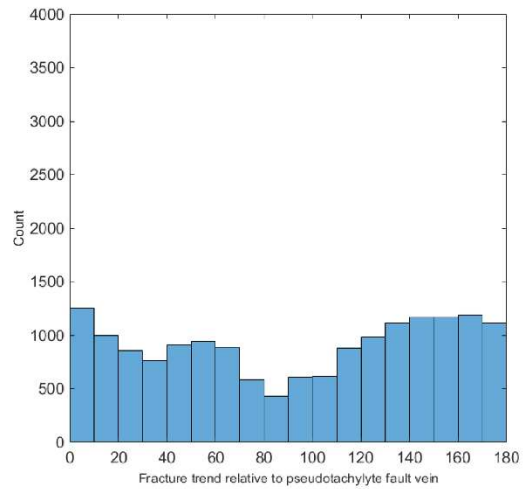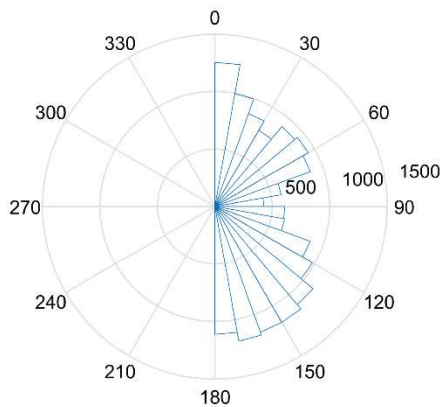
Rose diagram

Fig. A.12 FESEM-CL microimage L05-08 13. Southern wall rock, 7 mm from the pseudotachylyte fault vein.

103
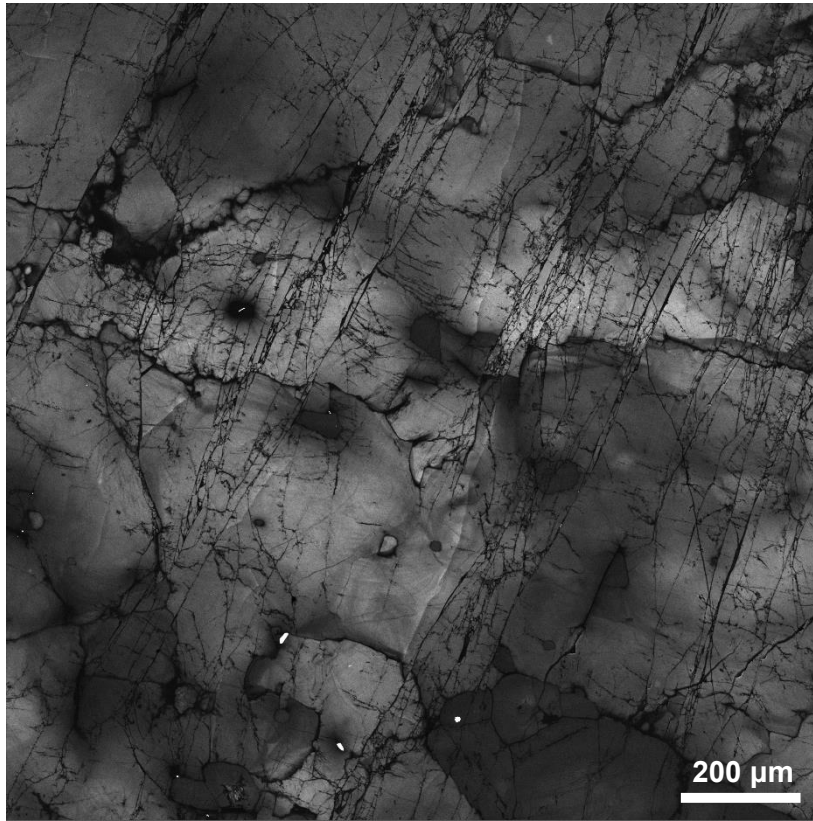
MATLAB® microfracture pattern
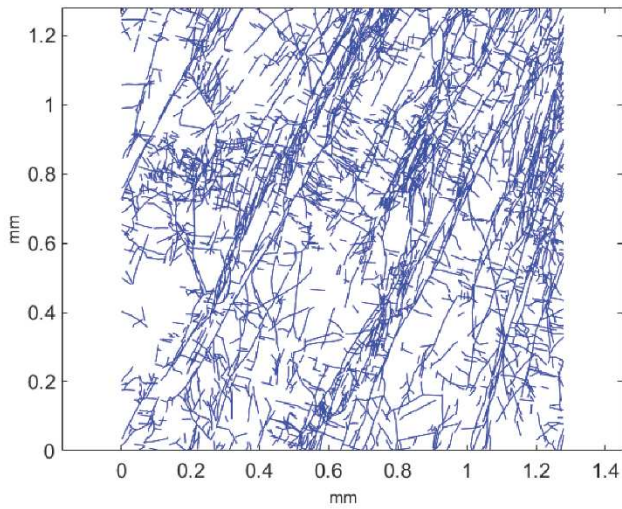
Frequency histogram
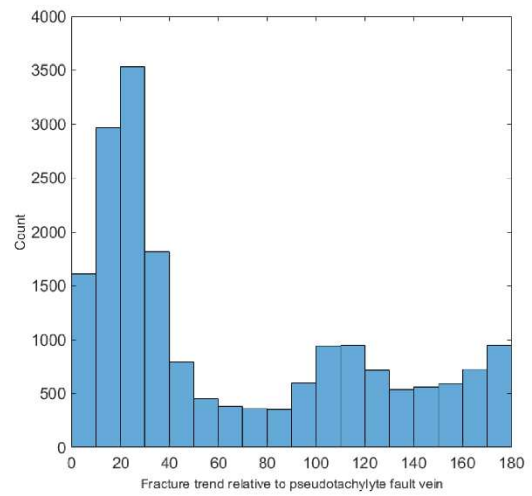
Rose diagram

Fig. A.13 FESEM-CL microimage WF22-01c 2. Southern wall rock, 22 mm from the pseudotachylyte fault vein.

104

200 µm

MATLAB® microfracture pattern

Frequency histogram

Rose diagram

Fig. A.14 FESEM-CL microimage HVR376 1. Stationary (N) side, 0 mm from the experimental pseudotachylyte.

MATLAB® microfracture pattern
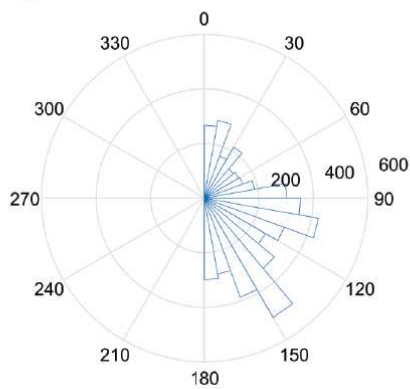

Frequency histogram
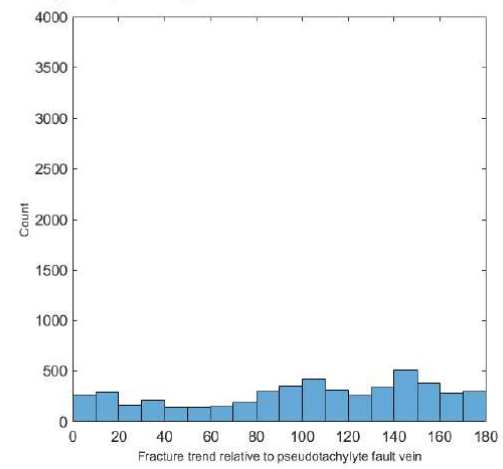
Rose diagram

Fig. A.15 FESEM-CL microimage HVR376 2. Rotary (S) side, 0 mm from the experimental pseudo-tachylyte.

Appendix B

MATLAB® script for microfracture analysis

```matlab
clear
close all
clc

%read xyz file
[seg, x, y] = textread('WF_22_01_B_03.xyz', '', 'delimiter', ',');


numnode = length(x);%number of nodes in .xyz file
node = 1:numnode; %index number of nodes
onenode = ones(numnode, 1); %boundary marker

%optional scale factor to scale to millimeters
sf = 1/1;
x = sf*(x-min(x));
y = sf*(y-min(y));


%optional rotation angle so that north points up
% rot = pi;%rotation angle
% x = x*cos(rot)+y*sin(rot); y = -x*sin(rot)+y*cos(rot);



%read node information and divide into individual segments
%get values for segments
numseg = 0;
for i = 2:numnode %find number of segments
    if seg(i)==seg(i-1)
        numseg = numseg+1;
    else
        numseg = numseg;
    end
end
segindex = 1:numseg; %index number of segments
segtotal = max(seg);


for i = 1:segtotal-1 %all fractures, excluding quartz boundary
elements
  j = find(seg==i);
```

```matlab
        segsubtotal(i) = length(j)-1;
end


%associate segments with nodes
for i = 1:segtotal-1
    for j = 1:segsubtotal(i)
        if i==1 && j==1
            segnode1(1) = 1;
            segnode2(1) = 2;
        elseif i==1 && j~=1
            segnode1(j) = segnode2(j-1);
            segnode2(j) = segnode1(j)+1;
        elseif i~=1 && j==1
            segnode1(1+length(segnode1)) =
segnode2(length(segnode1))+1;
            segnode2(1+length(segnode2)) =
segnode1(length(segnode1))+1;
        else
            segnode1(1+length(segnode1)) = segnode2(length(segnode1));
            segnode2(1+length(segnode2)) =
segnode1(length(segnode1))+1;
        end
    end
end


%%%%%%%%%%%%%%%%%%%%%%%%%%%%%%%%%%%%%%%%%%%%%%%%%%%%%%%%%%%%%%%%%%%%
%measure orientation, spacing, density data
%%%%%%%%%%%%%%%%%%%%%%%%%%%%%%%%%%%%%%%%%%%%%%%%%%%%%%%%%%%%%%%%%%%%

qtz_area = polyarea(x(find(seg==max(seg))),
y(find(seg==max(seg))));%(max(x(i))-min(x(i))).*(max(y(i))-
min(y(i)));%calculate grain volume
for i = 1:numseg-length(x(find(seg==max(seg))))
    seg_length(i) = sqrt((x(segnode1(i))-
x(segnode2(i)))^2+(y(segnode1(i))-y(segnode2(i)))^2);
    seg_az(i) = acos((x(segnode1(i))-
x(segnode2(i)))/seg_length(i))*180/pi;
    seg_slope(i) = (y(segnode2(i))-y(segnode1(i)))/(x(segnode2(i))-
x(segnode1(i)));
    rise(i) = (y(segnode2(i))-y(segnode1(i)));
    run(i) = (x(segnode2(i))-x(segnode1(i)));
```

108

```
        end



    trend = -atan2(rise, run)*180/pi+90;
    trend(find(trend<0))=trend(find(trend<0))+180;
    trend(find(trend>180))=trend(find(trend>180))-180;
    for i = 1:length(trend)
        if trend(i) == 0
            trend(i) = 0.01;
        elseif trend(i) == 180
            trend(i) = 179.9;
        end
    end


    avefraclength = sum(seg_length)/(max(seg)-1);%mean fracture length
    a = avefraclength/2;%mean half-length
    L = sum(seg_length); %total length of all fractures
    S_approx = qtz_area/(L+sqrt(qtz_area)); %average spacing using the
    area method


    %calculate nodimensional fracture density
    for i = 1:max(seg)-1
        j  = find(seg == i);
        xtemp = x(j); ytemp = y(j);
        for k = 1:length(j)-1
            d(k) = sqrt((xtemp(k+1)-xtemp(k))^2+(ytemp(k+1)-ytemp(k))^2);
        end
        frac_length(i) = sum(d);
    end
    epsilon = sum((frac_length./2).^2)/1.64;%nondimensional fracture
    density



    alpha_ave = mean(seg_az);


    %hist(seg_az, 18), text(-80, 110, 'n=566, S = 0.22', 'fontsize', 14),
    xlabel('Fracture Trend Relative to x_3', 'fontsize', 14),
    ylabel('Count', 'fontsize', 14)
    figure
```

```matlab
histogram(trend, 18), xlabel('\'), axis([0 180 0 4000]),
xlabel('Fracture trend relative to pseudotachylyte fault vein',
'fontsize', 12), ylabel('Count', 'fontsize', 12)
%figure, rose(trend*pi/180, 36), view(90,-90)
% print(gcf,'L05-08_05_hist','-dpng','-r600')

figure, rose(trend*pi/180, 36), view(90,-90)
%title('L05-08 03','fontsize', 12)
%text(10, 80, 'N = 534, \Gamma_{2D} = 1.36, S = 0.22, \alpha_{mean} =
%49^o', 'fontsize', 14),
print(gcf,'HVR376_02_rose','-dpng','-r600')

figure
for i = 1:max(seg)
   if i < max(seg)
    j  = find(seg == i);
    plot(x(j), y(j), 'b'), hold on
   else
    j  = find(seg == i);
    plot(x(j), y(j), 'k'), hold on
   end
end
axis equal
xlabel ('mm','fontsize', 12)
ylabel ('mm','fontsize', 12)
% title 'Microfracture pattern'
% print(gcf,'L05-08_03_fractures','-dpng','-r600')
```

MATLAB® MTEX script for EBSD data

```matlab
%% Import Script for EBSD Data
%
% This script was automatically created by the import wizard. You
should
% run the whoole script or parts of it in order to import your data.
There
% is no problem in making any changes to this script.


%% Specify Crystal and Specimen Symmetries

% crystal symmetry
CS = {...
  'notIndexed',...
  crystalSymmetry('321', [4.9 4.9 5.5], 'X||a*', 'Y||b', 'Z||c*',
'mineral', 'Quartz', 'color', [0.53 0.81 0.98]),...
  crystalSymmetry('12/m1', [5.4 9.3 10], [90,100.222,90]*degree,
'X||a*', 'Y||b*', 'Z||c', 'mineral', 'Biotite', 'color', [0.56 0.74
0.56]),...
  crystalSymmetry('12/m1', [8.5 13 7.2], [90,116.162,90]*degree,
'X||a*', 'Y||b*', 'Z||c', 'mineral', 'Feldspar', 'color', [0.85 0.65
0.13]),...
  crystalSymmetry('-1', [8.1 13 7.1], [93.94,116.54,88.46]*degree,
'X||a*', 'Z||c', 'mineral', 'Albite', 'color', [0.94 0.5 0.5])};


% plotting convention
setMTEXpref('xAxisDirection','east');
setMTEXpref('zAxisDirection','intoPlane');


%% Specify File Names


% path to files
pname = 'C:\Users\Utente\Desktop\TESI MAGISTRALE\MTEX\L0508_EBSD Site
1 Map Data 1';


% which files to be imported
fname = [pname '\L0508_EBSD Specimen 1 Site 1 Map Data 1_clean.crc'];


%% Import the Data
```

```matlab
% create an EBSD variable containing the data
ebsd = EBSD.load(fname,CS,'interface','crc',...
  'convertEuler2SpatialReferenceFrame');

%% plot band contrast
figure(1)
plot(ebsd,ebsd.bc)
mtexColorMap black2white
% print(gcf,'L05-08_Map1_bc.png','-dpng','-r600')

%% calculate grains
[grains,ebsd.grainId,ebsd.mis2mean] =
calcGrains(ebsd,'angle',10*degree)
figure(2)
plot(grains,'micronbar','off')
legend('Location','northoutside')
% print(gcf,'L05-08_Map1_Grains.png','-dpng','-r600')
%% merge biotite to non indexed values
ebsd(ebsd.phase == 2).phase = 0;

figure(3)
plot(ebsd,'micronbar','off')
% print(gcf,'L05-08_Map1_phase_noBt.png','-dpng','-r600')
%% calculate grains again after biotite and nIv merging
[grains,ebsd.grainId,ebsd.mis2mean] =
calcGrains(ebsd,'angle',10*degree)
figure(4)
plot(grains,'micronbar','off')
legend('Location','southeast')
% print(gcf,'L05-08_Map1_Grains_noBt.png','-dpng','-r600')
%% check Dauphinè twins
gb_Qu = grains.boundary('Quartz','Quartz');
rot = rotation('axis',Miller(0,0,0,1,CS{2}),'angle',60*degree);
ind = angle(gb_Qu.misorientation,rot)<4*degree;
twinBound = gb_Qu(ind);

figure(5)
plot(grains('Quartz'),'micronbar','off')
hold on
plot(twinBound,'linecolor','r')
% print(gcf,'L05-08_Map1_Dauphinè.png','-dpng','-r600')
```

112

```matlab
%% hexagonal simmetry
CS_hex = {...
  'notIndexed',...
  crystalSymmetry('622', [4.9 4.9 5.5], 'X||a*', 'Y||b', 'Z||c*',
'mineral', 'Quartz-new', 'color', [0.53 0.81 0.98]),...
  crystalSymmetry('12/m1', [5.4 9.3 10], [90,100.222,90]*degree,
'X||a*', 'Y||b*', 'Z||c', 'mineral', 'Biotite', 'color', [0.56 0.74
0.56]),...
  crystalSymmetry('12/m1', [8.5 13 7.2], [90,116.162,90]*degree,
'X||a*', 'Y||b*', 'Z||c', 'mineral', 'Feldspar', 'color', [0.85 0.65
0.13]),...
  crystalSymmetry('-1', [8.1 13 7.1], [93.94,116.54,88.46]*degree,
'X||a*', 'Z||c', 'mineral', 'Albite', 'color', [0.94 0.5 0.5])};

ebsd_hex = ebsd;
ebsd_hex.CS=CS_hex;

[grains,ebsd.grainId,ebsd.mis2mean] =
calcGrains(ebsd,'angle',10*degree)
%% remove small grains
min_points = 4;
ebsd(grains(grains.grainSize < min_points)).phase = 0;
[grains,ebsd.grainId,ebsd.mis2mean] =
calcGrains(ebsd,'angle',10*degree);

figure(6)
plot(grains,'micronbar','off')
legend('Location','southeast')
% print(gcf,'L05-08_Map1_Grains_removed4.png','-dpng','-r600')
%% set single notIndexed pixels to not measured
ebsd(grains(grains.grainSize <=2)) = []
[grains,ebsd.grainId,ebsd.mis2mean] =
calcGrains(ebsd,'angle',10*degree);

figure(7)
plot(grains,'micronbar','off')
legend('Location','southeast')
% print(gcf,'L05-08_Map1_Grains_nIp.png','-dpng','-r600')
%% fill empty portions (those deleted in the previous section)
ebsd = fill(ebsd);
%% smooth grainboundaries
```

```matlab
grains= smooth(grains,1);
%% plot EBSD qz - mis2mean
figure(7)
plot(ebsd('Quartz'),ebsd('quartz').mis2mean.angle./degree)
mtexColorbar
hold on
plot(grains('Quartz').boundary)
print(gcf,'L05-08_Map1_qz_mis2mean.png','-dpng','-r600')

figure(8)
plot(ebsd('Feldspar'),ebsd('feldspar').mis2mean.angle./degree)
mtexColorbar
hold on
plot(grains('Feldspar').boundary)
print(gcf,'L05-08_Map1_feld_mis2mean.png','-dpng','-r600')

figure(9)
plot(ebsd('Albite'),ebsd('albite').mis2mean.angle./degree)
mtexColorbar
hold on
plot(grains('Albite').boundary)
print(gcf,'L05-08_Map1_ab_mis2mean.png','-dpng','-r600')
%% plot EBSD - KAM
figure(10)
plot(ebsd('Quartz'),ebsd('Quartz').KAM./degree)
caxis([0 5])
mtexColorbar
mtexColorMap LaboTeX
hold on
plot(grains('Quartz').boundary)
print(gcf,'L05-08_Map1_qz_KAM.png','-dpng','-r600')

figure(11)
plot(ebsd('Feldspar'),ebsd('Feldspar').KAM./degree)
caxis([0 5])
mtexColorbar
mtexColorMap LaboTeX
hold on
plot(grains('Feldspar').boundary)
print(gcf,'L05-08_Map1_feld_KAM.png','-dpng','-r600')
```

114

```
figure(12)
plot(ebsd('Albite'),ebsd('Albite').KAM./degree)
caxis([0 5])
mtexColorbar
mtexColorMap LaboTeX
hold on
plot(grains('Albite').boundary)
print(gcf,'L05-08_Map1_ab_KAM.png','-dpng','-r600')
%% plot EBSD qz - 1) IPF
ipfKey = ipfHSVKey(ebsd('Quartz'));
ipfKey.inversePoleFigureDirection = vector3d.X;
colors_X = ipfKey.orientation2color(ebsd('Quartz').orientations);
ipfKey.inversePoleFigureDirection = vector3d.Y;
colors_Y = ipfKey.orientation2color(ebsd('Quartz').orientations);
ipfKey.inversePoleFigureDirection = vector3d.Z;
colors_Z = ipfKey.orientation2color(ebsd('Quartz').orientations);

figure(111), plot(ipfKey)
print(gcf,'L05-08_Map1_IPF_colorkey_qz.png','-dpng','-r600')

%%%

ipfKey = ipfHSVKey(ebsd('Feldspar'));
ipfKey.inversePoleFigureDirection = vector3d.X;
colors_X = ipfKey.orientation2color(ebsd('Feldspar').orientations);
ipfKey.inversePoleFigureDirection = vector3d.Y;
colors_Y = ipfKey.orientation2color(ebsd('Feldspar').orientations);
ipfKey.inversePoleFigureDirection = vector3d.Z;
colors_Z = ipfKey.orientation2color(ebsd('Feldspar').orientations);

figure(111), plot(ipfKey)
print(gcf,'L05-08_Map1_IPF_colorkey_feld.png','-dpng','-r600')

%%%

ipfKey = ipfHSVKey(ebsd('Albite'));
ipfKey.inversePoleFigureDirection = vector3d.X;
colors_X = ipfKey.orientation2color(ebsd('Albite').orientations);
ipfKey.inversePoleFigureDirection = vector3d.Y;
colors_Y = ipfKey.orientation2color(ebsd('Albite').orientations);
ipfKey.inversePoleFigureDirection = vector3d.Z;
```

```matlab
colors_Z = ipfKey.orientation2color(ebsd('Albite').orientations);

figure(111), plot(ipfKey)
print(gcf,'L05-08_Map1_IPF_colorkey_ab.png','-dpng','-r600')

%% plot EBSD QZ - 2) PLOT
figure(13)
plot(ebsd('Quartz'),colors_X,'micronbar','off')
hold on
plot(grains('Quartz').boundary)
print(gcf,'L05-08_Map1_qz_IPFX.png','-dpng','-r600')

figure(14)
plot(ebsd('Quartz'),colors_Y,'micronbar','off')
hold on
plot(grains('Quartz').boundary)
print(gcf,'L05-08_Map1_qz_IPFY.png','-dpng','-r600')

figure(15)
plot(ebsd('Quartz'),colors_Z,'micronbar','off')
hold on
plot(grains('Quartz').boundary)
print(gcf,'L05-08_Map1_qz_IPFZ.png','-dpng','-r600')
%% plot EBSD FELD - 2) PLOT
figure(16)
plot(ebsd('Feldspar'),colors_X,'micronbar','off')
hold on
plot(grains('Feldspar').boundary)
print(gcf,'L05-08_Map1_feld_IPFX.png','-dpng','-r600')

figure(17)
plot(ebsd('Feldspar'),colors_Y,'micronbar','off')
hold on
plot(grains('Feldspar').boundary)
print(gcf,'L05-08_Map1_feld_IPFY.png','-dpng','-r600')

figure(18)
plot(ebsd('Feldspar'),colors_Z,'micronbar','off')
hold on
plot(grains('Feldspar').boundary)
print(gcf,'L05-08_Map1_feld_IPFZ.png','-dpng','-r600')
```

116

```matlab
%% plot EBSD AB - 2) PLOT
figure(19)
plot(ebsd('Albite'),colors_X,'micronbar','off')
hold on
plot(grains('Albite').boundary)
print(gcf,'L05-08_Map1_ab_IPFX.png','-dpng','-r600')

figure(20)
plot(ebsd('Albite'),colors_Y,'micronbar','off')
hold on
plot(grains('Albite').boundary)
print(gcf,'L05-08_Map1_ab_IPFY.png','-dpng','-r600')

figure(21)
plot(ebsd('Albite'),colors_Z,'micronbar','off')
hold on
plot(grains('Albite').boundary)
print(gcf,'L05-08_Map1_ab_IPFZ.png','-dpng','-r600')
```

Acknowledgments